Volume 9, Number 4, Autumn 2023

ACERP
Advanced Ceramics Progress

ISSN 2423-7477
e-ISSN 2423-7485

Advanced Ceramics Progress

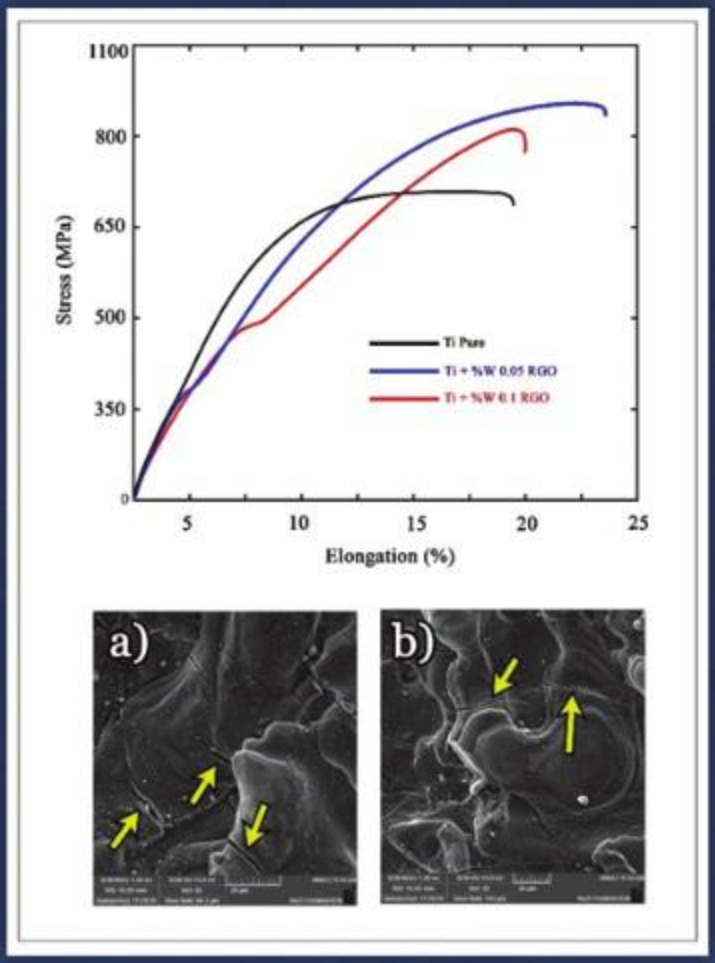

Materials and Energy
Research Center

Iranian Ceramic Society

In The name of God

Advanced Ceramics Progress

Advanced **Cer**amics **P**rogress (ISSN 2423-7477) (e-ISSN 2423-7485)

Web Site: www.acerp.ir, E-mail: office@acerp.ir
Tel: +98 (0) 26 36280040-7 ext.: 173, Fax: +98 (0) 26 36201888
Tel:+98 (0)21 88771626-7 ext.: 8931, Fax: +98 (0)21 88773352

Materials and Energy Research Center (MERC); Iranian Ceramic Society (ICERS)

AIMS AND SCOPE

Advanced Ceramics Progress (ACERP) as an ISC international journal is devoted to elucidating the fundamental aspects of chemistry and physics occurring at a wide range of oxide and nonoxide ceramics and composite materials and their processing, microstructure, properties, and applications. The journal provides a unique venue for publishing new exciting research, focusing on dynamic growth areas in this field.

INSTRUCTIONS FOR AUTHORS

Submission of manuscript represents that it has neither been published nor submitted for publication elsewhere and is result of research carried out by author(s).
Authors are required to include a list describing all the symbols and abbreviations in the paper. Use of the international system of measurement units is mandatory.

- On-line submission of manuscripts results in faster publication process and is recommended. Instructions are given in the ACERP web site: www.acerp.ir
- Hardcopy submissions must include MS Word and jpg files.
- Manuscripts should be typewritten on one side of A4 paper, double-spaced, with adequate margins.
- References should be numbered in brackets and appear in sequence through the text. List of references should be given at the end of the paper.
- Figures' captions are to be indicated under the illustrations. They should sufficiently explain the figures.
- Illustrations should appear in their appropriate places in the text.
- Tables and diagrams should be submitted in a form suitable for reproduction.
- Photographs should be of high quality saved as jpg files.
- Tables, illustrations, figures and diagrams will be normally printed in single column width (8 cm). Exceptionally large ones may be printed across two columns (17 cm).

PAGE CHARGES AND REPRINTS

ACERP subscribers do not need to make any payment for publication and reprints.

AUTHORS CHECKLIST

- Author(s), bio-data including affiliation(s) and mail and e-mail addresses.
- Manuscript including abstract, key words, illustrations, tables, figures with figures' captions and list of references.
- MS Word files of the paper.

Advanced **Cer**amics **P**rogress,
P.O. Box 31787-316, Karaj, Alborz, I. R. Iran
Materials and Energy Research Center, Imam Khomeini Blvd, Meshkin Dasht, Karaj, Alborz, I. R. Iran
P.O. Box 14155-4777, Tehran, I. R. Iran
No. 5, Ahuramazda St., Alvand Ave., Argentine Sq., Tehran, I. R. Iran

www.merc.ac.ir - www.acerp.ir

ISSN: 2423-7477; e-ISSN: 2423-7485

Advanced Ceramics Progress: Vol. 9, No. 4, (Autumn 2023) 1-49

CONTENTS

Advanced Ceramics Progress: Vol. 9, No. 4, (Autumn 2023) 1-6

Materials and Energy Research Center
MERC

Contents lists available at ACERP

Advanced Ceramics Progress

Journal Homepage: www.acerp.ir

Original Research Article

The Role of Diamond on Wear Properties of WC-Co Composite

Parinaz Pirmohammadi [a], Mohammad Zakeri [b]*, Mansour Razavi [c], Leila Nikzad [b]

[a] *PhD Student, Department of Ceramics, Materials and Energy Research Center, Karaj, Iran.*
[b] *Associate Professor, Department of Ceramics, Materials and Energy Research Center, Karaj, Iran.*
[c] *Professor, Department of Ceramics, Materials and Energy Research Center, Karaj, Iran.*

* Corresponding Author Email: m_zakeri@merc.ac.ir (M. Zakeri)

URL: https://www.acerp.ir/article_181841.html

ARTICLE INFO

Article History:

Received: 10 October 2023
Revised: 22 October 2023
Accepted: 25 October 2023

Keywords:

Diamond/WC-Co Composite,
Spark Plasma Sintering,
Wear Rate,
Wear Mechanism,

ABSTRACT

There is a growing interest in researching materials to produce wear-resistant composites. The current study aims to investigate the impact of adding 2.5 vol% diamond on the wear behavior of the WC-6% wt. Co composite. The samples were first fabricated using the spark plasma sintering method at 1300 °C for five minutes under the pressure of 40 MPa. The pin-on-disk method was employed to study the wear behavior, followed by evaluating the worn surfaces using SEM analysis. According to the results from the worn surfaces analysis, addition of diamond to the WC-Co composite reduced the wear rate from 0.34×10^{-4} mm³/N·m to 0.25×10^{-4} mm³/N·m. According to the SEM images, abrasive wear was the main wear mechanism in the WC-Co composite while the abrasive, adhesive, and oxidation mechanisms were the primary wear mechanisms in the WC-Co sample reinforced with diamond phase. The presence of diamond as a hard phase within WC-Co composite significantly improved the wear resistance of the composite.

https://doi.org/10.30501/acp.2023.420137.1135

1. INTRODUCTION

Modern industries are keenly interested in materials that exhibit enhanced wear resistance since these materials provide significant advantages including prolonged lifetime and ability to withstand heavy tribological conditions, to name a few (Holmberg, et al., (2007), Van Acker, et al., (2005), Bonny, et al.,(2009)). WC-Co composites are extensively used in the aerospace industry and mechanical engineering sectors due to their outstanding properties such as high hardness and fracture toughness, resulting in exceptional wear resistance. To achieve optimal sintering results in the WC-Co composites, SPS method is preferred. This technique employs high-pulsed electric current and Joule heat to sinter the powder compact, ensuring efficient and effective consolidation (Ma, et al., (2017)).

Extensive research has been carried out to enhance the wear characteristics and investigate the wear mechanisms of WC-Co composites (Beste & Jacobson, (2008))(Saito, et al.,(2006)) (JY & JA, (1999)) (Gant & Gee, (2006)). Studies indicate that the wear characteristics of WC-Co can be improved by incorporating carbides like Ta, Nb, Cb, Ti, Mo, V, and Cd into the hardmetals (Bonny et al., (2010)) (Brookes, (1998)) (Pirso, (2006)).

Pirso et al., (2006) conducted a study on sliding wear and friction behavior of WC–Co, Cr_3C_2–Ni, and TiC–NiMo composites. The results of block-on-ring test

Please cite this article as: Pirmohammadi, P., Zakeri, M., Razavi, M., Nikzad, L., "The Role of Diamond on Wear Properties of WC-Co Composite", ***Advanced Ceramics Progress***, Vol. 9, No. 4, (2023), 1-6. https://doi.org/10.30501/acp.2023.420137.1135

showed that the wear behavior of the Cr_3C_2–Ni cermet was influenced by their composition while the wear response of the WC-Co and TiC-NiMo cermet was determined by the amount of binder present.

Bonny et al., (2009) investigated WC–Co–Cr_3C_2–VC composites, remarking that addition of Cr_3C_2–VC to WC-Co decreased the composite friction. Quercia et al., (2001) studied the wear properties of WC–Co–(Ta,V)C composites under sliding, abrasion, and erosion conditions, proving that the mechanical properties and tribosystem configuration were the key factors affecting the wear behavior of these composites. Moreover, addition of TiC to cemented carbides enhanced the abrasion resistant of WC-Co composite due to the higher hardness of TiC than that of WC (Quercia, et al., (2001)) (Budinski & Budinski, (2002)).

van der Merwe & Sacks (2013) studied how TaC, TiC, and NbC could affect friction and dry sliding wear in WC–6 wt.% Co composite when interacting with steel surfaces. They found that incorporating less than 1 wt.% TaC resulted in enhanced wear resistance. The primary wear mechanisms observed for the carbides were preferential removal of the binding material, grain cracking and fragmentation, carbide grain pull-out, and formation of a protective film on the contact surfaces.

One way to enhance the wear resistance of the WC-Co composites is to incorporate super-hard and wear-resistant materials such as diamond and cubic-BN (Grasso, et al., (2011)) (Yaman & Mandal (2014)). Incorporation of the diamond particles into the WC-Co composites is expected to improve their wear behavior, and this improvement is attributed to the extremely low friction coefficients, approximately 0.1, observed in diamond and chemical vapor deposition diamond coatings under dry running conditions (Habig, (1995) (Hollman, et al., (1998)) (Hayward, (1991)).

Belji Yaman et al. demonstrated that the wear properties of tungsten carbide would be improved by adding cBN and using the SPS method (Yaman & Mandal, (2014). Salvatore Grasso et al., (2011) conducted the ultrafast SPS process to fabricate diamond binder less WC composites. The presence of diamond as an additive resulted in a reduction in the wear rate and a decrease in the friction coefficient of these composites from 0.328 to 0.117.

Fabrication of diamond hard-metal composites at low pressures poses significant technological challenges due to the thermodynamic instability of diamond under these conditions, leading to the graphitization of diamond (Ganta, et al., (2018)).

The cemented carbide composite are renowned for their remarkable wear properties. In previous studies, high percentages of diamond with larger grain sizes were commonly used as reinforcement for these composites. However, it is anticipated that even low percentages of diamond can enhance the wear properties of cemented carbide owing to the remarkable properties of diamond. Therefore, it is essential to investigate the role of even a small amount of diamond in the wear mechanism of composites that contain finer-grained diamond. The present research primarily focused on the effect of diamond presence on wear mechanisms, using the SPS method for consolidation. The worn surfaces were analyzed through scanning electron microscopy.

2. MATERIALS AND METHODS

The aim of the current study is to evaluate the effect of using diamond as an additive on the wear properties of the WC-Co composite. To this end, two samples were prepared, one with 2.5 Vol% diamond additive and another without the additive.

High-purity commercial powders WC (Almase Saz Co., 0.5µm, 99.9%), Co (Almase Saz Co.,1µm, 99.9%), and diamond (Henan Huanghe whirlwind Co., China, 10µm, 99 %) powder as the reinforcements were mixed in a planetary mill with cemented carbide balls in an ethanol environment at the rotation speed of 120 rpm for 3 hours. After drying the mixture and passing it through a sieve with a 50 µm mesh, it was poured into a graphite mold with the inner diameter of 30 mm. The sintering process was carried out in an SPS-20T-10 machine from China. The samples were spark plasma sintered in 1300 ˚C under 40 MPa for 5 min. Finally, the samples cooled to room temperature under a pressure of 40 MPa. After sintering, the samples were cleaned of graphite using a cubic-BN disk, polished with SiC papers and finally, mirrored with 2, 1, and 0.5 µm diamond paste.

To investigate the wear behavior of the samples, pin-on-disk wear test was done. Figure 1 shows the schematic of the sample and wear device used for the wear test. The wear test was conducted at room temperature in dry condition, using a SiC abrasive pin with the sliding speed of 0.07 m/s, normal load of 38.2 N, and sliding distance of 800 m. The wear rate is defined as follows [22]:

$$\text{Wear rate} = \frac{V}{N.S} \quad (1)$$

where V, N, and S are the volume loss of the specimen (mm^3), normal load (N), and sliding distance (m) respectively. The volume loss was obtained from the following equation (ASTM-G99-05(2010)):

$$\text{Volume loss } (V) = \frac{(\pi R d^3)}{6r} \quad (2)$$

where R, d, and r are the wear track radius (mm), wear track width (mm), and pin radius (mm) after wear tests, respectively.

The worn surfaces of samples were investigated by scanning electron microscope (FESEM; TESCAN MIRA3), and their elemental composition was analyzed using Energy Dispersive Spectroscopy (EDX). The phase composition of the SPSed sample was determined using

a Philips-PW3710 X-ray diffractometer with Cu Kα radiation (λ=0.15406 nm).

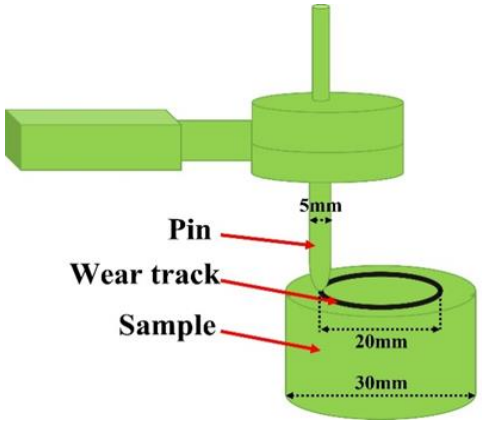

Figure 1. Schematic of the wear device and sample for the pin-on-disk test

3. RESULTS AND DISCUSSION

In Figure 2, the worn surfaces after 800 m wear are shown in low magnifications SEM images to better understand the wear behavior of the prepared samples.

An inverse relationship exists between the width of the worn surface and wear resistance of the sample. In the D2.5 sample, the width of the worn track decreased, indicating an improvement in the wear resistance of the sample.

Figure 3 shows the changes of width of worn surfaces and wear rate (as two main parameters to evaluation of wear resistance) for samples with diamond reinforcement and without diamond.

Upon comparing the worn surface widths of the samples, it was found that the sample without diamond has the lower wear resistance than that with diamond. The worn surface width and wear rate for the sample without diamond were obtained as 795 µm and 0.34×10^{-4} $mm^3/N.m$, respectively.

Followed by incorporating 2.5 Vol% diamond into the WC-Co matrix, significant improvements were observed in the wear resistance. The worn surface width and wear rate decreased by 722 µm and 0.25×10^{-4} $mm^3/N.m$, respectively, indicating an enhancement in the wear resistance compared to the previous condition.

According to the previous study (Pirmohammadi, et al., (2023)), hardness increased from 21.2 to 21.7 GPa by adding 2.5Vol% of diamond reinforcement to the matrix due to the reinforcing effect of diamond particles. Suh increase in the hardness can positively affect the wear resistance of the samples. In order to investigate the underlying wear mechanisms, the worn surface of the samples was studied using high-magnification SEM images and EDS analysis in more detail.

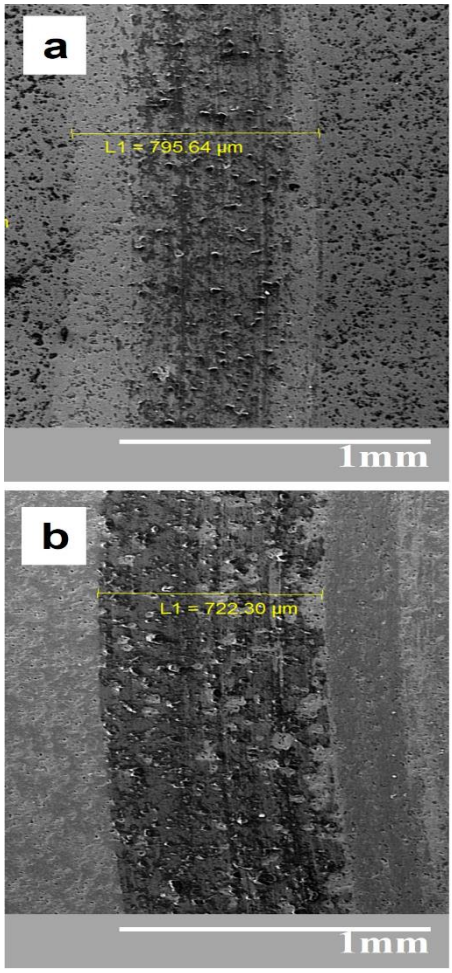

Figure 2. SEM images (Low magnification) of worn surfaces of a) D0, and b) D2.5

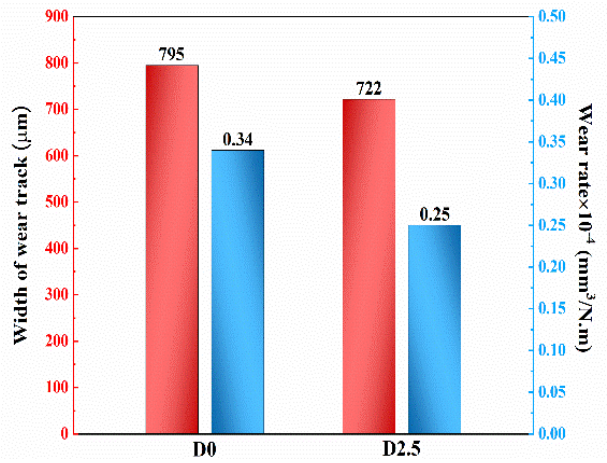

Figure 3. Variation of average width of worn surface, and wear rate for sample contained diamond and sample free diamond

Figure 4 depicts an SEM micrograph of the worn surface of D0 sample where ploughing grooves mechanism in the sliding direction, indicating the abrasive wear throughout the worn surface caused by the

continuous movement of high hardness pin on the surface of the sample.

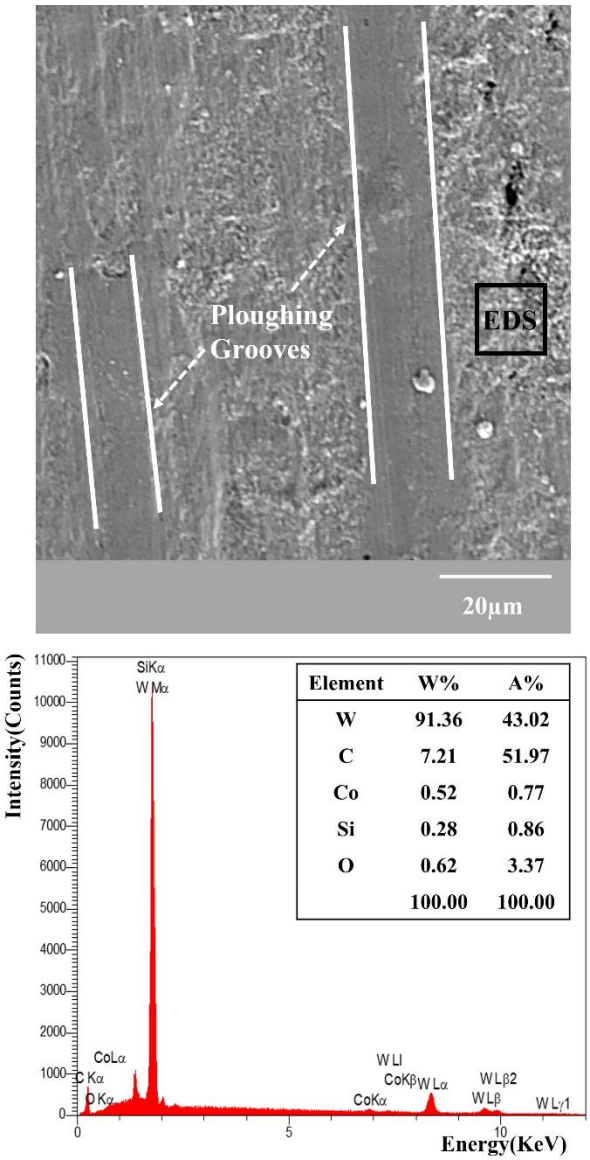

Element	W%	A%
W	91.36	43.02
C	7.21	51.97
Co	0.52	0.77
Si	0.28	0.86
O	0.62	3.37
	100.00	100.00

Figure 4. SEM micrograph and EDS analysis related to the worn surface of D0 sample

Some of the soft cobalt phase was apparently removed from the sample, and the tungsten carbide grains experienced wear. Furthermore, due to the continuous movement of the pin, a portion of the soft cobalt phase underwent plastic deformation and stretched across the sample surface.

EDS analysis confirmed the presence of tungsten, carbon, and cobalt as the sample constituents. Additionally, there is a very small amount of silicon (approximately 0.28 Wt%) which is related to the pin used for the wear test. This silicon was pull out from the pin and then attached to the sample during the interaction. Moreover, there is a small amount of oxygen (approximately 0.62 Wt%), resulting from the partial oxidation during the wear test.

The XRD of the diamond-reinforced composite sample is presented in Figure 5. The primary peaks observed in the sample are attributed to tungsten carbide. In addition to the peaks corresponding to tungsten carbide, cobalt and diamond peaks are also evident. The comparatively lower intensity of the cobalt and diamond peaks is due to the high absorbtion of WC and lower amount of diamond and cobalt compared to the WC phase.

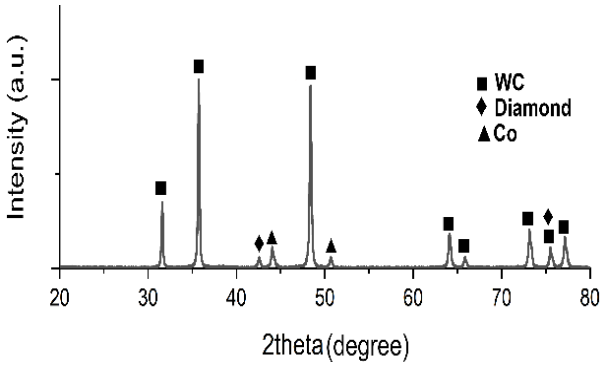

Figure 5. The XRD of D2.5 sample

As shown in Figure 6 of the SEM analysis of the fracture surface of the D2.5 sample, a dark phase is evenly distributed in the WC-Co matrix. According to the EDS analysis, this dark phase consists of diamond. The presence of tungsten and cobalt in the EDX spectrum is attributed to the presence of tungsten carbide and cobalt within the matrix.

Figure 7 depicts the SEM image displaying the worn surfaces of the D2.5 sample. Examination of these worn surfaces confirms the presence of pin elements through analysis using EDS. The presence of pin elements is a clear indication of the adhesive wear mechanism occurring in the D2.5 sample.

Additionally, the EDS results reveal the detection of oxygen on the worn surface of the composite samples, implying the involvement of an oxidation mechanism during the wear process.

Diamond exhibits higher thermal conductivity than tungsten carbide. This elevated thermal conductivity facilitates increased heat transfer to the sample during wear, unlike the sample without additives. As a result, the temperature of the sample rises more significantly during wear, thereby enhancing the oxidation reaction compared to sample without additives. Therefore, the presence of diamond in the sample is more advantageous for oxide layer formation.

The presence of an oxide layer on the worn surface has a positive effect on wear resistance as it acts as a protective barrier. This oxide layer prevents direct contact between the pin and the sample, thereby reducing friction and wear between the two surfaces.

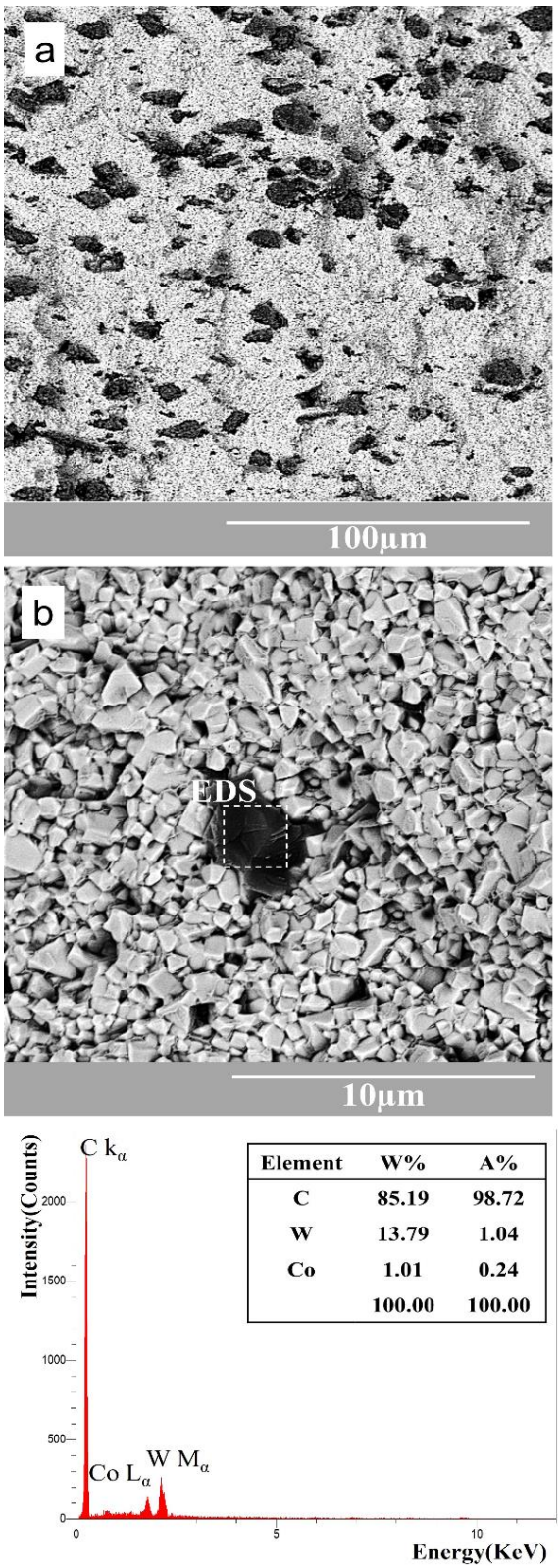

Figure 6. SEM image of fracture surface of D2.5 sample a) low magnification, and b) high magnification

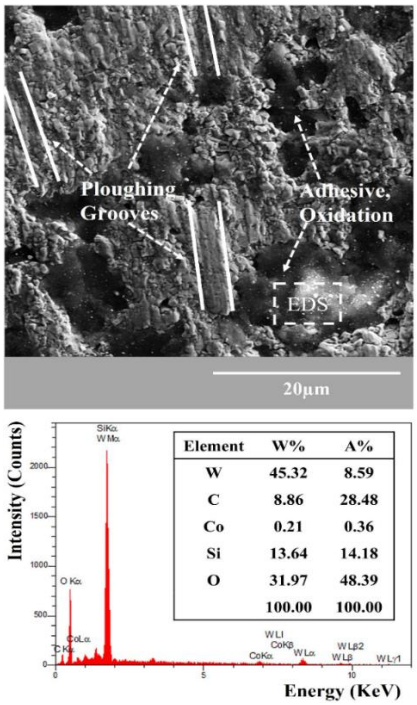

Figure 7. SEM micrograph related to the worn surfaces of D2.5 sample

The higher content of Si element observed in the worn surface of the D2.5 sample can be attributed to the increased interaction between the pin and the sample surface. This higher interaction would likely lead to the pull out Si from the pin and cause adhesion on the sample surface during the wear process. Hence, addition of diamond to WC-Co composites will result in a change in the wear mechanism from abrasion mechanism to a combination of oxidation, adhesion, and abrasion mechanisms. This change in wear behavior can be attributed to the enhanced hardness of the composite samples achieved through the addition of diamond and uniform distribution of reinforcement. The increased hardness promotes greater interaction between the counter surface and the composite sample, leading to the observed alteration in the wear mechanisms

As illustrated schematically in Figure 8-a, the main wear mechanisms observed in the D0 sample is abrasive mechanisms that include the removal of a portion of the soft cobalt phase from the surface and ploughing of the tungsten carbide phases. Additionally, a partially adhesive mechanism is observed. As depicted schematically in Figure 8-b, the main wear mechanisms observed in this sample involve abrasive and adhesive mechanisms. These mechanisms involve the removal of a portion of the soft cobalt phase from the surface and partial ploughing of the tungsten carbide phases. Furthermore, an increased occurrence of adhesive mechanism is observed, particularly on the diamond phases present on the surface of the sample, compared to the free diamond sample.

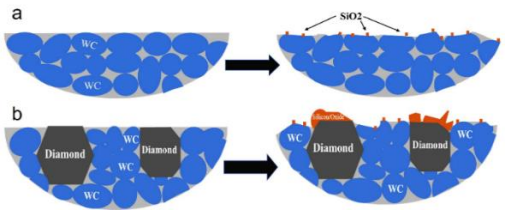

Figure 8. Schematic of wear mechanism in samples a) D0 and b) D2.5

4. CONCLUSION

This study employed SPS method to fabricate WC-Co-2.5 vol.% Diamond and WC-Co samples, and the wear behavior of these samples was examined. The results from wear test confirmed a significant improvement in the wear resistance for the WC-Co sample reinforced with diamond particles, compared to the pure WC-Co sample. The wear rate of the unreinforced WC-Co sample was 0.34×10^{-4} mm³/N·m, which decreased by 0.25×10^{-4} mm³/N·m after incorporating 2.5 vol.% diamond. In the pure WC-Co sample, abrasive wear was the predominant wear mechanism. However, incorporation of the diamond particles into the WC-Co matrix led to a complete change in the wear mechanism. The reinforced samples were a combination of oxidation, adhesive, and abrasive mechanisms during the wear process. The results revealed that diamond can be effectively used as a reinforcement to enhance the wear resistance of WC-Co composites.

ACKNOWLEDGEMENTS

The authors acknowledge the financial support from Materials and Energy Research Center (MERC), Karaj, Iran.

REFERENCES

1. **ASTM-G99-05, *Standard Test Method for Wear Testing with a Pin-On-Disk Apparatus*, Reapproved, (2010). https://www.academia.edu/27661541/Standard_Test_Method_for_Wear_Testing_with_a_Pin_on_Disk_Apparatus_1**
2. Beste, U., & Jacobson, S. A. (2008). New view of the deterioration and wear of WC/Co cemented carbide rock drill buttons. *Wear*, 264(11-12), 1129–1141. https://doi.org/10.1016/j.wear.2007.01.030
3. Bonny, K., Baets, P.De., Perez, Y., Vleugels, J. & Lauwers, B. (2010). Friction and wear characteristics of WC–Co cemented carbides in dry reciprocating sliding contact. ***Wear***, 268(11-12), 1504–1517. https://doi.org/10.1016/j.wear.2010.02.029
4. Bonny, K., De Baets, P., Ost, W., Vleugels, J., Huang, S., Lauwers, B., & Liu, W. (2009). Influence of electrical discharge machining on the reciprocating sliding wear response of WC–Co cemented carbides. ***Wear***, 266(1-2), 84–95. https://doi.org/10.1016/ j.ijrmhm.2008.09.002
5. Bonny, K., De Baets, P., Vleugels, J., Huang, S., Van der Biest, O., & Lauwers, B. (2009). Impact of Cr_3C_2/VC addition on the dry sliding friction and wear response of WC–Co cemented carbides. ***Wear***, 267(9-10), 1642–1652. https://doi.org/10.1016/j.wear.2009.06.013
6. Brookes, K. (1998). ***Hardmetals and other hard materials***. BPC Digital Information Limited. https://www.google.com/books/edition/Hardmetals_and_Other_Hard_Materials/peFGAQAAIAAJ?hl=en
7. Budinski, K. G. & Budinski, M. K. (2002). ***Engineering Materials, Properties and Selection***. New Jersey: Prentice Hall.
8. Gant, A.J. & Gee, M.G. (2006). Abrasion of tungsten carbide hard metals using hard counterfaces. *International* ***Journal of Refractory Metals and Hard Materials***. 24(1-2), 189–198. https://doi.org/10.1016/j.ijrmhm.2005.05.007
9. Ganta, A.J., Konyashin, I., Ries, B., McKie, A., Nilen, R.W.N. & Pickles, J. (2018). Wear mechanisms of diamond-containing hardmetals in comparison with diamond-based materials. ***International Journal of Refractory Metals & Hard Materials***, 71, 106-114. https://doi.org/10.1016/j.ijrmhm.2017.10.013
10. Grasso, S., Hu, C., Maizza, G. & Sakka, Y. (2011). Spark plasma sintering of diamond binderless WC composites. ***Journal of American Ceramic Society***, 95(8), 2423–2428. https://doi.org/10.1111/ j.1551-2916.2011.05009.x
11. Habig, K.H. (1995). Fundamentals of the tribological behaviour of diamond, diamond like carbon and cubic boron nitride coatings. ***Surface and Coating Technology***, 76–77(2), 540–547. https://doi.org/10.1016/0257-8972(95)02548-0
12. Hayward, I. P. (1991). Friction and wear properties of diamonds and diamond coatings. ***Surface and Coating Technology***, 49(1-3), 554–559. https://doi.org/10.1016/0257-8972(91)90116-E
13. Hollman, P., Wänstrand, O. & Hogmark, S. (1998). Friction properties of smooth nanocrystalline diamond coatings. ***Diamond and Related Materials***, 7(10), 1471–1477. https://doi.org/10.1016/ S0925-9635(98)00215-5
14. Holmberg, K., Ronkainen, H., Laukkanen, A., & Wallin, K. (2007). Friction and Wear of Coated Surfaces-Scales, Modelling and Simulation of Tribomechanisms. ***Surface and Coatings Technology***, 202(4-7), 1034–1049. https://doi.org/10.1016/j.surfcoat.2007.07.105
15. JY, S.A. & JA, B. (1999). The wear characteristics of some cemented tungsten carbides in machining particleboard. ***Wear***, 225–229(1), 256–66. https://doi.org/10.1016/S0043-1648(98)00361-5
16. Ma, R., Ju, Sh., Chen, H., & Shu, Ch. (2017). Effect of Cobalt Content on Microstructures and Wear Resistance of Tungsten Carbide–Cobalt Cemented Carbides Fabricated by Spark Plasma Sintering. *IOP* ***Conference Series: Materials Science and Engineering,*** 207. DOI 10.1088/1757-899X/207/1/012019
17. Pirmohammadi, P., Zakeri, M., Razavi, M. & Nikzad, L. (2023). Effect of diamond volume fraction on the microstructure and mechanical properties of SPS WC–Co/diamond composites. ***International Journal of Applied Ceramic Technology***, 1-10. https://doi.org/10.1111/ijac.145
18. Pirso, J., Viljus, M. & Letunovitš, S. (2006). Friction and dry sliding wear behaviour of cermets. ***Wear,*** 260(7-8), 815–824. https://doi.org/10.1016/j.wear.2005.04.006
19. Quercia, G., Grgorescu, I., Contreras, H., Di Rauso, C. & Gutierrez-Campos, D. (2001). Friction and wear behaviour of several hard materials. ***International Journal of Refractory Metals and Hard Materials***, 19(4-6), 359–369. https://doi.org/10.1016/S0263-4368(01)00028-2
20. Saito, H., Iwabuchi, A., & Shimizu, T. (2006). Effects of Co content and WC grain size on wear of WC cemented carbide. ***Wear***, 261(2), 126–132. https://doi.org/10.1016/j.wear.2005.09.034
21. Van Acker, K., Vanhoyweghen, D., Persoons, R., & Vangrunderbeek, J. (2005). Influence of tungsten carbide particle size and distribution on the wear resistance of laser clad WC/Ni coatings. ***Wear***, 258(1-4), 194–202. https://doi.org/10.1016/ j.wear.2004.09.041
22. van der Merwe, R &. Sacks, N. (2013). Effect of TaC and TiC on the friction and dry sliding wear of WC–6 wt.% Co cemented carbides against steel counterfaces. ***International Journal of Refractory Metals and Hard Materials***, 41, 94–102. https://doi.org/10.1016/ j.ijrmhm.2013.02.009
23. Yaman, B. & Mandal, H. (2014). Wear performance of spark plasma sintered Co/WC and cBN/Co/WC composites. ***International Journal of Refractory Metals and Hard Materials***, 42, 9-16. https://doi.org/10.1016/j.ijrmhm.2013.10.010

Advanced Ceramics Progress: Vol. 9, No. 4, (Autumn 2023) 7-14

Materials and Energy Research Center
MERC

Contents lists available at ACERP

Advanced Ceramics Progress

Journal Homepage: www.acerp.ir

Original Research Article

Investigation on the Band Gap of Centered Square Phononic Crystals

Bentolhoda Amanat [a]*, Mohammad Reza Kazerani Vahdani [b]

[a] *Assistant Professor, Department of Physics, Payame Noor University, Tehran, Iran.*
[b] *Associate Professor, Faculty of Naval Aviation, Malek Ashtar University of Technology, Iran.*

* Corresponding Author Email: amanat@pnu.ac.ir (Bentolhoda Amanat)

URL: https://www.acerp.ir/article_181825.html

ARTICLE INFO

Article History:

Received: 17 September 2023
Revised: 22 October 2023
Accepted: 25 October 2023

Keywords:

Phononic Crystal,
Band Gap,
Piezocomposite,
Filling Fraction

ABSTRACT

The periodic structure of 1-3 piezocomposite phononic crystal minimize the effect of the coupling of parasitic modes on the deliberately excited plane modes and prevent the propagation of unwanted Lamb waves. In this article, the band structures of the centered square phononic crystals of PZT-5H rods in polyethylene terephthalate matrix was studied using the numerical method of finite elements. In particular, the phoninic band gaps of the system was investigated as the functions of the volume of the PZT element at the center of the unit cell of the considered crystal under the constant filling fraction of PZT rods. According to the results, the band structure of the system contains three gaps whose widths vary by the volume. These gaps are extended in the (normalized) frequency range of 1100-2530 m/s. Further observations particularly show that in case the all PZT rods of the system are of the same size, the maximum achievable band gap of the system will be obtained.

https://doi.org/10.30501/acp.2023.416606.1131

1. INTRODUCTION

Today, piezocomposite materials are used in many engineering applications and smart structures. The concept of piezocomposite materials was first introduced in 1978 by Newnham et al., which garnered significant attention and recognition (H. Wang et al., 2022). In piezocomposite structure, a piezoelectric material with high piezoelectric properties, such as PZT and PMN-PT, typically serves as an active phase while a polymer material, such as epoxy resin, polyethylene, etc., acts as an inactive phase (Amanat, 2022) (Lv et al., 2022). Based on the connection concept proposed by Newnham, these materials are classified into 10 types of piezocomposites (Tize Mha et al., 2021). One of the most renowned and widely used materials is 1-3 piezocomposite.

The superior properties of piezocomposites, namely low acoustic impedances (ranging from 5 MRayl to 27 MRayl), high coupling coefficients (usually in the range of 0.61 to 0.75), high bandwidth and lower Q_m, have made these materials widely applied in high frequency ultrasound transducers, medical imaging, and sonar systems (Behera, 2022) (Zhou et al., 2021). The periodic structure of piezocomposites causes the formation of specific stop bands or band gaps in the frequency spectrum of these structures. The presence of these band gaps drawn the attention of numerous scientists in recent years to the propagation of elastic waves in heterogeneous media (Y.-Z. Wang et al., 2009). In fact, the large band gaps in piezocomposites find applications in elastic and acoustic filters, transducer structures,

Please cite this article as: Amanat, B., Kazerani Vahdani, M. R., "Investigation on the Band Gap of Centered Square Phononic Crystals", ***Advanced Ceramics Progress***, Vol. 9, No. 4, (2023), 7-14. https://doi.org/10.30501/acp.2023.416606.1131

control of noise, and vibration shields (Vatanabe & Silva, 2011). For instance, by tuning the frequency of the thickness mode of piezocomposites within these band gaps, it is possible to minimize coupling with parasitic modes, such as lateral modes, and prevent the propagation of Lamb waves. Consequently, substantial research efforts have been devoted to broadening the band gap widths (Sigmund & Jensen, 2003) (Wu et al., 2009), a characteristic which strongly depends on the physical properties, size, and shape of constituent phases (Miranda & Dos Santos, 2022).

Hou et al. (Hou et al., 2004) investigated the elastic band gap structure of a two-dimensional acoustic crystal containing piezoelectric materials and analyzed the piezoelectric effects on the band gaps. Qian et al. (Z. Qian et al., 2004) studied the dispersion relations of horizontal shear wave propagation in a periodic layered piezoelectric structure for cases of wave propagation in normal and tangential directions to the interface. Silva et al. (Vatanabe et al., 2014) attempted to maximize the absolute elastic wave gap width in designed piezocomposite materials using topology optimization. Zheng Hua et al. (Z.-H. Qian et al., 2008) compared the band gaps in two-dimensional piezocomposite with 1-3 connection family of piezoceramic rods, which had circular and square cross-sections. Sigmund (Sigmund & Jensen, 2003) (Thompson & Sigmund, 2000) applied the topology optimization to design periodic materials and structures with acoustic band gaps to minimize the structural response along the boundaries or maximize the response at certain boundary points. Halkjer et al. (Halkjaer et al., 2005) maximized the acoustic band gap for infinite periodic beam structures modeled based on Timoshenko beam theory, considering alternating, thick and medium thickness plates, and finite thick plates. Jensen et al. (Halkjær et al., 2006) extended the bandgap size for shear waves in the Mindlein plane. Evgrafov et al. (Rupp et al., 2007) applied topology optimization to the design of 2D and 3D phononic (elastic) materials, focusing on the surface wave filters and waveguides. Other different aspects related to the propagation of sound waves in two- and three-dimensional piezoelectric periodic structures have been addressed in several research studies (Vashishth & Gupta, 2009) (Y.-Z. Wang et al., 2007) (Y.-S. Wang, 2008) (Vu Quoc et al., 2021).

Most of the past research projects were primarily based on three main axes: a) adjusting the piezoceramic filling fraction, leading to changes in the piezocomposite parameters such as coupling coefficient, characteristic impedance, effective density, and longitudinal velocity; b) altering the geometric shape of piezoceramics and using different geometric shapes (this method lacks precise control over the band gap adjustment); c) modifying the constituents of the piezocomposite, which, like the second case, results in a sudden change in the band gap parameters, hence the challenge of precise control over the band gap adjustment.

This research aims to propose a 1-3 piezocomposite of centered cubic crystal structure and investigate the effect of the volume fraction of different phases of piezoelectric rods on the band gaps while maintaining a constant ceramic filling fraction. In this analysis, Bloch-Flocke theory (Comi & Marigo, 2020) and finite element analysis were employed to study the dynamic behavior of two-dimensional piezocomposite unit cells for calculation of the band gap. A structure was also presented in this paper that allows control over the width of band gaps without altering the filling fraction, solely by changing the ηs. According to the observations, the maximum gap bandwidth was achieved in the case of η=50%.

2. Problem explanation and finite element modeling

The system under study is a 1-3 piezocomposite structure consisting of a square lattice of lattice constant "a". The unit cell comprises a pair of rods made from PZT-5H with circular cross-section and different radii, distinguishable by white and gray color, as shown in Figure 1. These PZT rods are embedded in a polymer matrix of polyethylene terephthalate.

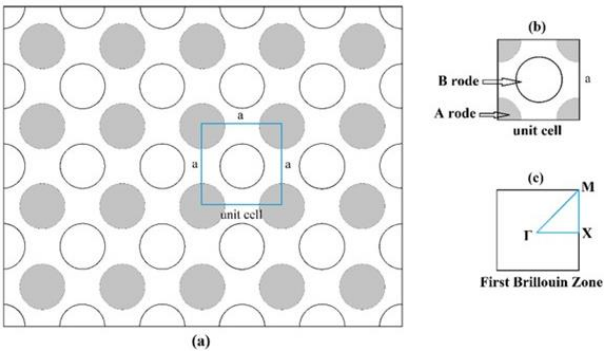

Figure 1. According to the schematic, (a) the proposed 1-3 piezocomposite network model, (b) the unite cell of the network, (c) the first Brillouin zone. Gray circles represent rode A and white circles rode B. we change the size of the gray and white circles while maintaining the filling fraction of the piezocomposite constant.

Due to the crystal periodicity and its infinite size along the x and y axes, the mechanical displacements (u_i) and electric potential (φ) follow the Bloch relation (Equations (1-2)) [15]:

$$u_i(x+ma_1,y+pa_2) = u_i(x,y,z)\exp(-jk_xma_1)\exp(-jk_ypa_2) \quad (1)$$

$$\varphi(x+ma_1,y+pa_2) = \varphi(x,y,z)\exp(-jk_xma_1)\exp(-jk_ypa_2) \quad (2)$$

where "kx" and "ky" represent the components of the Bloch wave vectors in the x and y, respectively, while m

and p are integers.

These periodical boundary conditions allow us to confine the calculations just to a single unit cell. The square unit cell of the system is also taken into account, as depicted in Figure 1-b. The cell consists of two different rode: rod A, represented by four quarter circles with the radius R_A at the corners, and rod B, a full circle with the radius R_B in the center. The polarization axis of the piezoelectric rods is considered perpendicular to the unit cell plane.

For the considered piezocomposite, the filling fraction of the piezoceramics phase, defined as the ratio of the volume of the piezocomposite rods in the unit cell to the total volume of the unit cell, is given by Equation (3).

$$(\pi(R_A^2 + R_B^2)/a^2) \tag{3}$$

Additionally, we define the volume fraction of the rod B as the ratio of the volume of rod B to the summation of the volume of the rods A and B in a unit cell, denoted by η (Equation (4)). Based on the radius of the rods, we have:

$$\eta = \frac{R_B^2}{R_A^2 + R_B^2} \tag{4}$$

The main objective of this paper is to investigate the band structures of the mentioned phononic crystal as a function of η in order to determine the optimal value of η for achieving the maximum band gap. To simplify the analysis, the filling fraction is held constant at 50% throughout this research. In other words, as the R_b increases by increasing η, R_a must decrease in such a way that the filling fraction remains constant.

Given the complex topology of this structure, a numerical method, such as the Finite Element Method (FEM), is essential to analyze the vibrational properties of the structure.

The finite element numerical method is well established for linear piezoelectric materials and has been widely used in the analysis of piezocomposites. For this reason, FEM was employed in this study to investigate the band structures of the considered composite. To this end, the unit cell is divided into a mesh of triangular elements connected by nodes as represented schematically in Figure 2.

In the absence of external forces and considering a monochromatic time dependent exp(jωt), the general piezoelectric problem is expressed by Equation (5) [14].

$$\begin{bmatrix} K_{uu} - \omega^2 M_{uu} & K_{\varphi u} \\ K_{\varphi u} & K_{uu} \end{bmatrix} \begin{pmatrix} u \\ \varphi \end{pmatrix} = \begin{pmatrix} 0 \\ 0 \end{pmatrix} \tag{5}$$

where K_{uu} and M_{uu} denote the stiffness and mass matrices of the fully elastic part of the problem, respectively. In addition, $K_{\varphi\varphi}$ and $K_{u\varphi}$ represent the pure dielectric part and piezoelectric coupling matrix, respectively. As mentioned earlier, the translational symmetry of the lattice allows us to mitigate the problem of the first Brillouin zone, as depicted in Figure 1 (b). To obtain the dispersion diagrams, the wave vector varies within the first Brillouin zone for a given propagation direction which as usual can be reduced using the symmetry properties of the system to the first irreducible Brillouin zone. For a square lattice of constant "a", the first Brillouin zone is defined by $-\pi/a<kx<\pi/a$ and $-\pi/a<ky<\pi/a$. The band structures are calculated along the M-Γ-X-M path (see Figure 1(c)). To ensure the accuracy of the results, the mesh sizes have been refined repeatedly until the angular frequency convergence is achieved.

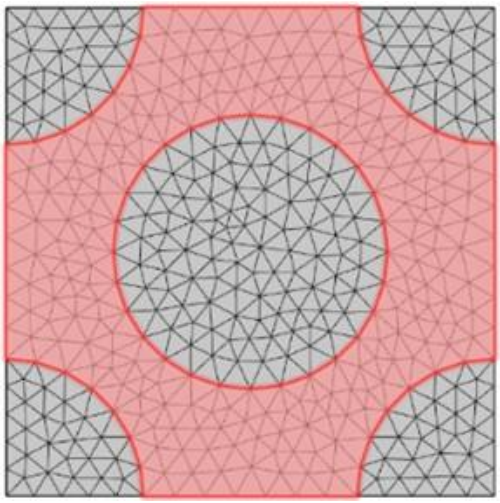

Figure 2. A view of a meshed unit cell

2. NUMERICAL SIMULATION AND DISCUSSION

This section presents and discusses the results of varying the volume fraction η and its effects on the band structure of the piezoelectric phononic crystal, introduced in the previous sections. We maintain the total filling fraction of the PZT-5H rods at a constant value of 50% while altering the η from 0 to 50%. The band structures are obtained by calculating the lowest 20 bands of the system using the finite element analysis. The material parameters used in the calculations are tabulated in Table 1, the results of which are as follow. It should be noted that since the rods within a unit cell consist of the same type of piezoceramic material, i.e., PZT-5H, we expect that the band structure for η values greater than 50% will resemble those for η<50%. In the other words, for example, the band structure of η=70% matches that of η=30% because the only difference between the unit cell in this case lies in the volumes of rods A and rods B. The bands are calculated along the path M-Γ-X-M about the irreducible Brillouin zone of the square lattice and are plotted in terms of the product of frequency and lattice

constant f × a versus the wave vector K along the first irreducible Brillouin zone, as seen in Figure 1-c. It is evident that the existing band gaps extend across the Brillouin zone, as stated by Vasseur et al. [24].

TABLE 1. Characteristics of the materials used in the calculations (Vasseur et al., 1994) (Z.-H. Qian et al., 2008)

		PZT-5H		polyethylene terephthalate
Elastic constants ($10^9 Nm^{-2}$)	C_{11}	121	Young's modulus	7×10^9
	C_{33}	117		
	C_{44}	23		
	C_{13}	84.1		
	C_{12}	79.5		
Piezoelectric constants (Cm^{-2})	e_{15}	17	Poisson's ratio	0.44
	e_{31}	-6.5		
	e_{33}	23.3		
Dielectric constants (10^{-10} F m^{-1})	ε_{13}	150	Mass Density (kg/ m^{-3})	1430
	ε_{33}	130		
Mass Density (kg/ m^{-3})	ρ	4500		

Figure 3 illustrate the band structures of the considered 1-3 piezocomposite in the limiting case η=0, which corresponds to a simple square lattice. As observed in Figure 3, there is a single complete band gap between the third and fourth bands. The gap extended in the frequency range 1100<f.a<1500 with relative bandwidth 31%.

As the η values exceeds zero, the volume of rod B starts to grow from zero as well, and due to the constant filling fraction 50%, the volume of rod A decreases.

Figure 4 (a) depicts the band structure for η=5%. In this case, the magnitude of the band gap between the third and fourth bands decrease to 209m/s. This band spans from 1105 m/s to 1314 m/s with the relative bandwidth 17%. Although this gap narrows as η increases from zero, another band gap begins to appear between the tenth and eleventh bands. This new gap falls within the frequency range of 2296 m/s to 2527 m/s with the relative band gap of 9.8%. The presence of the later gap can be attributed to the emergence of rods B in the middle of the unit cell, rather than a decrease in the volumes of rod A. To confirm this, we evaluated the band structures for very small values of η, not shown here, and observe that the later gap starts to grow immediately as η increases from zero. Given that for these small values of η, the volume of rod A does not change considerably, it is reasonable to attribute this band gap to the new scattering center produced in each unit cell. (The number in the right of each figure is the bandwidth of band gap)

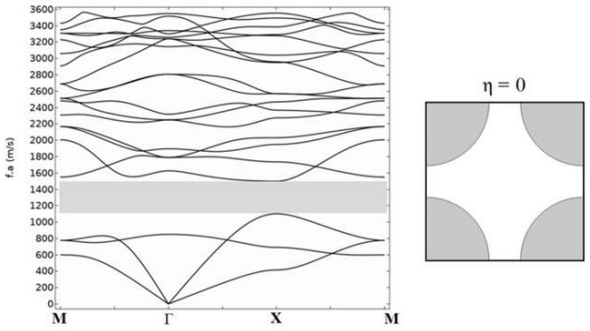

Figure 3. Dispersion diagram and elastic band structure for XY vibration modes in a typical 1-3 piezocomposite in 50% piezoceramic filling fraction, which does not have rode A circles (η=0)

TABLE 2. Specifications of materials used and different values of η

Figure	η	Polymer material	piezoceramic material	Piezoceramic filing fraction
3	0	polyethylene terephthalate (PET)	PZT-5H	50
2-(a)	5			
2-(b)	10			
2-(c)	20			
2-(d)	30			
2-(e)	40			
2-(f)	50			

Upon increasing η up to 10%, a third gap begins to emerge, as presented in Figure 4 (b). As indicated in this figure, this gap lies between the 6th and 7th bands with a lower edge at 1737m/s and relative bandwidth of 0.4%. In this case, while the lower limit of first band gap remains unchanged compared to the η =5% case, its band width decreases by 95m/s due to the descending 4th band. Contrarily, the second band gap now grows to 262m/s with the relative bandwidth of 10.9% due to the descending 10th and ascending 11th bands.

With a further increase in η up to 20%, the first band gap is closed completely as a result of the downward movement of the fourth band (in addition to the fifth and sixth bands), although the first, second, and third bands remain almost unchanged. As presented in Figure 4c, the bandwidth of the 2nd band gap shrinks symmetrically to

131 m/s, with its lower edge increasing up to 2362 m/s. On the other hand, although both the maximum of 6th band (1597m/s) and the minimum of 7th band (1791m/s) have decreased, the width of the 3rd band width increases up to 194m/s.

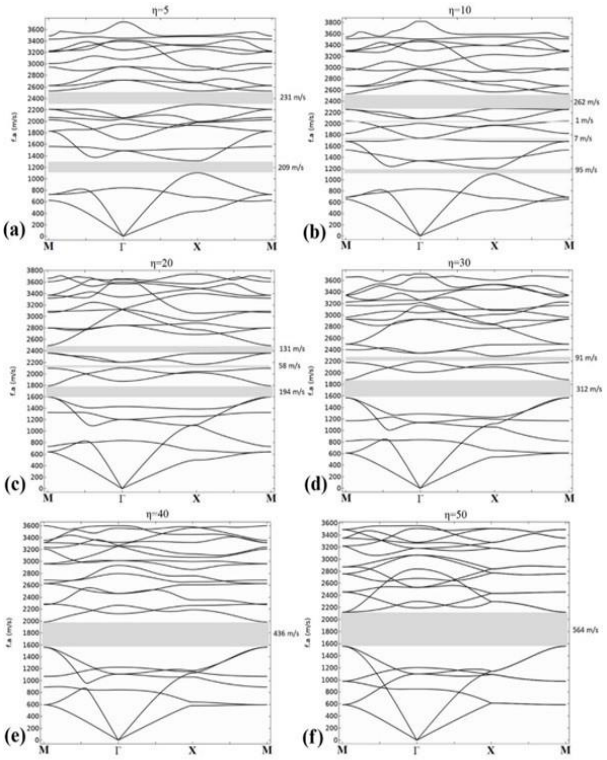

Figure 4. Dispersion diagram and elastic band structure for XY vibration modes in a typical 1-3 piezocomposite in 50% piezoceramic filling fraction

The width of the 3rd band gap grows continuously as η increases up to 50% and reaches its maximum, as depicted in Figures. 4-b, c, d, e, f. At η=50%, the 3rd gap extends in the frequency range of 2122<f.a<1558 with the band width of 564m/s and relative bandwidth of 31%. Since the 5th and 6th bands remain almost unchanged, the widening of this gap occurs as a direct result of the shift of 7th band to the higher frequencies. In addition, there is a narrower band gap just above the 7th band from η=10% to η=40%, as depicted in Figure 4-b, c, d, which is faded as η increases up to 40%. The maximum relative bandwidth of this gap is 4.3% while its minimum relative bandwidth at 2234m/s occurs at M point of Brillouin zone for η=35% (show in Figure 6). An interesting feature of the case η=50% is the dual degeneracy of each band in the X-M range. In other words, the six bands in the range of M-Γ to Γ-X converge in such a way that only three bands are observable in the X-M range. This happens mainly because for η=50%, the centered square lattice under consideration is transformed into a simple square lattice of lattice constant $a/\sqrt{2}$ whose axis rotates π/4 with respect to the axis of the centered square lattice considered so far. Figure 5 depict the Brillouin zones of this lattice as well as the original centered square. Calculation of the band structure of the simple square lattice mentioned above along with the (unconventional) directions of Figure 5 shows complete match with the η=50% case.

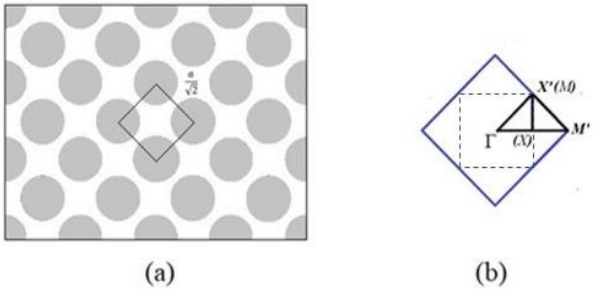

Figure 5. According to the schematic, (a) the unit cell of simple square lattice associated with = 50% (solid line), (b) The B.Z. corresponding to the simple square in addition with the B.Z. of a centered square lattice constant a of Figure 1 (The dotted lines show the Brillouin zone in Figure 1)

TABLE 2. Specifications of each band gap for different η

	1st Band gap			2nd Band gap			3rd Band gap		
η	Band end (m/s)	Band start (m/s)	Bandwidth (m/s)	Band end (m/s)	Band start (m/s)	Bandwidth (m/s)	Band end (m/s)	Band start (m/s)	Bandwidth (GHz)
0	1500	1100	400						
5	1314	1105	209	2527	2296	231			
10	1202	1107	95	2530	2268	262	1744	1737	7
15	1138	1110	28	2518	2306	212	1772	1665	107
20				2493	2362	131	1791	1597	194
25				2457	2424	33	1829	1580	249
30							1881	1569	312
35							1931	1564	367
40							1984	1548	436
45							2052	1559	493
50							2122	1558	564

In short, information of the gaps in the above-mentioned phononic crystals has been accumulated and plotted as functions of η in Figure 6. As shown in this figure, the maximum width of the first band gap, equal to 400m/s, occurs at η=0, and the gap dissolves above η=20%. In the mid-range, the second band gap dominates from η =5% up to η≈18%, with a maximum of 262m/s at η=10%. The third and the long-lasting gap start at η=10% and exists until η=50% with a maximum of 564 m/s at η=50%. The width of latter gap grows continuously with η, making it the dominant gap above η≈18%. There is also a minor gap which appears above η=10% with a

maximum not exceeding 98m/s. Finally, it should be noted that despite the nearly equal maximums of the first and second band gaps, the largest band gap, achievable by modifying the volume ratio of rode A with respect to rode B, belongs to third gap at η=50%.

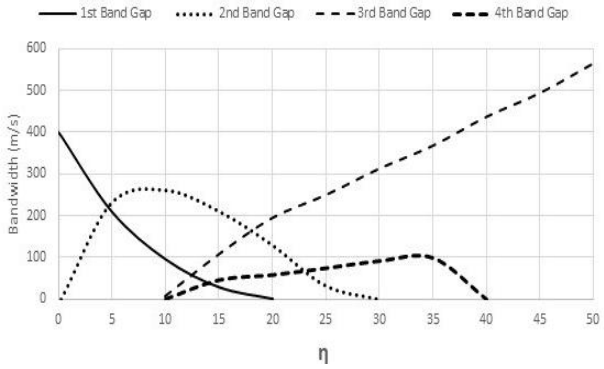

Figure 6. The width of the first five bands in terms of different values of η at the filling fraction F=50%

This property is detailed in Figure 7 which depicts the upper and lower boundaries corresponding to each gap as a function of η. As shown in this figure, the first and second band gaps lies in the frequency ranges of 1500 m/s-1100 m/s and 2268 m/s-2530 m/s, respectively, with the third gap in between ranging from 1558 m/s to 2122 m/s. Of note, no gap exists below the lower frequency limit of first gap and above the higher frequency limit of the second band gap (although it has been tested but not presented here by considering 50 bands in our calculations).

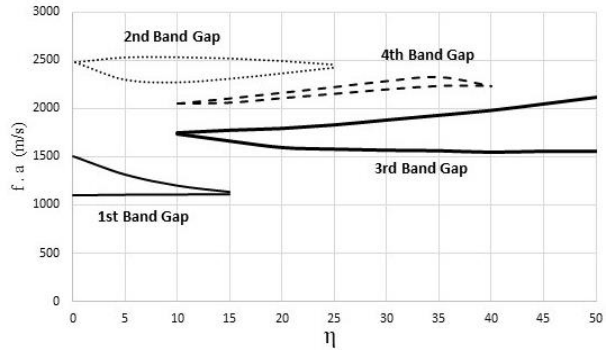

Figure 7. The open points, close points and width of the band gaps at the filling fraction F=50% versus η

We calculated the density of states in the entire Brillouin zone, which is shown as an example of the results obtained for a filling fraction=50% and eta = 50% in Figure 8. According to the obtained results, this gap is spread throughout the Brillouin zone. The presence and magnitude of this gap in the elastic band structure and density of state clearly show that this band gap extends throughout the Brillouin zone.

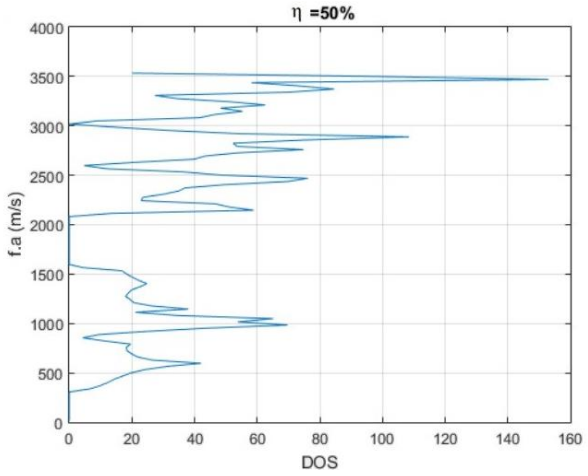

Figure 8. The density of states at the filling fraction F=50% versus η=50%

The bandwidth, lower and upper limits, and opening and closing points of each band gap in different η values are easily detectable in Figure 7. In the first and third band gaps, the lower limit of the band gap is almost constant, and their changes are mainly caused by changes in their upper limit. According to Figure 4, the first, second, and third bands remain stable and unchanged and with the movement of the fourth, fifth, and sixth modes, the first band gap closes. After the first band gap closes, these modes remain almost constant and unchanged, thus playing a role as the lower limit of the third band gap. With the stability of these modes, the main changes in the bandwidth of the third band result from the upward movement of the higher bands. In other words, in case the bandwidth of the third band gap increases, the first to sixth modes remain constant and unchanged, and the main change of this band gap results from the upward movement of the seventh, eighth, ninth, and tenth bands. In general, it can be concluded that addition of the rode A creates new boundary conditions and excites lateral modes, and these new boundary conditions lead to changes in the band gaps.

As shown in Figure 4, by changing the η while maintaining the filling fraction of the piezoceramic rods, the dispersion diagram of the piezocomposite changes, showing that the band gaps are highly sensitive to these changes, and this parameter can be adjusted to obtain a larger relative bandwidth in the desired frequency range.

Upon comparing Figure 3 (η=0) with other figures, it can be concluded that this method allows us to create band gaps in different frequency ranges and different widths. In addition, in the η=50 (Figure 4 (f)), the bandwidth of the band gap is 1.43 times that of the mode without rode B (η =0) (Figure 3). In some values of η, we have two or three bands at the same time at different frequency ranges. According to the diagrams, the changes in the bands are attributed to the displacement of higher modes and their movement towards higher or

lower frequencies. In this respect, it can be concluded that the non-uniform volume distribution of piezoceramic rods cause these changes.

With the increase of η, phase b elements appear from zero while their effect gradually increases. These elements are located between the elements of phase A, reducing the distance between then, and as a result. As a result, it is expected that the forbidden gap at low frequencies will gradually disappear and shift to higher frequencies. As observed in Figure 4, this effect occurs by transferring the frequency modes to the forbidden gap. While the energy of the lowest three frequency bands remains almost constant, the frequency of its upper edge gradually decreases.

The first energy gap is caused by the destructive combination of waves moving in the x or y direction and being partially reflected from the plates containing the phase A elements. Reducing the volume of phase A elements and increasing the effect of phase B elements on these reflections upon increasing η reduces the size of this gap until finally it disappears for η=15 by decreasing the energy of the fourth frequency band.

On the other hand, the second frequency gap appears immediately with an increase in η from zero. Due to the high frequency of this gap, its creation can be attributed to the destructive combination of waves that move perpendicular to the planes of phases a and b (along the x or y axes) and are partially reflected from these phases. Initially, the width of this gap increases with an increase in η bit it ultimately closes by reducing the frequency of its upper edge and increasing the energy of its lower edge at η=0.25.

The third energy gap, which is the main focus in this research, starts to appear from η=10. This gap is created by the destructive superposition of waves that move along the bisector of the x and y axes and being partially reflected from the phase elements A and B. Increasing the volume of phase B and the simultaneously decreasing the volume of phase A with an increase in η bring the volume of these two elements closer together. As a result, the width of the gap increases continuously with the increase of η until at η=50, where the volume of the two elements becomes equal, the gap reaches its maximum value. At η=50, the final grid is a simple square grid, rotated by 45 degrees relative to the initial grid at η=0, and the distance between its elements is a/sqrt (2). Hence, the width of the gap in this case is sqrt (2) times that of η=0.

We calculated the entire inverted space and observed that this gap has extended throughout entire inverted space.

In previous research, such as the study by Zhang Hua et al. [15], changes in the filling fraction of piezoceramic were typically used to alter the bandgap, resulting in changes in the functional characteristics of the piezoceramic, such as effective electromechanical coupling coefficient, characteristic impedance, longitudinal velocity, and density. However, in this case, without changing the piezoceramic filling fraction, the bandwidth and location of the band gaps can be controlled without changing the piezoceramic filling fraction, allowing for the desired bandwidth and location based on practical needs.

3. CONCLUSION

In the current research, the phononic band structures of a two-dimensional body center 1-3 piezocomposite consisting of PZT-5H rod and polyethylene terephthalate polymer matrix were theoretically investigated. The volume fraction of the PZT rods was assumed to be constant as 50% to examine the band structure of the system as a function of the ratio η, representing the volume fraction of the PZT rod at the center of a unit cell relative to the total volume of the PZT rods in the unit cell. The results revealed that in the whole range of variation of η, there was at least one complete band gap in the band structure of the considered structure while detecting no gaps below f.a=110 m/s and above f.a=2530 m/s. Moreover, the band structure contained three main band gaps (in addition to two minor ones) that reached their maximum values at η=0% (first band gap), η=20% (second band gap), and η=50% (third band gap), the latter is the largest band gap (equal to 564m/s) of the considered system.

ACKNOWLEDGEMENTS

The authors would like to acknowledge Payame Noor University and Malek Ashtar University for all supports throughout this work.

REFERENCES

1. Amanat, B. (2022). "Improvement of the Effective Parameters of 1-3 Piezocomposite Using Multi-Layer Polymer and PMN-PT Relaxor Single Crystal." ***Advanced Ceramics Progress***, 8(2), 61–72. https://doi.org/10.30501/acp.2022.355196.1099
2. Behera, A. (2022). "***Piezoelectric Materials. In A. Behera (Ed.), Advanced Materials: An Introduction to Modern Materials Science***", (pp. 43–76). Springer International Publishing. https://doi.org/10.1007/978-3-030-80359-9_2
3. Comi, C., & Marigo, J.-J. (2020). "Homogenization Approach and Bloch-Floquet Theory for Band-Gap Prediction in 2D Locally Resonant Metamaterials." ***Journal of Elasticity***, 139. https://doi.org/ 10.1007/s10659-019-09743-x
4. Halkjaer, S., Sigmund, O., & Jensen, J. (2005). "Inverse design of phononic crystals by topology optimization." ***Zeitschrift Fur Kristallographie - Z KRISTALLOGR***, 220, 895–905. https://doi.org/ 10.1524/zkri.2005.220.9-10.895
5. Halkjær, S., Sigmund, O., & Jensen, J. (2006). "Maximizing band gaps in plate structures." ***Structural and Multidisciplinary Optimization***, 32, 263–275. https://doi.org/10.1007/s00158-006-0037-7
6. Hou, Z., Wu, F., & Liu, Y. (2004). "Phononic crystals containing piezoelectric material.", ***Solid State Communications***, 130(11), 745–749. https://doi.org/10.1016/j.ssc.2004.03.052
7. Lv, J., Xie, X., Zhu, X., Li, Z., Han, Z., Cui, Y., Zhang, B., & Jian, X. (2022). "Cold ablated high frequency PMN-PT/Epoxy 1-3 composite transducer.", ***Applied Acoustics***, 188, 108540. https://doi.org/10.1016/j.apacoust.2021.108540

8. Miranda, E. J. P., & Dos Santos, J. M. C. (2022). "Wave attenuation in 1-3 phononic structures with lead-free piezoelectric ceramic inclusions.", ***Physica B: Condensed Matter***, 631, 413642. https://doi.org/10.1016/j.physb.2021.413642
9. Qian, Z., Jin, F., Wang, Z., & Kishimoto, K. (2004). "Dispersion relations for SH-wave propagation in periodic piezoelectric composite layered structures.", ***International Journal of Engineering Science***, 42(7), 673–689. https://doi.org/10.1016/j.ijengsci.2003.09.010
10. Qian, Z.-H., Jin, F., Li, F.-M., & Kishimoto, K. (2008). "Complete band gaps in two-dimensional piezoelectric phononic crystals with {1–3} connectivity family.", ***International Journal of Solids and Structures***, 45(17), 4748–4755. https://doi.org/10.1016/j.ijsolstr.2008.04.012
11. Rupp, C., Evgrafov, A., Maute, K., & Dunn, M. (2007). "Design of phononic materials/structures for surface wave devices using topology optimization.", ***Structural and Multidisciplinary Optimization***, 34, 111–121. https://doi.org/10.1007/s00158-006-0076-0
12. Sigmund, O., & Jensen, J. (2003). "Systematic design of phononic band-gap materials and structures by topology optimization.", ***Philosophical Transactions. Series A, Mathematical, Physical, and Engineering Sciences***, 361, 1001–1019. https://doi.org/ 10.1098/rsta.2003.1177
13. Thompson, J. M. T., & Sigmund, O. (2000). "Topology optimization: A tool for the tailoring of structures and materials.", ***Philosophical Transactions of the Royal Society of London. Series A: Mathematical, Physical and Engineering Sciences***, 358(1765), 211–227. https://doi.org/10.1098/rsta.2000.0528
14. Tize Mha, P., Maréchal, P., Ntamack, G. E., and Charif d'Ouazzane, S. (2021). "Homogenized electromechanical coefficients and effective parameters of 1–3 piezocomposites for ultrasound imaging transducers.", ***Physics Letters A***, 408, 127492. https://doi.org/ 10.1016/j.physleta.2021.127492
15. Vashishth, A. K., & Gupta, V. (2009). "Wave propagation in transversely isotropic porous piezoelectric materials.", ***International Journal of Solids and Structures***, 46(20), 3620–3632. https://doi.org/10.1016/j.ijsolstr.2009.06.011
16. Vasseur, J. O., Djafari-Rouhani, B., Dobrzynski, L., Kushwaha, M. S., & Halevi, P. (1994). "Complete acoustic band gaps in periodic fibre reinforced composite materials: The carbon/epoxy composite and some metallic systems.", ***Journal of Physics Condensed Matter***, 6, 8759–8770. https://doi.org/10.1088/0953-8984/6/42/008
17. Vatanabe, S. L., Paulino, G. H., & Silva, E. C. N. (2014). "Maximizing phononic band gaps in piezocomposite materials by means of topology optimization.", ***The Journal of the Acoustical Society of America***, 136(2), 494. https://doi.org/10.1121/1.4887456
18. Vatanabe, S. L., & Silva, E. C. N. (2011). "Design of phononic band gaps in functionally graded piezocomposite materials by using topology optimization.", ***Behavior and Mechanics of Multifunctional Materials and Composites*** 2011, 7978, 268–277. https://doi.org/10.1117/ 12.878851
19. Vu Quoc, T., Do Ba, D., Tran Thi Thuy, D., Nguyen Ngoc, L., Nguyen Thuy, C., Vu Thi, H., Khanh, L. D., Doan Thi Yen, O., Thai, H., Long, V. C., Talu, S., & Nguyen Trong, D. (2021). "DFT study on some polythiophenes containing benzo[d]thiazole and benzo[d]oxazole: Structure and band gap.", ***Designed Monomers and Polymers***, 24(1), 274–284. https://doi.org/10.1080/15685551.2021.1971376
20. Wang, H., Li, Y., Hui, H., & Rong, T. (2022). "Analysis of electromechanical characteristics of the 1-3-2 piezoelectric composite and 1-3-2 modified structural material.", ***Ceramics International***, 48(15), 22364–22375. https://doi.org/10.1016/j.ceramint.2022.04.238
21. Wang, Y.-S. (2008). "Calculation of band structures for surface waves in two-dimensional phononic crystals with a wavelet-based method.", ***Phys. Rev. B***, 78. https://doi.org/10.1103/PhysRevB.78.094306
22. Wang, Y.-Z., Li, F.-M., Huang, W.-H., & Wang, Y.-S. (2007). "Effects of inclusion shapes on the band gaps in two-dimensional piezoelectric phononic crystals.", ***Journal of Physics: Condensed Matter***, 19, 496204. https://doi.org/10.1088/0953-8984/19/49/496204
23. Wang, Y.-Z., Li, F.-M., Kishimoto, K., Wang, Y.-S., & Huang, W.-H. (2009). "Wave band gaps in three-dimensional periodic piezoelectric structures.", ***Mechanics Research Communications***, 36(4), 461–468. https://doi.org/10.1016/j.mechrescom.2009.01.003
24. Wu, M.-L., Wu, L.-Y., Yang, W.-P., & Chen, L.-W. (2009). "Elastic wave band gaps of one-dimensional phononic crystals with functionally graded materials.", ***Smart Materials and Structures***, 18, 115013. https://doi.org/10.1088/0964-1726/18/11/115013
25. Zhou, C., Zhang, J., Liu, D., & Zhang, Z. (2021). "Novel 1–3 (K,Na)NbO_3-based ceramic/epoxy composites with large thickness-mode electromechanical coupling coefficient and good temperature stability.", ***Ceramics International***, 47(4), 4643–4647. https://doi.org/ 10.1016/j.ceramint.2020.10.031

Advanced Ceramics Progress: Vol. 9, No. 4, (Autumn 2023) 15-21

Materials and Energy Research Center
MERC

Contents lists available at ACERP

Advanced Ceramics Progress

Journal Homepage: www.acerp.ir

Original Research Article

Effect of Fluorine Doping on LiCoO2 Cathode Material: a DFT Study

Hatef Yousefi Mashhour [a], Mohammad Mahdi Kalantarian [b]*, Afshin Namiranian [c]*

[a] *Ph.D. Candidate, Faculty of Physics, Iran university of science and technology, P.O. Box 13114-16846, Tehran, Iran.*

[b] *Assistant professor, Department of Ceramic, Materials and Energy Research Center, Karaj, Iran.*

[c] *Associate Professor, Faculty of Physics, Iran university of science and technology, P.O. Box 13114-16846, Tehran, Iran.*

* Corresponding Author Email: kalantarian@gmail.com and m.kalantarian@merc.ac.ir (Mohammad Mahdi Kalantarian), Afshinn@iust.ac.ir (Afshin Namiranian)
URL: https://www.acerp.ir/article_184372.html

ARTICLE INFO

Article History:

Received: 18 November 2023
Revised: 01 December 2023
Accepted: 02 December 2023

Keywords:

Li-ion Batteries,
Cathode Materials,
Density Functional Theory,
Density of States,
Doping

ABSTRACT

This study employs density functional theory (DFT) in order to investigate the fluorine doping effects on the structural, electrochemical and electrical, properties of $LiCoO_2$ cathode materials for LIBs. The research reveals that fluorine substitution with oxygen can significantly enhance the performance and stability of $LiCoO_2$ in multiple aspects. Investigation show that the fluorine doping results in n-type doping and Fermi level increases in electron density of states, which may enhance the electrical conduction. The substitution of fluorine modifying the cycling life of battery and improves the structural stability by suppressing the expansion rate of volume and increasing the lattice parameter along the *c*-axis during full delithiation. The findings demonstrate that the fluorine doping improves the structural stability of $LiCoO_2$ by decreasing volume shrinkage during the delithiation. Accordingly, the study identifies the most stable fluorine substitution site, located furthest from the lithium layer. Consistent results from calculations using different approaches (internal and Fermi energy) and methods (GGA and GGA+U) confirm that $LiCoO_{2-x}F_x$ exhibits lower voltage compared to $LiCoO_2$, making it desirable for electrolyte tolerance and prolonged battery lifetime. Evaluation of electrical properties demonstrates that the fluorine doping enhances the electrical conductivity of $LiCoO_2$ by reducing the band gap and charge carrier transfer barrier (CCTB). The examination of intrinsic and extrinsic band gaps, as well as Delta and CCTB approaches, consistently reveals that $LiCoO_{2-x}F_x$ exhibits a lower band gap and CCTB, indicating improved rate-capability and electrical conductivity.

https://doi.org/10.30501/acp.2023.425848.1139

1. INTRODUCTION

In the present era, lithium-ion batteries (LIBs) have emerged as the predominant power source for portable electric devices (Kim, Song, Son, Ono, & Qi, 2019). However, the current commercially utilized cathode materials suffer from limited reversible capacity, exemplified by Layered $LiNi_{1/3}Mn_{1/3}Co_{1/3}O_2$ (150-160 mAhg-1), $LiCoO_2$ (~140 $mAhg^{-1}$), olivine $LiFePO_4$ (~160 $mAhg^{-1}$ and spinel $LiMn_2O_4$ (~120 $mAhg^{-1}$),) (Barkholtz et al., 2019; Blomgren, 2016; Ellis, Lee, & Nazar, 2010). This constraint poses a significant obstacle to the advancement of Li-ion cathode materials.

Among the existing cathode materials, lithium cobalt oxide ($LiCoO_2$) is widely employed in the current LIB industry (Mizushima, Jones, Wiseman, & Goodenough, 1980; Nagaura, 1990). Its layered structure offers advantages such as satisfactory energy and power densities, high rate capacity, and reasonable reversibility. Nonetheless, the structural stability of $LiCoO_2$ cathodes during charging and discharging poses a substantial challenge. Recent investigations have revealed notable

Please cite this article as: Yousefi Mashhour, H., Kalantarian, M. M., Namiranian, A. "Effect of Fluorine Doping on LiCoO2 Cathode Material: a DFT Study", ***Advanced Ceramics Progress***, Vol. 9, No. 4, (2023), 15-21. https://doi.org/10.30501/acp.2023.425848.1139

lattice expansion along the c axis during delithiation, while the contraction rate reaches up to just 10% for complete deintercalation (G. Amatucci, Tarascon, & Klein, 1996; Momeni, Mashhour, & Kalantarian, 2019; Reimers & Dahn, 1992). This non-uniform variation of lattice exceeds the elastic strain tolerance of cobalt oxides, which is approximately 0.1%, resulting in mechanical fractures that adversely affect battery capacities over prolonged operation periods (Dokko et al., 2000; Thackeray, 1995; H. Wang, Jang, Huang, Sadoway, & Chiang, 1999).

To address this issue, substitutional doping sites of Co with various transition metals has been explored to improve the structural stability of $LiCoO_2$ during the deintercalation process (Fergus, 2010; Jones, Rossen, & Dahn, 1994; Kobayashi et al., 2000; Needham, Wang, Liu, Drozd, & Liu, 2007). Notably, the substitution of Co species with Mg and La has demonstrated effective retention of the layered structure, suppression of phase transitions during Li lithiation/delithiation, and significant improvements in performance of cycling for LIBs (Zhu et al., 2014). Materials with doping showed minor capacity fade and much higher columbic efficiency compared to pristine $LiCoO_2$ (Thirunakaran, Kim, & Yoon, 2014). Conversely, doping with V, Cr, Mo, and Zr leads to a deficient $LiCoO_2$ structure and irreversible capacity loss in the initial cycle (Needham et al., 2007).

On the other hand, substitutional doping of oxygen sites with anionic elements, such as halogens, has received not as much of attention, while it can be promising strategy. Studies have indicated that fluorine substitution with oxygen also impacts the structural properties of cobalt and nickel oxides (G. G. Amatucci & Pereira, 2007; Naghash & Lee, 2001). F-doped $LiNiO_2$ was found to remove abrupt changes in distortion of lattice and remarkably improve the cycling life of LIBs (Kubo, Fujiwara, Yamada, Arai, & Kanda, 1997). Also, $LiNi_xCo_yMn_{1-x-y}O_{2-z}F_z$ ($0 \leq z \leq 0.1$) compounds show improved structural stability without phase transitions during deintercalation, demonstrating excellent cycling performance and rate capacity compared to fluorine-free compounds (Lee et al., 2015).

Utilization of DFT in battery research has revolutionized the field by providing a influential tool for the rational characterization and design of materials (Cohen, Mori-Sánchez, & Yang, 2011; Guillén-López, Espinosa-Torres, Cuentas-Gallegos, Robles, & Muñiz, 2018; Perdew et al., 2017; Ullah, Majid, & Rani, 2018). Its ability to predict material properties, investigate electrochemical processes, and analyze interfaces have significantly accelerated the development of high-performance batteries. By combining theoretical predictions with experimental validation, researchers can drive the discovery of next-generation battery technologies, leading to more efficient, longer-lasting, and safer energy storage devices. (Assat & Tarascon, 2018; A. Wang, Kadam, Li, Shi, & Qi, 2018; Yu & Manthiram, 2018)

In this study, we investigate the effects of fluorine substitution at oxygen sites in $LiCoO_2$ (hereinafter call LCO) systems using density functional theory (DFT) calculations. Our analysis encompasses variance of lattice during delithiation, electrode voltage, electronic state, and its influence on rate capability. Through these investigations, our goal is achieving a better understanding of the implications of fluorine substituted $LiCoO_{2-x}F_x$ (hereinafter call LCOF) cathode materials.

2. Methodology

In this work all of the calculations were performed by employing full- potential linear augmented plane wave (FP-LAPW) method as used in the WIEN2K code (Blaha, Schwarz, Madsen, Kvasnicka, & Luitz, 2001) by the frame-work of DFT.

Using PBE-GGA full relaxation was performed.

Also, we applied GGA plus an on-site Coulomb self-interaction correction potential (U^{SIC}) (hereinafter called GGA+U) to obtain more accurate electrical properties, for more comprehension. The U value was calculated to be equal to 5.87 eV for Co atom int the LCO structure, which it was equal to the used U value in literature, 6 eV (M. M. Kalantarian, Asgari, Capsoni, & Mustarelli, 2013; Meng & Arroyo-de Dompablo, 2009, 2012). The calculations were carried out as ferromagnetic (FM) in GGA and GGA+U methods.

For each atom, in the Wien2k code, a sphere radius around it should be considered. It is called as muffin tin radius, and denoted as RMT. The RMT values of 1.84, 1.76, 1.42 and 1.35 a.u. were used for Co, Li, O, and F atoms, respectively.

In this study, hexagonal structured with the $R\bar{3}m$ space group was considered as initial structure of $LiCoO_2$ cathode material. The primitive structure (atomic positions and structural characteristics) was taken from ref. (Akimoto, Gotoh, & Oosawa, 1998). For the structure, calculated integrals were over the Brillouin zone with k-points based on 11×11×2 Monkhorst–Pack (MP) (Monkhorst & Pack, 1976) mesh for hexagonal structure.

3. RESULTS AND DISSCUSSION

3.1. Structural properties and structural stability

In layered LCO cathode material, lithium atoms and transition metal are positioned in octahedral positions in the evaluated hexagonal structures. There are three unit formulas in each cell. The three parallel planes M, O, and Li make up the material structure, and each atom is arranged into a hexagonal shape. Lithium diffusion is aided by this formation. All of the planes are parallel to the c-axis, since the c-axis is crucial for our considerations. Accordingly, in order to substitute the fluoride with oxygen sites there would be three symmetric sites denoted as A, B, and C. We calculated the substitution of each site and find the energies and

forces. The most stable with low amount of forces and energies was found in site of C. Figure 1 illustrates the structure of $LiCoO_{2-x}F_x(x=\frac{2}{3})$ and the mentioned atomic sites for fluorine. It is equal to 12.6 %wt of F-doping and about 16.6 of atomic percentage.

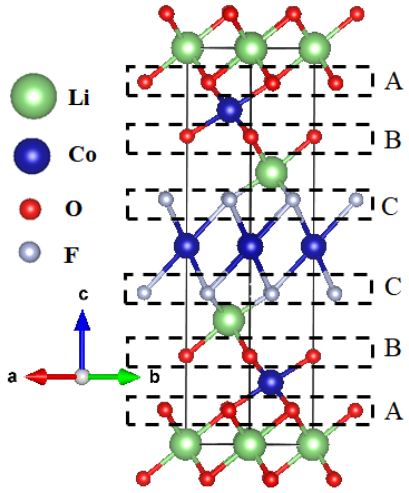

Figure 1. Schematics of intercalated (unite cell) structures of the assessed $LiCoO_{2-x}F_x$ cathode materials with demonstrated symmetric substitution sites A, B, and C.

The calculated structures in their lithiated and delithiated states, as well as the changes in the parameters following Li extraction, are shown in Table 1. By noticing the volume cells, it can be concluded that doping caused about 4% volume increase which is mostly effected by the increasing of c axis. As expected, axis c can tolerate the most shrinkage. A stable structure for this cathode material during charge/discharge is predicted by considering the maximum shrinkage of the cell volume after delithiation (structure remains stable in less than 10% change (M. M. Kalantarian, Asgari, & Mustarelli, 2013)). According to Table 1, in terms of volume shrinkage and subsequently the structural stability, fluorine doping not only does not harm the structure but also make structure a little more stable.

TABLE 1. Calculated structural data for delithiated (Delith.) and lithiated (Lith.) $LiCoO_2$ and $LiCoO_{2-x}F_x$ (per Angstrom), structural changes are in percent. In the table x is related column value and Δx/x is equal to (x delithiation – x lithiation)/ x lithiation.

Material		a	c	Vol.
$LiCoO_2$	Lith.	2.85	14.16	99.89
	Delith..	2.84	13.67	95.58
	Δx/x(%)	-0.35	-3.46	-4.31
$LiCoO_{2-x}F_x$	Lith.	2.81	15.22	104.04
	Delith.	2.85	14.15	99.83
	Δx/x(%)	1.6	-7.0	-4.0

3.2. Cell voltages

The calculated voltages obtained from two distinct approaches, namely internal and Fermi (Haghipour, Momeni, Yousefi Mashhour, & Kalantarian, 2022) energy, and produced by the GGA and GG+U methods are shown in Table 2. The main idea of Fermi energy approach is to replace Fermi energy changes with internal energy changes. This method considers the change of Fermi level during the delithiation process. According to the results all approximations and approaches predict that $LiCoO_2$ has the higher voltage and $LiCoO_{2-x}F_x$ has the lower voltage. However, in such a range of cell voltages, the lower value is more desirable regarding electrolyte voltage tolerance.

TABLE 2. Obtained reaction voltages (V) calculated in GGA/+U methods of the evaluated materials, resulted from Fermi and Internal energy approaches.

Material	Voltage (V)			
	Internal		Fermi	
	GGA	GGA+U	GGA	GGA+U
$LiCoO_2$	3.36	3.78	3.53	3.43
$LiCoO_{2-x}F_x$	3.44	3.66	3.17	3.13

3.3. Electrical properties

By studying calculated DOS diagrams, here, we evaluate the Electrical properties, i.e. rate-capability and band-gap, of the considered materials. We used two main methods for each property to assess the band-gap (BG) and the electrical rate-capability of each material. We report the BG by using the density of states (DOS) diagrams to show the intrinsic (ILBG) and extrinsic (ELBG) bands. The electrical rate-capability was examined using two approaches called as Delta (M. M. Kalantarian, Mashhour, & Barjini, 2020) and CCTB (charge carrier transfer in DOS bands) (Yousefi-Mashhour & Kalantarian, 2021).

Intrinsic and extrinsic band gap

By noticing the resulted *3d* bands as donor and acceptor, we have established that there should be two kinds of BG, i.e. intrinsic- and extrinsic-like BG (ELBG and ILBG, respectively) (M. Kalantarian & Yousefi Mashhour, 2019; M. M. Kalantarian, Mashhour, et al., 2020; Momeni et al., 2019). The BG depends on the spin of each electron, which is a natural property of the electron. Therefore, we have to look at the spin-up and -down of a material separately when we evaluate the BG. The lower energy is more desirable, so the lower BG is the dominant value (M. M. Kalantarian, Mashhour, et al., 2020). For each pair of structures of a material, one with intercalation and one without, the higher BG value determines the electron transfer (M. M. Kalantarian, Mashhour, et al., 2020). So, we first compare the spin-down values of the delithiated and lithiated structures,

and we report the higher one as the spin-down BG of the pair.

In Figure 2, ILBG values of the considered materials are shown in DOS diagram calculated with GGA. Also, resulted ILBGs are given in Table 3. Accordingly, both approximations predicted that LCOF has better conductivity (lower ILBG) than LCO.

Evaluation of ELBG is usually more significant than ILBG, at least for electrode materials (Hatef Yousefi-Mashhour, 2023).

As far as the extrinsic BG (ELBG) was considered as the electrical conductivity criterion, according to Table 4, both approximations show that LCOF has the superiority over LCO and its electrical conductivity is much better. This indicates that the F-doping of LCO has significant modification on electrical conductivity.

TABLE 3. Calculated ILBG for the evaluated LCO and LCOF materials by GGA/+U approaches. The controlling BG (Ctr.) are shown in the right column.

Method	Electrode	spin-up		spin-down		Ctr.
		int.	deint.	int.	deint.	
GGA	$LiCoO_2$	8.7	11.6	8.7	9.9	9.9
	$LiCoO_{2-x}F_x$	8.3	5.1	8	7.9	8
GGA+U	$LiCoO_2$	6.9	0	8.2	9.5	6.9
	$LiCoO_{2-x}F_x$	4.1	7.3	4.2	6.5	6.5

TABLE 4. Calculated ELBG for the evaluated materials by GGA/+U approaches. The controlling BGs (Ctr.) are shown in the right column.

Method	Material	spin-up		spin-down		Ctr.
		int.	deint.	int.	deint.	
GGA	$LiCoO_2$	1.2	1.3	1.2	0	1.2
	$LiCoO_{2-x}F_x$	1.2	1	0.4	0	0.4
GGA+U	$LiCoO_2$	6.9	0	2.4	1.7	2.4
	$LiCoO_{2-x}F_x$	4.1	7.3	0	0.2	0.2

Electrical rate-capability

We used two main approaches to assess each material's electrical rate-capability , which are Delta (M. M. Kalantarian, Mashhour, et al., 2020; Momeni et al., 2019) and CCTB (Yousefi-Mashhour & Kalantarian, 2021; Yousefi-Mashhour, Namiranian, & Kalantarian, 2023). The Delta method compares the difference between the intrinsic conduction/valence bands of the structures with and without intercalation, which are called ΔCB/ΔVB (M. M. Kalantarian, Mashhour, et al., 2020; Momeni et al., 2019). This difference indicates the rate-capability criterion. We have to consider the spin-up and spin-down separately and choose the lowest value among the Delta results as the dominant one. The other method, called CCTB, which is based on how the charge carriers transfer in the density of states (DOS) bands (Yousefi-Mashhour & Kalantarian, 2021; Yousefi-Mashhour et al., 2023). In the both methods, we have to align the Fermi level in the structures with and without intercalation, which shows the behavior of the semiconductor junction.

Delta approach

Figure 2 illustrates DOS diagram in view of the Delta approach for GGA method for the considered cathodes. The resulted Delta values for both calculation methods as well as the governing values are shown in Table 5. According to the table and making comparison by its resulted values between these two electrode materials, our calculations show that, as far as intrinsic rate-capability criterion is considered, both materials are in the same range and show suitable rate capability.

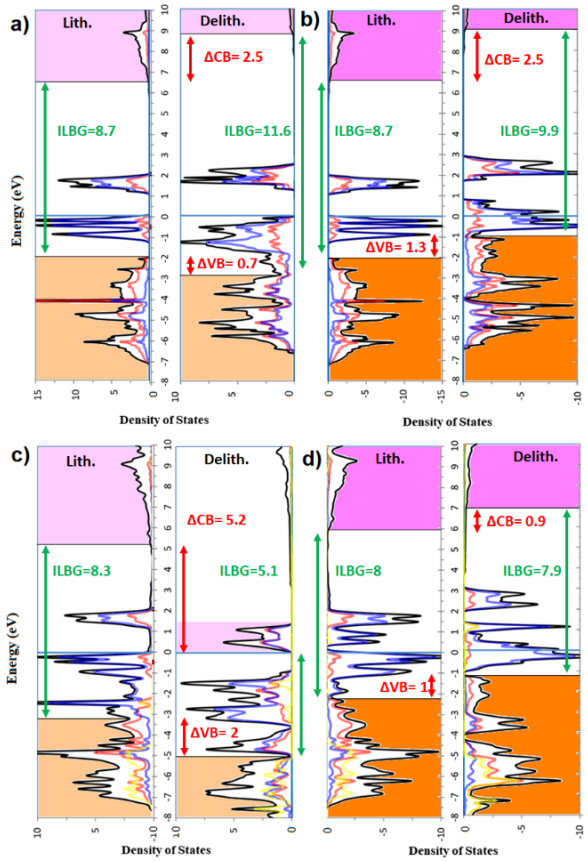

Figure 2. DOS diagrams calculated for intercalated and deintercalated structures via GGA, spin-up, spin-down of a-b) $LiCoO_2$, c-d) $LiCoO_{2-x}F_x$. The intrinsic bands are colored. ILBG, and ΔCB/VB values are shown in the diagrams. The pink and orange colored bands are intrinsic conduction and valance bands, respectively. The lower value among delta values becomes the governing value of the electrode. The Fermi levels set to zero and are aligned for each reacted-unreacted joint structure. The light and dark colors are for spin –up and –down, respectively.

TABLE 5. Calculated values of the Delta criterion via GGA, per eV. The governing (Gvr.) value is the lowest amount in each row.

Method	Material	ΔCB		ΔVB		Gvr.
		up	dn	up	dn	
GGA	**$LiCoO_2$**	2.2	2.5	0.7	1.3	0.7
	$LiCoO_{2-x}F_x$	5.2	0.9	2	1	0.9

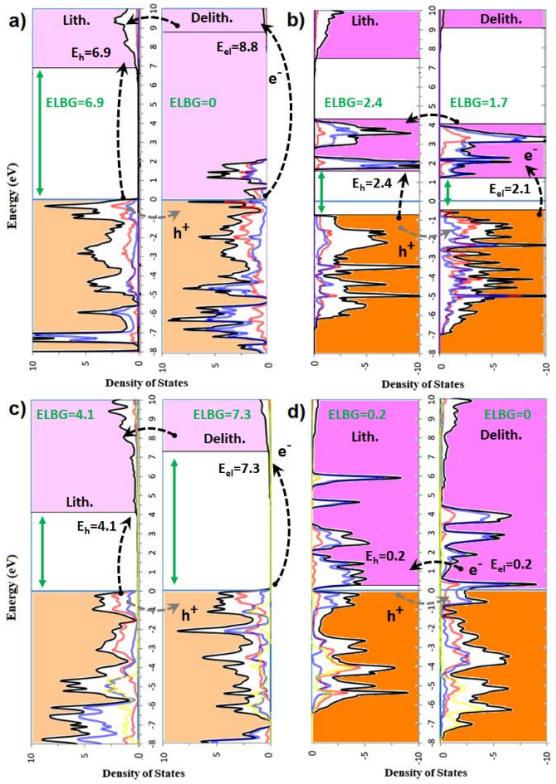

Figure 3. Calculated DOS diagrams via GGA+U for the deintercalated and intercalated structures spin –up and spin-down of a-b) $LiCoO_2$, c-d) $LiCoO_{2-x}F_x$. Path of the electron-hole and electron transfer is shown by black and gray arrow, respectively. The generated bands by *3d*-Co orbitals are assumed as acceptor/donor bands. The pink and orange colored bands are intrinsic conduction and valance bands, respectively. The lower value among delta values becomes the governing value of structure. The Fermi levels set to zero and are aligned for each reacted-unreacted joint structure. CCTB values are denoted as E_{el} and E_h for electron and electron-hole energy, respectively. The light and dark colors are for spin –up and –down, respectively.

Charge carrier transfer in DOS bands (CCTB)

Details of the CCTB approach were explained in Ref. (Yousefi-Mashhour & Kalantarian, 2021). However, here, we explain one case study to recall the concept. Figure 3 displays the DOS diagrams of the studied cathodes computed by the GGA+U method with spin polarization up and down.

Unlike the Delta approach (M. M. Kalantarian, Hafizi Barjini, & Momeni, 2020; M. M. Kalantarian, Mashhour, et al., 2020; Momeni et al., 2019), we use the extrinsic-like bands (ELBs) for CCTB. Therefore, obviously, GGA+U should be more trustworthy. The transfer paths for the electron and electron-hole are indicated in Figure 3 by the black and gray dash-line arrows, respectively.

We can explain the CCTB idea with an example. Figure 3c shows the junction between the structures with and without intercalation (reacted and unreacted) for the spin-up LCOF cathode material, which we calculated using GGA+U. An electron from the valence band of the unreacted structure, COF, can cross the junction and conduct only if the two structures have overlapping electron states in DOS. The electron needs an energy of 7.3 eV to overcome the barrier. However, if we look at Figure 3b, we can see that both structures have overlapped *3d* bands that can help the electron to conduct easily. Therefore, the electron only needs 2.2 eV to overcome the gap barrier and participate in conduction.

As for the electron-hole transfer, we can see from Figure 3b that when an electron has an energy of 2.4 eV. It goes to the conduction band of the intercalated structure and leaves an electron-hole in the valence band. The electron-hole can then move to the valence band of the unreacted structure because these two bands have an overlap. For having a better explanation and information please see Ref. (Yousefi Mashhour & Kalantarian, 2021).

The method gives four values to each electrode, where two of them show how an electron (spin-up and -down) and the other two show how an electron-hole (spin-up and -down) can transfer through junctions. The lowest number is the governing one in this method, because a lower barrier is better. The governing numbers are used to compare the electrodes and see how good they are for the rate-capability. Table 6 shows all and dominant numbers of CCTB method for the electrodes that we studied from the DOS diagrams (Figure 3). In the table, E_h is the energy that is required to transfer an electron-hole, and E_{el} is the energy that is required to transfer an electron from an unreacted to a reacted structure. The lowest energy among the E_{el}/E_h spin-up/down is the criterion value.

According to Table 6, CCTB approach predicted that LCOF has the superiority over LCO and it has much higher rate-capability. Generally, as far as considering the CCTB approach, it can be concluded that 12.6% dopant of fluorine can remarkably improve the electrical rate capability of LCO cathode material.

TABLE 6. The calculated required energy values for transferring holes (E_h) and electrons (E_{el}) crossways deintercalated-intercalated junction, gained from DOS diagrams (Figure 3) by different methods for the considered case studies. The values are in eV unit. The lowest value in each row is the criterion value (C.V) (underlined). Also, the major charge carriers (MCC) are shown in the right column.

Method	Material	Spin-up		Spin-down		C.V/MCC
		E_{el}	E_h	E_{el}	E_h	
GGA+U	**$LiCoO_2$**	8.8	6.9	<u>2.1</u>	2.4	2.1 / el
	$LiCoO_{2-x}F_x$	7.3	4.1	<u>0.2</u>	<u>0.2</u>	0.2 / el-h

4. CONCLUSION

In this work, we studied the structural, electrical, and electrochemical properties of $LiCoO_2$ and $LiCoO_{2-x}F_x$ cathode materials for LIBs using DFT. We found that fluorine-doping can improve the performance and stability of $LiCoO_2$ in several aspects.

It was revealed that fluorine-doping can improve the structural stability of $LiCoO_2$ by reducing the volume shrinkage after delithiation. We also found that the most stable fluorine substitution site was C, which is the farthest from the lithium layer.

It was shown that fluorine doping can decrease the cell voltage of $LiCoO_2$ by lowering the Fermi level and the internal energy. We calculated the cell voltages using two different approaches, namely internal and Fermi energy, and two different methods, namely GGA and GGA+U. We obtained consistent results that $LiCoO_{2-x}F_x$ had a lower voltage than $LiCoO_2$. This makes it more desirable regarding electrolyte tolerance to have a better lifetime of cell.

Evaluations showed that fluorine doping can improve the electrical properties of $LiCoO_2$ by reducing the band gap and the charge carrier transfer barrier (CCTB). We assessed the band gap and the electrical rate-capability using two main methods, namely intrinsic and extrinsic band gap, and Delta and CCTB approaches. We showed that $LiCoO_{2-x}F_x$ has a lower band gap and a lower CCTB than $LiCoO_2$, which indicates a better electrical conductivity and rate-capability.

In conclusion, we demonstrated that fluorine doping can be an effective strategy to modify and optimize the stability and performance of $LiCoO_2$ cathode materials for LIBs. We also provided a comprehensive analysis of the electrochemical, electrical, and structural properties of $LiCoO_2$ and $LiCoO_{2-x}F_x$, using DFT. We hope that our study can provide useful insights and guidance for the development and design of novel cathode materials for LIBs.

5. ACKNOWLEDGEMENTS

The Wien2k code access is gratefully acknowledged. Materials and Energy Research Center's (MERC, Iran) financial support is gratefully acknowledged through an international project supported by internal grant (project nos. of 391400007, 391400006, and 391400005).

REFERENCES

1. Akimoto, J., Gotoh, Y., & Oosawa, Y. (1998). Synthesis and Structure Refinement of LiCoO 2 Single Crystals. *Journal of Solid State Chemistry*, *141*(1), 298-302,. https://doi.org/10.1006/jssc.1998.7966
2. Amatucci, G., Tarascon, J., & Klein, L. (1996). CoO2, the end member of the Li x CoO2 solid solution. *Journal of The Electrochemical Society*, *143*(3), 1114, https://doi.org/10.1149/1.1836594.
3. Amatucci, G. G., & Pereira, N. (2007). Fluoride based electrode materials for advanced energy storage devices. *Journal of Fluorine Chemistry*, *128*(4), 243-262, https://doi.org/10.1016/j.jfluchem.2006.11.016
4. Assat, G., & Tarascon, J.-M. (2018) .Fundamental understanding and practical challenges of anionic redox activity in Li-ion batteries. *Nature Energy*, *3*(5), 373-386, https://doi.org/10.1038/s41560-018-0097-0
5. Barkholtz, H. M., Preger, Y., Ivanov, S., Langendorf, J., Torres-Castro, L., Lamb, J., . . . Ferreira, S. R. (2019). Multi-scale thermal stability study of commercial lithium-ion batteries as a function of cathode chemistry and state-of-charge. *Journal of Power Sources*, *435*, 226777, https://doi.org/10.1016/j.jpowsour.2019.226777
6. Blaha, P., Schwarz, K., Madsen, G., Kvasnicka, D., & Luitz, J. (2001). *WIEN2k, An augmented plane wave plus local orbitals program for calculating crystal properties*. Austria: Vienna University of Technology, Austria, http://www.wien2k.at/reg_user/textbooks/usersguide.pdf
7. Blomgren, G. E. (2016). The development and future of lithium ion batteries. *Journal of The Electrochemical Society*, *164*(1), A5019 ., *https://doi.org/*10.1149/2.0251701jes.
8. Cohen, A. J., Mori-Sánchez, P., & Yang, W. (2011). Challenges for density functional theory. *Chemical Reviews*, *112*(1), 289-320, https://doi.org/10.1021/cr200107z
9. Dokko, K., Nishizawa, M., Horikoshi, S., Itoh, T., Mohamedi, M., & Uchida, I. (2000). In Situ Observation of LiNiO2 Single-Particle Fracture during Li-Ion Extraction and Insertion. *Electrochemical and Solid-State Letters*, *3*(3), 125, https://doi.org/10.1149/1.1390977.
10. Ellis, B. L., Lee, K. T., & Nazar, L. F. (2010). Positive electrode materials for Li-ion and Li-batteries. *Chemistry of Materials*, *22*(3), 691-714 , *https://doi.org/10.1021/cm902696j*
11. Fergus, J. W. (2010). Recent developments in cathode materials for lithium ion batteries. *Journal of Power Sources*, *195*(4), 939-954, https://doi.org/10.1016/j.jpowsour.2009.08.089
12. Guillén-López, A., Espinosa-Torres, N. D., Cuentas-Gallegos, A. K., Robles, M., & Muñiz, J. (2018). Understanding bond formation and its impact on the capacitive properties of SiW12 polyoxometalates adsorbed on functionalized carbon nanotubes. *Carbon*, *130*, 623-635, https://doi.org/10.1016/j.carbon.2018.01.043
13. Haghipour, A., Momeni, M., Yousefi Mashhour, H., & Kalantarian, M. M. (2022). Memory effects' mechanism in the intercalation batteries: the particles' bipolarization. *ACS applied materials & interfaces*, https://doi.org/10.1021/acsami.2c00472
14. Hatef Yousefi-Mashhour, S. S., Samin Hassani, Mohammad Mahdi Kalantarian. (2023). Spin and band-gap in spin-polarized materials for first principal studies. *in press* https://doi.org/10.30501/acp.2023.425848.1139
15. Jones, C. D., Rossen, E., & Dahn, J. (1994). Structure and electrochemistry of Li [sub x] Cr [sub y] Co [sub 1-y] O [sub 2]. *Solid State Ionics;(Netherlands)*, *68*, *https://www.osti.gov/etdeweb/biblio/5047615*
16. Kalantarian, M., & Yousefi Mashhour, H. (2019). Evaluating electrical properties, band gaps and rate capability of Li2MSiO4 (M= Mn, Fe, Co, Ni) cathode materials using DOS diagrams. *Advanced Ceramics Progress*, *5*(3), 30-35, https://doi.org/10.30501/acp.2019.95358
17. Kalantarian, M. M., Asgari, S., Capsoni, D., & Mustarelli, P. (2013). An ab initio investigation of Li 2 M 0.5 N 0.5 SiO 4 (M, N= Mn, Fe, Co Ni) as Li-ion battery cathode materials. *Physical Chemistry Chemical Physics*, *15*, 8035-8041, https://doi.org/10.1039/C3CP51481A
18. Kalantarian, M. M., Asgari, S., & Mustarelli, P. (2013). Theoretical investigation of Li2MnSiO4 as a cathode material for Li-ion batteries: a DFT study. *Journal of Materials Chemistry A*, *1*(8), 2847-2855, *https://doi.org/10.1039/C2TA01363K*

19. Kalantarian, M. M., Hafizi Barjini, M., & Momeni, M. (2020). Ab Initio Study of AMBO3 (A = Li, Na and M = Mn, Fe, Co, Ni) as Cathode Materials for Li-Ion and Na-Ion Batteries. *ACS Omega*, *5*(15), 8952-8961, https://doi.org/10.1021/acsomega.0c00718

20. Kalantarian, M. M., Mashhour, H. Y., & Barjini, M. H. (2020). A semi-quantitative approach to evaluate electrical rate-capability and conductivity of polyanion cathode materials of intercalation batteries using DOS diagrams. *Ceramics International*, *46*(10), 15222-15227, https://doi.org/10.1016/j.ceramint.2020.03.060

21. Kim, T., Song, W., Son, D.-Y., Ono, L. K., & Qi, Y. (2019). Lithium-ion batteries: outlook on present, future, and hybridized technologies. *Journal of Materials Chemistry A*, *7*(7), 2942-296 . , https://doi.org/10.1039/C8TA10513H

22. Kobayashi, H., Shigemura, H., Tabuchi, M., Sakaebe, H., Ado, K., Kageyama, H., Morimoto, S. (2000). Electrochemical Properties of Hydrothermally Obtained LiCo1− x Fe x O 2 as a Positive Electrode Material for Rechargeable Lithium Batteries . *Journal of The Electrochemical Society*, *147*(3), 960, https://doi.org/10.1149/1.1393298

23. Kubo, K., Fujiwara, M., Yamada, S., Arai, S., & Kanda, M. (1997). Synthesis and electrochemical properties for LiNiO2 substituted by other elements. *Journal of Power Sources*, *68*(2), 553-557, https://doi.org/10.1016/S0378-7753(97)02530-5.

24. Lee, S .H., Moon, J.-S., Lee, M.-S., Yu, T.-H., Kim, H., & Park, B. M. (2015). Enhancing phase stability and kinetics of lithium-rich layered oxide for an ultra-high performing cathode in Li-ion batteries. *Journal of Power Sources*, *281*, 77-84, https://doi.org/10.1016/j.jpowsour.2015.01.158.

25. Meng, Y. S., & Arroyo-de Dompablo, M. E. (2009). First principles computational materials design for energy storage materials in lithium ion batteries. *Energy & Environmental Science*, *2*(6), 589-609, https://doi.org/10.1039/B901825E

26. Meng, Y. S., & Arroyo-de Dompablo, M. E. (2012). Recent Advances in First Principles Computational Research of Cathode Materials for Lithium-Ion Batteries. *Accounts of Chemical Research*. , https://doi.org/10.1021/ar2002396

27. Mizushima, K., Jones, P., Wiseman, P., & Goodenough, J. B. (1980). LixCoO2 (0< x<-1): A new cathode material for batteries of high energy density. *Materials Research Bulletin*, *15*(6), 783-789. https://doi.org/10.1016/0025-5408(80)90012-4

28. Momeni, M., Mashhour, H. Y., & Kalantarian, M. M. (2019). New approaches to consider electrical properties, band gaps and rate capability of same-structured cathode materials using density of states diagrams: Layered oxides as a case study. *Journal of Alloys and Compounds*, *787*, 738-743, https://doi.org/10.1016/j.jallcom.2019.02.155.

29. Monkhorst, H. J., & Pack, J. D. (1976). Special points for Brillouin-zone integrations. *Physical Review B*, *13*(12), 5188-5192. , https://doi.org/10.1103/PhysRevB.13.5188.

30. Nagaura, T. (1990). Lithium ion rechargeable battery. *Progress in Batteries & Solar Cells*, *9*, 209 ., https://doi.org/10.1541/ieejfms1990.115.4_349.

31. Naghash, A., & Lee, J. Y. (2001). Lithium nickel oxyfluoride (Li1− zNi1+ zFyO2− y) and lithium magnesium nickel oxide (Li1− z (MgxNi1− x) 1+ z O2) cathodes for lithium rechargeable batteries: Part I. Synthesis and characterization of bulk phases. *Electrochimica Acta*, *46*(7), 941-951 ., https://doi.org/10.1016/S0013-4686(00)00657-5

32. Needham, S., Wang, G., Liu, H.-K., Drozd, V., & Liu, R. (2007). Synthesis and electrochemical performance of doped LiCoO2 materials. *Journal of Power Sources*, *174*(2) ,828-831 ., https://doi.org/10.1016/j.jpowsour.2007.06.228.

33. Perdew, J. P., Yang, W., Burke, K., Yang, Z., Gross, E. K., Scheffler, M., . . . Ruzsinszky, A. (2017). Understanding band gaps of solids in generalized Kohn–Sham theory. *Proceedings of the National Academy of Sciences*, *114*(11), 2801-2806 ., https://doi.org/10.1073/pnas.1621352114.

34. Reimers, J. N., & Dahn, J. (1992). Electrochemical and in situ X-ray diffraction studies of lithium intercalation in Li x CoO2. *Journal of The Electrochemical Society*, *139*(8), 2091 ., https://doi.org/10.1149/1.2221184.

35. Thackeray, M. (1995). Structural considerations of layered and spinel lithiated oxides for lithium ion batteries. *Journal of The Electrochemical Society*, *142*(8), 2558 ., https://doi.org/10.1149/1.2050053.

36. Thirunakaran, R., Kim, T., & Yoon, W.-s. (2014). Synthesis and electrochemical characterization on dual-doped LiCoO 2 via green chemistry method for lithium rechargeable batteries. *Journal of Applied Electrochemistry*, *44*, 709-718 ., https://doi.org/10.1007/s10800-014-0687-x.

37. Ullah, A., Majid, A., & Rani, N. (2018). A review on first principles based studies for improvement of cathode material of lithium ion batteries. *Journal of energy chemistry*, *27*(1), 219-237, https://doi.org/10.1016/j.jechem.2017.09.007.

38. Wang, A., Kadam, S., Li, H., Shi, S., & Qi, Y. (2018). Review on modeling of the anode solid electrolyte interphase (SEI) for lithium-ion batteries. *npj Computational Materials*, *4*(1), 1-26 ., https://doi.org/10.1038/s41524-018-0064-0.

39. Wang, H., Jang, Y. I., Huang, B., Sadoway, D. R., & Chiang, Y. M. (1999). TEM study of electrochemical cycling-induced damage and disorder in LiCoO2 cathodes for rechargeable lithium batteries. *Journal of The Electrochemical Society*, *146*(2), 473 ., https://doi.org/10.1149/1.1391631

40. Yousefi-Mashhour, H., & Kalantarian, M. M. (2021). A theoretical approach to evaluate and understand the electrical properties of the electrode materials of batteries. *Physical Chemistry Chemical Physics*, *23*(30), 16013-16022 ., https://doi.org/10.1039/D1CP01796A.

41. Yousefi-Mashhour, H., Namiranian, A., & Kalantarian, M. M. (2023). A first principle study of structural and electrical properties of novel Li2FeO3/Li2FeO2F Li-ion battery cathode material. *ФІЗИКА НИЗЬКИХ ТЕМПЕРАТУР, 49*(1), 42-49 ., https://doi.org/10.1063/10.0016474

42. Yousefi Mashhour, H., & Kalantarian, M. M. (2021). A theoretical approach to evaluate and understand the electrical properties of the electrode materials of batteries. *Physical Chemistry Chemical Physics*, *23*, 16013-16022 ., https://doi.org/10.1039/D1CP01796A

43. Yu, X., & Manthiram, A. (2018). Electrode–electrolyte interfaces in lithium-based batteries. *Energy & Environmental Science*, *11*(3), 527-543 ., https://doi.org/10.1039/C7EE02555F

44. Zhu ,X., Shang, K., Jiang, X., Ai, X., Yang, H., & Cao, Y. (2014). Enhanced electrochemical performance of Mg-doped LiCoO2 synthesized by a polymer-pyrolysis method. *Ceramics International*, *40*(7), 11245-11249 ., https://doi.org/10.1016/j.ceramint.2014.03.170

Advanced Ceramics Progress: Vol. 9, No. 4, (Autumn 2023) 22-31

Materials and Energy Research Center
MERC

Contents lists available at ACERP

Advanced Ceramics Progress

Journal Homepage: www.acerp.ir

Original Research Article

Experimental Investigation of the Effect of Reduced Graphene Oxide Addition on the Mechanical Properties and Behavior of Ti/RGO Composites in Spark Plasma Sintering Process with Reference to Potential Applications in Medical Implants

Syyed Mohammadreza Sedehi [a], Mohammadreza Maraki [b*], Seyed Davoud Houshyar Eftekhari [c], Mohammadreza Fazeli [a], Zahra Maleki [d], Fatemeh Norouzi Palangani [d]

[a] *Ph.D. Candidate, School of Mechanical Engineering, College of Engineering, University of Tehran, Tehran, Iran.*
[b] *Master, Department of Material Engineering, Birjand University of Technology, Birjand, Iran.*
[c] *Master, Department of Engineering, Islamic Azad University, Gonabad, Iran.*
[d] *Bachelor, Department of Engineering, Gonabad University, Gonabad, Iran.*

* Corresponding Author Email: Maraki@birjandut.ac.ir (Mohammadreza Maraki) URL: https://www.acerp.ir/article_206327.html

ARTICLE INFO

Article History:

Received: 15 July 2024
Revised: 31 July 2024
Accepted: 07 September 2024

Keywords:

Titanium,
Reduced Graphene Oxide,
Spark Plasma Sintering,
Mechanical Properties,
Medical Implants

ABSTRACT

Given the strategic importance of pure titanium in sensitive industries, such as healthcare, and the existing weaknesses in the mechanical and physical properties of this metal, the present study aims to investigate the enhancement of its mechanical properties through the composite fabrication of pure titanium with Reduced Graphene Oxide (RGO) nanoparticles based on Spark Plasma Sintering (SPS) method. During the fabrication process, the mechanical properties of the samples were evaluated and compared using specialized tests. Composite fabrication is one of the effective and common methods for improving the material properties. As demonstrated in the results obtained in this study, the SPS method can be proposed as a reliable method for producing high-quality composites. Further evaluation of the mechanical properties of the samples reinforced with RGO indicates that the optimal presence of this reinforcement significantly enhances the mechanical properties compared to those of the pure samples. Moreover, the analysis of the behavior of the produced samples during the sintering process indicates a significant increase in the force and pressure in samples containing reduced graphene oxide, with no observed significant changes in displacement and temperature.

https://doi.org/10.30501/acp.2024.468057.1156

1. INTRODUCTION

As cases of tooth loss due to accidents continue to increase and population aging becomes a global issue, the demand for dental implant surgery is rising annually worldwide (Barootchi, S et al., 2020). To meet the rigid biological and mechanical requirements, dental implants must possess high strength, good corrosion resistance, and excellent biocompatibility. A variety of implant materials have been designed over the past decades, ranging from precious metals (Au, Pt, etc.) to stainless steel, CoCr alloys and titanium alloys, etc. Due to their relatively high strength, low density, low elastic

Please cite this article as: Sedehi, S. M., Maraki, M., Houshyar Eftekhari, S. D., Fazeli, M., Maleki, Z., Norouzi Palangani, F. "Experimental Investigation of the Effect of Reduced Graphene Oxide Addition on the Mechanical Properties and Behavior of Ti/RGO Composites in Spark Plasma Sintering Process with Reference to Potential Applications in Medical Implants", ***Advanced Ceramics Progress***, Vol. 9, No. 4, (2023), 22-31. https://doi.org/10.30501/acp.2024.468057.1156

modulus, and high corrosion resistance, titanium and its alloy have become popular dental implant materials among all metals (Pałka, K et al., 2018). To date, Ti and Ti alloys have been widely applied in dental implants. However, most of these implants rely on commercial pure Ti (cp-Ti), whose low strength (300 MPa) has greatly restricted its reliability in load-bearing implants such as dental screw etc., despite of its excellent biocompatibility and corrosion resistance (Niu, J et al., 2021). Some specific reinforcing particles such as TiB (Zhou, Z et al., 2023), TiC (Wang, J et al., 2024), SiC (Wang, L et al., 2024), ZrO_2 (Dwivedi, S et al., 2024), Al_2O_3 (Kaykilarli, C et al., 2024), and Y_2O_3 (Barootchi, S et al., 2020)have been introduced to improve the mechanical properties of titanium-based composites using different manufacturing technologies. Graphene and its allotropes are one of these materials. This valuable material, first synthesized by Andre Geim and Konstantin Novoselov in 2004 (Novoselov, K et al., 2004), can be used as a suitable reinforcement for composite materials due to its unique properties such as electrical (Schedin, F et al., 2007) , thermal properties (Balandin, A et al., 2008) , and tensile strength of 130 GPa (Lee, C et al., 2008) . In recent years, significant achievements have been made regarding the factors affecting the mechanical properties of titanium (Cao, H et al., 2020) , copper (Dong, L et al., 2017) , aluminum (Khodabakhshi, F et al., 2017) , and magnesium (Khodabakhshi, F et al., 2017) composites. Hang et al. (Cao, H et al., 2020) employed the same method and process of rolling during heat treatment to produce graphene-reinforced titanium composites and reported that increasing the sintering temperature from 600 to 900 C^O increases the density of composites from 84 up to 98 percent. In addition, the optimal solid-phase reaction temperature under the optimum spark plasma sintering parameters was 850 C^0, and the tensile strength could reach 1206 MPa for composites with a weight percentage of 0.3 after annealing and rolling at room temperature. Dong et al. (Dong, L. L et al., 2018) fabricated titanium-based composites with 0.6 wt% RGO using the spark plasma sintering method at temperatures ranging from 800 to 1100 C^O and studied the effects of sintering temperature on the microstructural changes and mechanical properties of the composites. They showed that the density of composites was improved upon increasing the sintering temperature. The optimal sintering temperature with a 5-minute duration under a pressure of 45 MPa was 1000 C^O, which created a good connection between the RGO reinforcement and the titanium matrix. Currently, skeletal bone diseases and related injuries have become more prevalent worldwide. Assessments have shown that over 50% of women and 20% of men over the age of 50 experience bone fractures during their remaining lifetime. Such bone defects may require surgery for complete knee and hip replacements or temporary and permanent implantation of components. This had led many researchers to pursue the development of a biological material that could mimic real bone properties such as flexibility and strength for repetitive use. Weihong Jin et al. (Jin, W et al., 2017)observed that medical materials cannot withstand loads in biological processes. Viktor Baltrus et al. referred to the significant role of these biological materials in the biological replacement of reconstructed alveolar bone insofar as some metals are now widely recognized as substitutes for natural bones. Over time, metallic materials lose their properties and fail to withstand pressure loads, thus making them susceptible to fractures. Additionally, metallic structures tend to weaken over time, leading to unintended effects such as toxicity and undesirable reactions. In the past two decades, implants for biomedical applications have undergone rapid and remarkable advancements. Titanium, due to the formation of a stable inert layer of titanium oxide on its surface, has superior biocompatibility compared to other metallic materials. With its low elastic modulus, lightweight, and reduced artifact production in computer tomography and magnetic resonance imaging compared to other metals, it has gained more popularity in the orthopedic field. Although Ti-6Al-4V is the most widely used titanium alloy for surgeries, despite its excellent performance and corrosion resistance, a high concentration of metal ions has been identified in the tissues surrounding the implants, questioning the long-term safety of the biological applications of this alloy. An alternative approach to overcoming the problem of harmful ion release is the application of pure titanium. However, the mechanical properties of commercial pure titanium are not as good as those of Ti64 alloy. In 2021, in one of the most interesting recent studies on graphene oxide-reinforced titanium-based composites, Sedehi et al. (Sedehi, S. M. R et al., 2021) successfully enhanced the mechanical properties and biocompatibility of commercial pure titanium through a combination of spark plasma sintering composite fabrication and severe plastic deformation methods. Despite the fact that relatively limited information is available on the effect of reduced graphene oxide presence on the behavior of titanium-based composites during spark plasma sintering, it has been established that the presence of this type of nanoparticles significantly contributes to the enhancement of composite properties. This research primarily aims to investigate these behaviors in titanium-based composites reinforced with different percentages of RGO during spark plasma sintering.

2. MATERIALS AND METHODS

The reduced graphene oxide was prepared from Nano part Aseman Company in Gonabad County. Spherical pure titanium powder, with the features given in Table 1, was also used as the primary material in this study. To

achieve an optimal and uniform composite structure, the following four stages were followed based on powder metallurgy principles: a) Initially, RGO nanosheets with the weight percentages of 0.05% and 0.1% were added to pure ethanol and sonicated until a dark and homogeneous solution was obtained. This physical property indicates that RGO is fully dispersed in ethanol. b) Pure titanium powder was also mixed with ethanol and vigorously stirred at room temperature. Then, both solutions were mixed for 30 min to achieve a homogeneous slurry. c) The mixed slurry was completely dried using a vacuum furnace and then ball-milled under argon gas protection for 5 h at the speed of 350 rpm with a powder-to-ball ratio of 1:10 (zirconia balls). d) The prepared powders in the previous stages were loaded into graphite molds with an inner diameter of 25 mm and a height of 50 mm and then, they were subjected to spark plasma sintering at the temperature of 900 C° and pressure of 45 MPa. The displacement rate during the sintering process is described as follws (Sugita, T et al., 1970):

$$\varepsilon = \frac{d\varepsilon}{dt} = A\,\frac{\varphi\mu b}{KT}\left(\frac{b}{G}\right)^{p}\left(\frac{\sigma}{\mu}\right)^{n} \tag{1}$$

where ε is the displacement rate, t the time (sec), A the constant coefficient, φ the diffusion coefficient, μ the shear modulus, b the Burgers vector, K the Boltzmann constant (1.38×10^{-23} j/K), T the sintering temperature (Kelvin), G the grain size (nm), σ the microscopic stress (MPa), P the grain growth rate, and n the effective stress. Generally, material displacement during spark plasma sintering process is directly proportional to the sintering time at high temperatures. In this regard, the kinetic equation of the process can be written as (Ting, C et al., 1999) :

$$\frac{1}{D}\frac{dD}{dt} = \frac{B\varphi\mu_{eff}b}{KT}\left(\frac{b}{G}\right)^{p}\left(\frac{\sigma_{eff}}{\mu_{eff}}\right)^{n} \tag{2}$$

where D denotes the relative density percentage, B a constant coefficient, σ the instantaneous compressive stress (MPa), and μeff the instantaneous shear stress (MPa). As described by Ashbi (Chaim, R et al., 2010) , the applied pressure is determined based on Formula 3:

$$\sigma_{eff} = \frac{1-D}{(D-D_0)D^2}\,\sigma_{mac} \tag{3}$$

where σ mac = 45 MPa and D_0 represent the initial relative density (40%). The Young's modulus of the porous material can also be calculated through the following equation [23]:

$$\frac{E_{eff}}{E_{th}} = 1 - \frac{P}{P_0} \tag{4}$$

where E_{eff} represent the effective Young's modulus (GPa), E_{th} the Young's modulus of the compacted material (gigapascals), p = 1-D the actual porosity, and P_0 = 1-D_0 the initial porosity (percentage). Here, μeff can be expressed using Equation 5 (Dong, L. L et al., 2018):

$$\mu_{eff} = \frac{E_{eff}}{2(1-V_{eff})} \tag{5}$$

The kinetic equations of the spark plasma sintering process can also be expressed as follows [23]:

$$\frac{1}{\mu_{eff}}\frac{1}{D}\frac{dD}{dt} = K\,\frac{\frac{Q_d}{Rt}}{T}\left(\frac{b}{G}\right)^{p}\left(\frac{\sigma_{eff}}{\mu_{eff}}\right)^{n} \tag{6}$$

$$\mathrm{Ln}\left(\frac{1}{\mu_{eff}}\frac{1}{D}\frac{dD}{dt}\right) = n\ln\left(\frac{\sigma_{eff}}{\mu_{eff}}\right) + K_1 \tag{7}$$

where K is the constant coefficient, R the gas constant (8.314 J/(mol.K)), and Qd the activation energy for surface diffusion (joules). Therefore, the above equation can be rewritten as Y = nX + K1. Based on the results from the previous research studies [5] as well as the equations provided, the optimal sintering temperature for titanium is chosen to be between 900 to 1000 C°. In the following, for more convenience, the experimental samples are labeled as follows: pure sintered sample, sintered sample containing 0.5% weight fraction RGO, and sintered sample containing 1.0% weight fraction RGO. The experimental procedures are illustrated in Fig.1.

TABLE 1. Specifications of RGO powder

Purity (%)	Aver. part. size (lm)	True density (g/cm³)	Volatile (%)	Ash (%)
99/28	4/81	2/23	0/67	0/05

TABLE 2. Specifications of the Ti powder used

Powder	Impurity content (mass%)					Density (g/cm³)	Particle size (μm)
Ti	O	Fe	N	C	Si	4/51	45
	0/27	0/05	0/03	0/02	0/02		

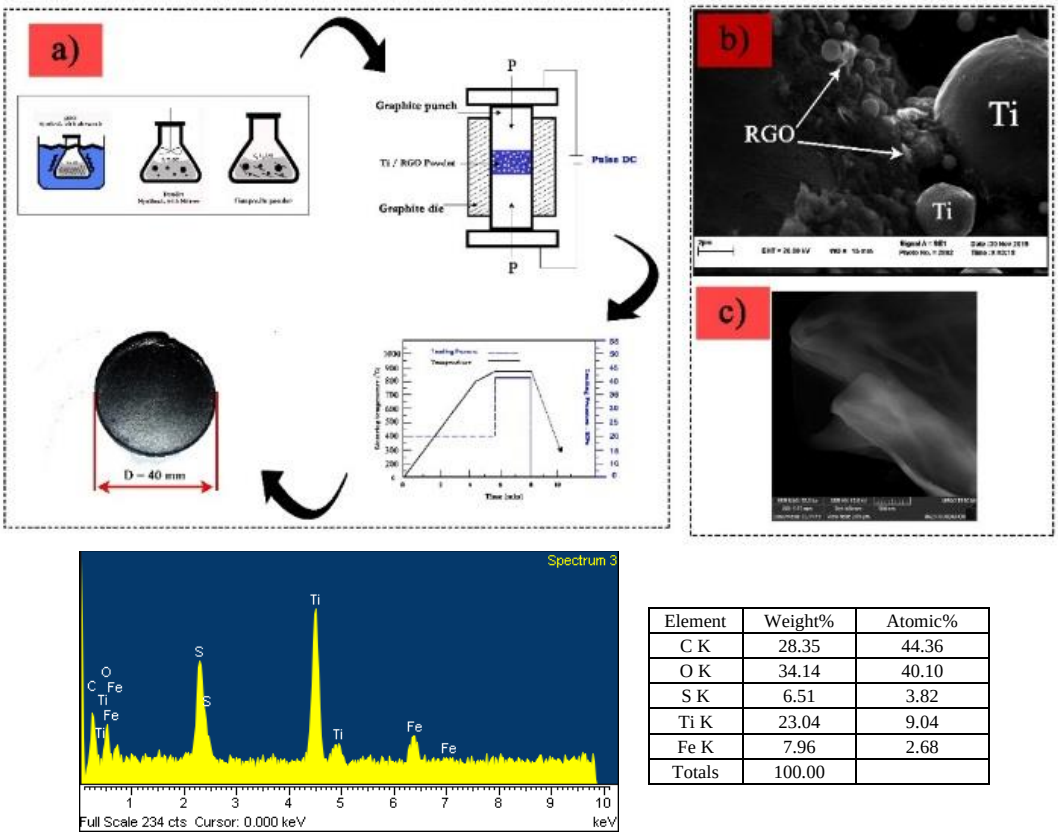

Element	Weight%	Atomic%
C K	28.35	44.36
O K	34.14	40.10
S K	6.51	3.82
Ti K	23.04	9.04
Fe K	7.96	2.68
Totals	100.00	

Figure 1. a) Schematic of the fabrication cycle, b, c) SEM images of the produced composite and RGO.

Characterization

To further investigate the existing phases and determine the presence and nature of RGO in the composite, X-Ray Diffraction (XRD) was conducted using an Explorer device manufactured by GNR Italy. In addition, to examine the morphological changes of the initial powders and produced samples, a Field Emission Scanning Electron Microscope (SEM) model MIRA3 from TESCAN, Czech Republic, with a resolution capability down to 1.5 nm at 15 kilovolts voltage, was employed. Further, the hardness of the samples was measured using a Vickers hardness tester model KOOPA-UV1 under a load of 30 kg at the dwell time of 10 sec. To obtain the average value, at least 3 repetitions of the hardness test were performed for each sample, and the Vickers microhardness value was calculated using the following equation:

$$HV = 1/8544 \frac{P}{d^2}$$

The tensile test was also conducted using an MTS810 testing machine at the speed of 1 mm/min at room temperature (ASTM E8M/E8-16a).

3. Results and discussion

Hardness

Incorporation of RGO into titanium matrix composites and application of Spark Plasma Sintering (SPS) can significantly enhance the hardness of these materials. RGO, with its two-dimensional structure and strong carbon-carbon bonds, acts as an excellent reinforcing material. When RGO is incorporated into the titanium matrix, its sheets are uniformly distributed that prevents dislocation motion and crack propagation, thereby increasing the overall hardness of the composite. The strong bonds formed between RGO and titanium particles also facilitate effective load transfer. The SPS method, due to its short processing time and relatively low temperatures, ensures uniform distribution of RGO and reduces the likelihood of defect and internal void formation. This method employs rapid electrical pulses to compress and sinter the powders at lower temperatures, compared to traditional methods, reducing the grain growth, maintaining fine grain sizes, and ultimately contributing to enhanced hardness. Such enhanced hardness of titanium composites resulting from addition of RGO and implementation of the SPS method can have a significant impact on improving the mechanical properties of the medical implants. Titanium implants are widely used in the medical field due to their excellent mechanical properties and biocompatibility, yet there is a need to improve their hardness and wear

resistance to increase their longevity and performance. Incorporating RGO into the titanium composites not only enhances the hardness but also improves the fatigue and wear resistance of the implants. Owing to these features, the RGO-reinforced titanium implants become more durable and exhibit a better performance in the body, which is particularly of high importance in orthopedic and dental applications. The results of Vickers microhardness tests on the specimens at various stages are shown in Fig.2.

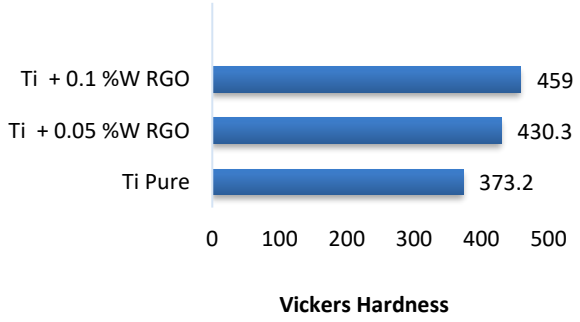

Figure 2. Hardness results

XRD

The figure below shows the X-Ray Diffraction (XRD) spectrum under the conditions of V=40 kV, Current=30 mA, and Detector type: Dectris. Evidently, titanium (Ti) and titanium carbide (TiC) phases are the main phases in the composite, whose peaks correspond to pure titanium powder serving as a reference; hence, the peak at 40 degrees is considered the strongest peak present in titanium. Additionally, weaker peaks are identified at the angles 34, 38, 53, 63, 71, 77, and 78 degrees. The Ti phase alone can only be observed in the pure titanium sample. The weak peak labeled (002) at an angle of 5.26° is attributed to the reduced graphene oxide. This peak is exclusive to components containing RGO. Changes in the intensity and position of the peaks are also observed in subsequent stages of the experiment, with the most significant peaks attributed to TiC at 43 degrees during the sintering stage. As a result of using a graphite mold and carbon infiltration, the formation of the TiC phase is observed in both pure and RGO-containing samples. The intensity of the TiC phase increases with an increase in the sintering time and temperature, which has been reported in previous studies when the sintering temperature exceeds 800 C^O [19]. The standard Gibbs free energy (ΔG) of TiC formation from the reaction between Ti and carbon can be expressed as (Sedehi, S. M. R et al., 2021) :

$\triangle G = -184571.8 + 41.382T \ -5.042TlnT + 2.425 \times 10\text{-}3T2 - 9.79 \times 105/T \ (T < 1939\ K)$

where ΔG represents the Gibbs free energy in kilojoules per mole, and T the reaction temperature in Kelvin. Given the sintering temperature of 900 C^O in this study, it can be concluded that TiC particles were formed during the spark plasma sintering process, as shown below (Sedehi, S. M. R et al., 2021) :

$\triangle G = -184571.8 + 41.382(1173.15) - 5.042(1173.15)ln(1173.15) + 2.425 \times 10\text{-}3(1173.15)2 - 9.79 \times 105/(1173.15) = -175325.641$

Therefore, all processes proved to be ideally controlled in terms of phase control, hence successful. To provide further details on carbon atom diffusion within the composite, the depth profile of carbon penetration is shown in Fig. 3. As evident in this figure, at point 6, which is close to the surface, the carbon content was approximately 19.62% by weight that decreased towards the center of the sample. In this regard, the carbon content at point 5 was found to be approximately 5.5% by weight. As mentioned earlier, the carbon content may increase as a result of the formation of the TiC phase. The formation of the TiC (titanium carbide) phase in the titanium-based composites can significantly impact the mechanical properties and performance of medical implants. TiC, known for its high hardness, wear resistance, and chemical stability, acts as a reinforcing phase within the titanium matrix. Adding TiC to titanium can enhance the hardness and wear resistance of the medical implants, thereby improving their longevity and performance, since implants are prone to severe mechanical forces and wear within the body. Additionally, the TiC phase, due to its integration with the titanium matrix, can improve the thermal properties of implants and reduce their thermal expansion, which is crucial under the varying environmental conditions within the body. Although the presence of this phase has not been specifically and fully validated for medical applications, it has gained significance through research on in vivo implants, hence considered a safe material for this field (Gonçalves, V. R. M et al., 2024) . Further, higher degrees of hardness and wear-resistance of the TiC surface decrease the amount of wear particles released from the implant surface, which in turn leads to inflammatory responses and long-term complications within the body. Consequently, the formation of the TiC phase in the titanium-based implants can significantly enhance their mechanical and biological performance, increasing their lifespan and efficacy in medical applications.

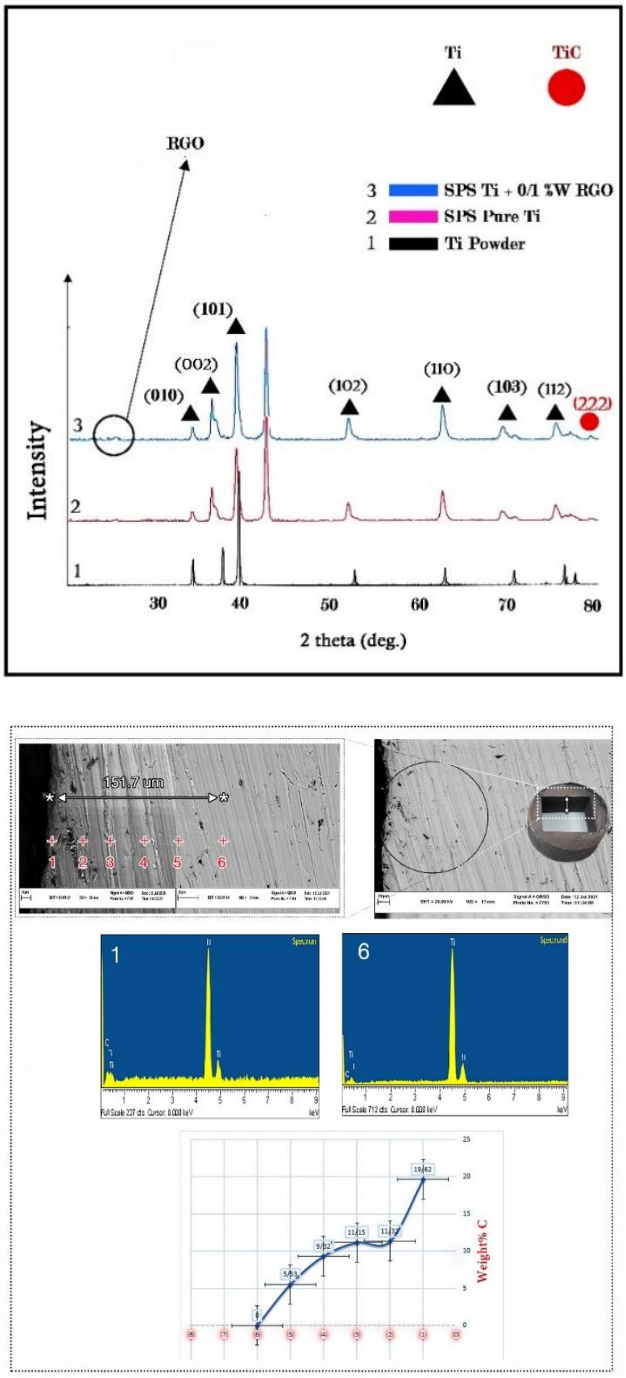

Figure 3. XRD Results and Carbon Penetration in the Composite after SPS Process

Tensile strength

Fig.4 presents the results of the tensile strength for Ti/RGO composite at different percentages of RGO, compared to the pure sample. As expected, compared to the pure sample, the samples containing graphene in the plasma sintering stage showed an optimal increase in their strength, indicating uniform distribution of the reinforcement particles. However, in the third sample with the highest amount of RGO, a suitable bond between titanium particles and RGO nanoparticles has not been established, hence a decrease in strength compared to the second sample. At this stage, the tensile strengths of the samples are recorded as 670.19, 824.71, and 821.42 MPa, respectively, and the yield strengths are calculated as 660, 800, and 780 MPa, respectively. According to the obtained results, compared to the pure sample, the tensile and yield strength values showed a significantly optimal growth upon increasing weight percentage of RGO.

Additionally, in Figure 5a-b, fractography images of the fracture surfaces of the tensile test specimens are displayed, indicating that the fracture surface of the pure sample has broader cracks than those in the sample containing RGO, hence the smaller crack widths. This factor could serve as evidence for the increased tensile strength of the reinforced samples. The fractographic analysis of the Ti/RGO composite indicates that the presence of the RGO nanoparticles significantly impacts the mechanical behavior and fracture characteristics of the material. Firstly, RGO ensures uniform stress distribution within the titanium matrix, preventing stress concentration at specific points and thereby reducing crack width. Secondly, these nanoparticles form stronger bonds between titanium particles, inhibiting rapid crack propagation. Additionally, RGO acts as a physical barrier along the crack propagation path, deflecting and slowing down crack growth, which further reduces crack width. Finally, the presence of RGO enhances energy absorption during fracture, leading to finer cracks with smaller widths. Collectively, these factors contribute to improved mechanical behavior, increased tensile strength, and enhanced fracture resistance of the Ti/RGO composite compared to the pure sample.

For instance, in knee implants requiring high resistance to mechanical pressures and tensile strength, the presence of smaller and finer cracks in RGO-containing samples can promote more uniform stress distribution within the titanium matrix, mitigating stress concentrations at specific points. This property may reduce susceptibility to failure and enhance the lifespan of knee implants. Similarly, in dental implants where seamless integration with surrounding natural tissues is crucial, the presence of fewer and finer cracks in RGO-containing samples can potentially reduce bacterial invasion risks and maintain surface integrity. Overall, these analyses demonstrate that inclusion of RGO nanoparticles can improve the mechanical behavior and fracture resistance of Ti/RGO implants compared to pure titanium samples.

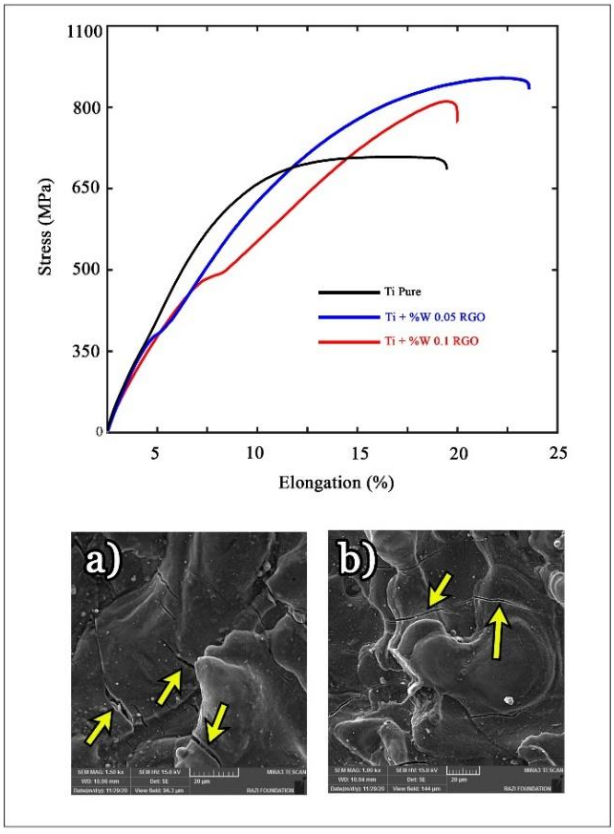

Figure 4. Tensile Test Results and Fractography Images a) Pure Sample b) Sample Containing RGO

Analysis of the Behavior of Produced Samples Based on the Output Variables of the SPS Device during the Fabrication Process

In previous research with a main focus on the implementation of spark plasma sintering for composite fabrication, little attention has been paid to the outputs of the device as well as the behavior of the produced composites during the process. Given the high importance of analyzing the behavior of RGO-reinforced composites, this study focused on the behavior of the pure and RGO-reinforced samples at different percentages of RGO during the process, yielding

interesting results. Fig.5 illustrates the displacement, force, pressure, and temperature of the three produced samples in this study: the first sample was pure titanium, and the next two samples contained RGO with different percentages. As observed in this figure, no significant changes were observed in the displacement parameter for the three produced samples. However, in terms of force and pressure, it is quite evident that while the pure titanium sample undergoes a descending trend during the process, the other two samples containing RGO possess an optimum level of force and pressure during the process. To be specific, the force imposed on the pure titanium sample reached its minimum level of 1450 N, while that on the second and third samples reached 1850 and 1780 N, respectively. Similarly, the minimum pressure before loading completion for the three samples was 29, 37, and 36 MPa, respectively, indicating the significance of analyzing the output parameters of the behavior of the produced composite with the SPS method. The temperature variable was also recorded continuously during the process using sensors embedded in the device and mold. However, no significant changes were observed in temperature for these three samples throughout the process. In summary, the output results from the device regarding the analysis of the behavior of the produced samples show that the recorded force and pressure are consistent with the results from the tensile test. It can be concluded that although the presence of RGO increases the force and pressure imposed on the mold during the process, the good connection between the matrix and reinforcement achieved after sintering has also increased the tensile strength and yield strength of the samples.

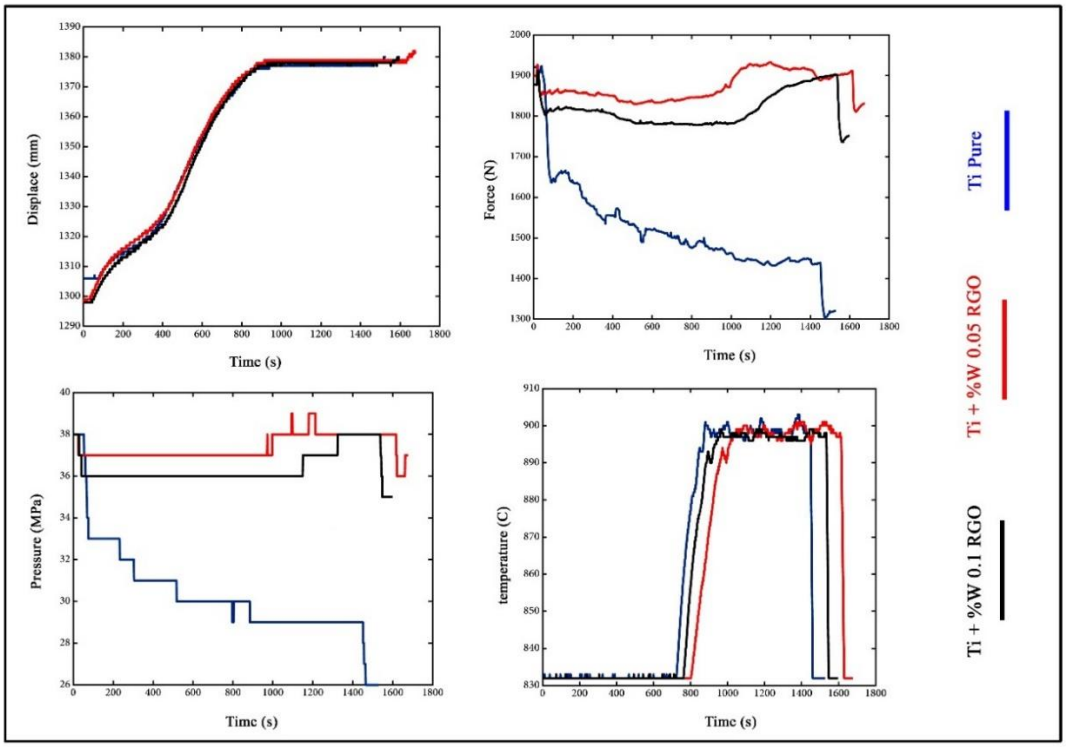

Figure 5. Behavior of different produced samples using output variables during the SPS process

Conclusions

Composite synthesis method is a common and effective method for enhancing various properties. In this study, titanium samples reinforced with reduced graphene oxide nanoparticles were fabricated using spark plasma sintering method at the temperature of 900 C°, pressure of 45 MPa, and time of 6 min. The effect of RGO presence on the mechanical properties and behavior of the samples during the sintering process was investigated, and the following conclusions were drawn

1. Based on the summary of the research results, Spark Plasma Sintering (SPS) method was proposed introduced as a reliable technique for producing high-quality composites. However, due to the sensitivity of the method to phase formation, it may adversely affect the quality of produced components, especially in certain medical applications. Additionally, unlike conventional manufacturing processes, the SPS method had some limitations in the size and complexity of parts it produced. Considering these advantages and disadvantages, application of SPS for titanium component production for medical applications required precise evaluation and thorough understanding of the properties and requirements of the intended products to achieve the optimal outcomes and efficiency.

2. The formation of the TiC (titanium carbide) phase in titanium-based composites could significantly affect the mechanical properties and performance of medical implants due to its high hardness, wear resistance, and chemical stability. Additionally, once integrated with the titanium matrix, the TiC phase enhanced the thermal properties of implants and reduced their thermal expansion, which is crucial under the variable environmental conditions within the body.
3. The results of the mechanical properties of RGO-reinforced samples indicated that although the presence of this reinforcement increases the mechanical properties compared to the pure sample, a diminishing return trend was observed among the samples with different RGO concentrations.
4. The analysis of the behavior of the produced samples during the sintering process, conducted using precise sensors installed in the device and mold, indicates that in samples containing RGO, the force and pressure increase significantly and maintain a relatively constant level, whereas in the pure sample, a noticeable descending trend is experienced.
5. Regarding the output values of the samples' behavior during the process, displacement and temperature did not show specific sensitivity to the presence of graphene, and all three samples exhibited similar behavior.

Acknowledgments

The authors would like to express their appreciation to Nano Part Aseman Company in Gonabad County for providing the raw materials, as well as Bargaz (https://bargaz.ir/) and Kohmax companies (https://koohmax.ir/) in Gonabad County for their constructive support, which has greatly benefited them.

References

1. Balandin, A. A., Ghosh, S., Bao, W., Calizo, I., Teweldebrhan, D., Miao, F., & Lau, C. N. (2008). Superior thermal conductivity of single-layer graphene. Nano letters, 8(3), 902-907. https://doi.org/10.1021/nl0731872.
2. Barootchi, S., Chan, H. L., Namazi, S. S., Wang, H. L., & Kripfgans, O. D. (2020). Ultrasonographic characterization of lingual structures pertinent to oral, periodontal, and implant surgery. Clinical oral implants research, 31(4), 352-359. https://doi.org/10.1111/clr.13573
3. Cao, H. C., & Liang, Y. L. (2020). The microstructures and mechanical properties of graphene-reinforced titanium matrix composites. Journal of Alloys and Compounds, 812, 152057. https://doi.org/ 10.1016/j.jallcom.2019.152057.
4. Chaim, R., & Bar-Hama, O. R. (2010). Densification of nanocrystalline NiO ceramics by spark plasma sintering. Materials Science and Engineering: A, 527(3), 462-468. https://doi.org/10.1016/j. msea.2009.10.011.
5. Dang, Q., Huang, G., Wang, Y., Zhang, C., Liu, G. H., & Wang, Z. D. (2024). Mechanical properties and thermal deformation behavior of low-cost titanium matrix composites prepared by a structure-optimized Y2O3 crucible. Journal of Iron and Steel Research International, 31(3), 738-751. https://link.springer.com/article/10.1007/s42243-023-01093-2.
6. Dong, L., Chen, W., Deng, N., Song, J., & Wang, J. (2017). Investigation on arc erosion behaviors and mechanism of W70Cu30 electrical contact materials adding graphene. Journal of Alloys and Compounds, 696, 923-930. https://doi.org/10.1016/j.jallcom.2016.12.044.
7. Dong, L. L., Xiao, B., Liu, Y., Li, Y. L., Fu, Y. Q., Zhao, Y. Q., & Zhang, Y. S. (2018). Sintering effect on microstructural evolution and mechanical properties of spark plasma sintered Ti matrix composites reinforced by reduced graphene oxides. Ceramics International, 44(15), 17835-17844. https://doi.org/10.1016/j.ceramint.2018.06.252.
8. Dwivedi, S. P., Saxena, K. K., Sharma, S., & Chaudhary, V. (2024). Effect of Yttria-Stabilized Zirconia addition along with Cu in development of titanium based metal matrix composite via FSP technique for the application in biomedical devices. Composite Interfaces, 1-25. https://doi.org/10.1080/09276440.2024.2330789
9. Gonçalves, V. R. M., Corrêa, D. R. N., de Sousa, T. D. S. P., Pintão, C. A. F., Grandini, C. R., Afonso, C. R. M., & Lisboa-Filho, P. N. (2024). Promising composites for wear resistant load-bearing implant applications: Low elastic moduli of β Ti–Nb alloy reinforced with TiC particles and/or TiB whiskers. Journal of Materials Research and Technology, 30, 879-889. https://www.sciencedirect.com/science/article/pii/S2238785424006641.
10. Jin, W., & Chu, P. K. "Orthopedic implants," Vol. 17, No.20, pp. 1- 15, 2017. http://www.google.com/url?sa=t&rct=j&q=&esrc=s&source=web&cd=&cad=rja&uact=8&ved=2ahUKEwj6h6jsqNuIAxVBgf0HHYMFCaYQFnoECBAQAQ&url=http%3A%2F%2Fwww.cityu.edu.hk%2Fphy%2Fappkchu%2FPublications%2F2019%2F19.04.pdf&usg=AOvVaw1O25mAKDgX-pRSAGJfX6ly&opi=89978449
11. Kaykilarli, C., Uzunsoy, D., & Yeprem, H. A. (2024). Role of process control agent in the production of Al2O3-reinforced titanium matrix composites. Ceramics International, 50(9), 16452-16462. https://www.sciencedirect.com/science/article/pii/S0272884224006266.
12. Khodabakhshi, F., Arab, S. M., Švec, P., & Gerlich, A. P. (2017). Fabrication of a new Al-Mg/graphene nanocomposite by multi-pass friction-stir processing: dispersion, microstructure, stability, and strengthening. Materials Characterization, 132, 92-107. https://doi.org/ 10.1016/j.matchar.2017.08.009.
13. Lee, C., Wei, X., Kysar, J. W., & Hone, J. (2008). Measurement of the elastic properties and intrinsic strength of monolayer graphene. Science, 321(5887), 385-388. https://doi.org/10.1126/science.1157996.
14. Niu, J., Guo, Y., Li, K., Liu, W., Dan, Z., Sun, Z., ... & Zhou, L. (2021). Improved mechanical, bio-corrosion properties and in vitro cell responses of Ti-Fe alloys as candidate dental implants. Materials Science and Engineering: C, 122, 111917. https://www.sciencedirect.com/science/article/pii/S0928493121000552.
15. Novoselov, K. S., Geim, A. K., Morozov, S. V., Jiang, D. E., Zhang, Y., Dubonos, S. V., ... & Firsov, A. A. (2004). Electric field effect in atomically thin carbon films. Science, 306(5696), 666-669. https://www.science.org/doi/abs/10.1126/science.1102896.
16. Pałka, K., & Pokrowiecki, R. (2018). Porous titanium implants: a review. Advanced Engineering Materials, 20(5), 1700648. https://doi.org/10.1002/adem.201700648
17. Schedin, F., Geim, A. K., Morozov, S. V., Hill, E. W., Blake, P., Katsnelson, M. I., & Novoselov, K. S. (2007). Detection of individual gas molecules adsorbed on graphene. Nature materials, 6(9), 652-655. https://doi.org/10.1038/nmat1967.

18. Sedehi, S. M. R., Khosravi, M., & Yaghoubinezhad, Y. (2021). Mechanical properties and microstructures of reduced graphene oxide reinforced titanium matrix composites produced by spark plasma sintering and simple shear extrusion. Ceramics International, 47(23), 33180-33190. https://www.sciencedirect.com/science/article/pii/S0272884221026195.

19. Sugita, T., & PASK, J. A. (1970). Creep of doped polycrystalline Al2O3. Journal of the American Ceramic Society, 53(11), 609-613. https://doi.org/10.1111/j.1151-2916.1970.tb15983.x.

20. Ting, C. J., & Lu, H. Y. (1999). Hot-pressing of magnesium aluminate spinel—I. Kinetics and densification mechanism. Acta materialia, 47(3), 817-830. https://doi.org/10.1016/S1359-6454(98)00400-5.

21. Wang, J., Tang, L., Xue, Y., Zhao, Z., Ye, Z., Cao, W., ... & Jiang, F. (2024). Microstructure and properties of (diamond+ TiC) reinforced Ti6Al4V titanium matrix composites manufactured by directed energy deposition. Journal of Materials Research and Technology, 28, 3110-3120. https://www.sciencedirect.com/science/article/pii/S223878542303291X.

22. Wang, L., Yuan, S., Gao, X., Li, Q., Xu, W., An, W., ... & Chen, B. (2024). Unveiling Damage Mechanisms of SiC Fiber-reinforced Titanium Matrix Composites through Ultrasonic Scratching. Journal of Cleaner Production, 142820. https://www.sciencedirect.com/science/article/pii/S0959652624022698.

23. Zhou, Z., & Liu, Y. (2023). New insights into the evolution of TiB whisker and TiC particle during selective laser melting of titanium matrix composites. Materials Science and Engineering: A, 877, 145200. https://www.sciencedirect.com/science/article/pii/S092150932300624X.

Advanced Ceramics Progress: Vol. 9, No. 4, (Autumn 2023) 32-40

Materials and Energy Research Center
MERC

Contents lists available at ACERP

Advanced Ceramics Progress

Journal Homepage: www.acerp.ir

Original Research Article

Identifying Effective Parameters for Ceramic Floor Tile Strength Using Design of Experiments Methodology

Peyman Mardani Ghahfarrokhi [a], Rasool Sahragard [b], Hossein Ghanbari [c,*], Mojtaba Safari [d]

[a] *Master, Department of Industrial Engineering, Kharazmi University of Tehran, Tehran, Iran.*
[b] *Master, Department of Industrial Engineering, University of Semnan, Semnan, Iran.*
[c] *Ph.D. Candidate, Department of Industrial Engineering, Iran University of Science and Technology, Tehran, Iran.*
[d] *Ph.D. Candidate, Department of Science, Chiang Mai University, Chiang Mai, Thailand.*

* Corresponding Author Email: Hossein_ghanbari@ind.iust.ac.ir (Hossein Ghanbari)

URL: https://www.acerp.ir/article_206528.html

ARTICLE INFO

Article History:

Received: 11 February 2024
Revised: 09 May 2024
Accepted: 07 September 2024

Keywords:

Ceramic Floor Tile,
Effective Parameters of Strength,
Quality Control,
Deign of Experiments,

ABSTRACT

The production of ceramic floor tiles requires experimentation to achieve acceptable quality and ensure the successful application of the final product. The strength of ceramic floor tiles depends on various parameters, some of which are controllable, while others are beyond the control of production processes. The design of experiments (DOE) is a cost-effective and efficient method for evaluating the production process through controllable variables. However, poorly designed experiments can lead to incorrect results, causing significant costs and waste. In this paper, we investigate the effects of pressure, firing temperature, and firing time on the strength and quality of ceramic floor tiles using the DOE methodology. The samples were tested for compressive strength following Iran's national standards. Optimal conditions were determined using a model and compared with results obtained from Minitab software. The final results show that the optimal compressive strength derived from Minitab's experimental design is 331 MPa, with parameters of 200 N pressure, 1120°C temperature, 48 minutes, and a 0.02 mesh size. In contrast, GAMS software produced an optimal compressive strength of 338 MPa under conditions of 200 N pressure, 1150°C temperature, 48 minutes, and 0.02 mesh size. The 8 MPa difference is attributed to rounding and the specialized analytical capabilities of both GAMS and Minitab.

https://doi.org/10.30501/acp.2024.441815.1148

1. INTRODUCTION

Quality is a concept that has been important to humans since ancient times. Quality is a term that has different meanings and concepts. According to ISO (2005), it refers to the personal characteristics of products that meet customers' needs. The British Standards Organization (1991) defined product and service quality as the use of high-quality materials, high performance, and the highest reliability to meet customer satisfaction and needs. Hatoush (1997) defines quality as a set of characteristics in products or services that meet specific requirements. Barrett (2000) observes that quality in manufacturing can satisfy a broad array of stakeholders. Additionally, Sanvido et al. (1992) emphasize that quality manufacturing projects, when successfully implemented, can lead to customer satisfaction and meet their expectations. Improving quality and efficiency is integral to the design cycle as well as to product and process development.

Please cite this article as: Mardani Ghahfarrokhi, P., Sahragard, R., Ghanbari, H., Safari, M., "Identifying Effective Parameters for Ceramic Floor Tile Strength Using Design of Experiments Methodology", ***Advanced Ceramics Progress***, Vol. 9, No. 4, (2023), 32-40. https://doi.org/10.30501/acp.2024.441815.1148

Employing the design of experiments (DOE) method early in new product development cycles, as well as in improving existing products and optimizing manufacturing processes, is crucial for achieving product success. DOE, or Design of Experiments, has been recognized as a method for quality improvement since the late 19th century, gaining prominence as a competitive advantage in Japan and Western countries around 1990. DOE helps identify critical variables influencing product characteristics, systematically modifies controllable input parameters, and impacts the final product features. This statistical approach significantly reduces variations in quality characteristics and determines optimal levels for controllable variables to enhance process performance. Frequently employed in the preliminary stages of production as a quality control method, DOE is particularly valuable in industries like ceramic floor tile manufacturing, where achieving customer satisfaction and meeting specific needs are crucial. Thus, conducting foundational experiments is essential to ensure the quality and successful application of ceramic floor tile products.

The strength of ceramic floor tile products depends on several parameters, some of which are controllable and some of which are beyond production control. When the effectiveness of controllable variables on strength is measured, it can play an important role in improving the quality of ceramic floor tile end products and ultimately customer satisfaction. Overall, the main tile manufacturing process includes the following steps:

- Homogenization and grinding of primary materials
- Drying of slurries and production of granules
- Shaping by pressing
- Drying
- Application of slipware and glaze
- Printing of the pattern on the tile
- Firing of the products

In each production step, there are controllable variables that can affect the quality of the final product. In addition, there are various tests at the end that ensure product quality. Compressive strength testing is one of the tests that ensure the quality of the final product in this industry. In brittle materials, fracture occurs at maximum load, so tensile strength and breaking strength are combined. In very brittle materials, which include most ceramics, yield, tensile, and fracture stress are united. The bending test is an experiment in which a piece of ceramic (see Figure 1) is loaded at three points. The center shaft on the ceramic is a loading jaw, and the other two shafts on the sides are support bearings. In this test, the standard bending test is set at 300 for floor tiles and 115 for wall tiles.

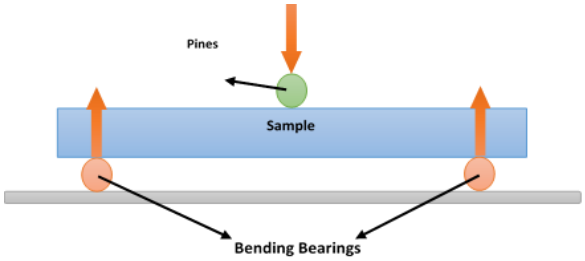

Figure 1. Bending test experiment

In the current article, we propose an innovative approach to examining the compressive strength of tiles in a new environment. This research utilizes a mathematical model tailored to this new environment and its corresponding parameters. Ultimately, the optimal value under the conditions of this new environment was obtained using GAMS software. The experimental design was also conducted using Minitab software, and its results were compared with the outcomes obtained from GAMS. The methodology employed in this research contributes to enhancing the accuracy and efficiency in evaluating the compressive strength of tiles in the studied environment.

The remainder of this paper is organized as follows: Section 2 provides a literature review of related studies. Section 3 outlines the objectives and assumptions of this study. Section 4 describes the research methodology. Section 5 presents the experimental results and discussion. Finally, Section 6 concludes the study.

2. Literature Review

Porcelain tiles are prepared from kaolin, silica sand, feldspar, clay raw materials, and various additives. Ceramic powders are calcined at different temperatures after grinding, drying, and sieving. After the powders are formed and dried, they are sintered at different temperatures. Firing shrinkage (FS), water absorption (WA), and three-point flexure tests of the samples are compared (Durgun & Abalı, 2022). As mentioned earlier, the quality of the final tile and ceramic products is affected by controllable and non-controllable variables at different levels of manufacturing. Since the non-controllable variables are outside our scope of monitoring and control, we focus mainly on the controllable variables. Soil meshing is a measure used to sort soil grains. Soils are graded according to the obtained results from meshes or different sizes of their grains. Soil meshing is an important part of soil mechanics, especially in foundation engineering, because the size of soil grains explicitly affects the behavior and properties of soil, such as shear stress, compressibility, and permeability (Jordán et al., 2009). The powder used for the production of body cookies has a specific formula and consistent moisture content, which is obtained from the spray dryer and formed by the powder pressing process at defined pressures. Evaluations of the body properties

show that the powder sizes in the finished body and the amount of pressing pressure have a significant effect on the strength of the tile (ASTM, 2009). We describe that the powder particles displace and move during the formation of the tile body due to compressive forces, which are important parameters for the compressibility of the tile body. The increase in particle distribution in a cookie is accompanied by a decrease in porosity and is an important variable for increasing flexural strength. Hao (1999) studied the effect of hydraulic device pressure on the compressibility of the cookie body in the molding area and also the effect on the strength of the final product based on finite element analysis. Jiang Ing (2001) also described the effect of the compression area on the improvement of product quality based on the standards available in this industry. In the articles published in the field of pressing range, the standard pressure is set at a maximum of 250 bar (Croseck & Jung, 1982; Silva et al., 2014; Thiers et al., 2018).

In addition to the controllable variables mentioned above, there are others that can affect the quality of the final product. Ceramic parts have low strength after drying and can be crushed with a minimum of force or turned into clay by reabsorption of water and destruction. To increase the strength of the body, the parts must be fired. The firing of ceramics is done in a kiln, for which there are different models, but usually, a roller kiln is used because it has the necessary flexibility for short cycles, in which, due to the action of heat, clean particles combine and increase the strength of the part. When firing ceramic parts, each composition has specific run-out temperature ranges. Depending on the composition, the run-out temperature varies with the heat temperature. The following table shows the temperature ranges. The declared temperatures may differ for different compositions (Baccour et al., 2009; Edelson & Glaeser, 1986).

TABLE 1. Removed Compositions in different temperatures from tile biscuit

Carbonates, Sulfates, Crystallized water	Carbon and Organic Compositions	Humidity
Carbonates 400-1000 C	Some of Organic compositions Between 200-300 C	About 200 C
Sulfates Over than 1000 C	Carbon up to 1000 C	
Crystallized Water Over than 400 C		

Manfredini and Romagnoli (1999) presented a suitable temperature for baking brick cookies between 1050 and 1180 degrees Celsius. They also studied the existing compositions in clay and their effects on the flexural strength of bricks. Finally, they introduced clay with the appropriate number of compositions to produce bricks with suitable strength. Hamisi et al. (2014) studied the effects of firing temperature on the physical properties of bricks and ceramics. They described a suitable temperature for baking tiles between 1100 and 1150 degrees Celsius, noting that all compositions that need to leave the cookie come out at this temperature. The duration of the baking cycle in the oven is another controllable variable in the manufacturing process of the tiles, which depends on the type of tiles. For example, the cycle for baking single-wall tiles is less than 50 minutes. From the studied articles, the importance of paying attention to the bottom grid, the correct pressure during pressing, the firing time in the kiln, and the temperature, which significantly impact the strength of the tiles and the final ceramic product, can be seen. We can use statistical methods to evaluate the influence of these parameters on bending strength, which are also used to improve the production process. One of the most important statistical methods is the DOE method. DOE is used to determine the relationships between the effective parameters of a process and its results. In the final analysis of the results of these experiments, the parameters that significantly impact the results are identified (Montgomery, 2017). In similar research, we can refer to the work of Hınıslıoğlu and Bayrak (2004), in which the flexural strength of concrete is improved by using the DOE.

Many studies have been conducted on the influence of different parameters on the resistance of floor tiles. For example, Meena et al. (2024) introduce innovative bamboo and marble dust ceramic systems, highlighting their superior qualities and significant impact on crystalline phase composition. By partially replacing marble powder with bamboo dust, it offers a novel approach to ceramic tile production, demonstrating promising results in terms of rupture modulus and meeting or exceeding specifications for water absorption, loss of ignition, tile strength, and linear shrinkage. Castillo et al. (2021) gathered informative insights into various variables influencing the compressive strength of floor ceramic tiles, such as temperature and baking time, type and concentration of alkaline activator, water content, and impurity effects. Tahiwa et al. (2023) evaluated the effect of high temperatures up to 800 degrees Celsius on the compressive strength of ceramics. Ercioglu Akdogan et al. (2023) contend that process control in tile baking is highly challenging, considering it the most crucial stage in ceramic production. In their research, they employ manufacturing technology and statistical methods together to produce low-cost, high-quality products at optimal baking temperatures and times. Eren Gültekin (2018) investigated the effects of heating rate and sintering temperature on the strength, shrinkage, and apparent density of ceramic tiles. In their study, experiments were designed as a 32-factor full factorial design, where the individual effects of the two main factors and their interaction were determined. The values of resistance, shrinkage intensity, and apparent

density were analyzed using MINITAB 17 statistical software. They concluded that the interaction effect of heating rate and sintering temperature influences strength, shrinkage, and apparent density, and as a main factor, the effect of sintering temperature is significant. Ochen et al. (2021) addressed the investigation of quartz particle size (larger than 45 micrometers) and its detrimental effects on the physical and mechanical properties of ceramic tiles. They believe this adverse effect is due to various factors, including the microstructure (pores) post-sintering. In their study, they examined the influence of quartz particle size (QPS) on the firing behavior and flexural strength of ceramic tiles made from raw materials. Zamani et al. (2023) conducted a study on the investigation and optimization of the composition and firing temperature of ceramic tiles using statistical analysis techniques. In their research, they employed a full factorial design, which included model adequacy assessment, analysis of variance, Pareto charts, interaction plots, regression modeling, and response surface optimization. Key factors included Seger ratios of SiO2/Al2O3, Na2O/K2O, MgO/CaO, and firing temperature. Their research findings indicate that optimal properties, such as maximum strength, can be achieved with SiO2/Al2O3 = 5.2, Na2O/K2O = 1.50, MgO/CaO = 3.0, and a firing temperature of 1180 degrees Celsius.

The response data were analyzed using ANOVA (analysis of variance) by the Taguchi method. According to the ANOVA table, the water and silicate vapor contents play an important role in the primary flexural strength. Balak and Zakeri (2016) also used DOE to improve the flexural strength of composites. They analyzed nine parameters, such as temperature, time, and pressure, in four stages using statistical analysis of variance. In the current article, we propose an innovative approach to examining the compressive strength of tiles in a new environment. This research utilizes a mathematical model tailored to this new environment and its corresponding parameters. Ultimately, the optimal value under the conditions of this new environment was obtained using Gams software. The experimental design was also conducted using Minitab software, and its results were compared with the outcomes obtained from Gams. The methodology employed in this research contributes to enhancing the accuracy and efficiency in evaluating the compressive strength of tiles in the studied environment.

3. Objectives and Assumptions

In this paper, we intend to study the compressive strength of ceramic floor tile products based on the effective parameters (amount of bottom mesh, suitable pressure during pressing, firing time, and temperature in the kiln) identified in previous research. Our goal is to select the best-optimized conditions. Using a two-step DOE approach, we will sort all the necessary tests and then evaluate the strength quality of the products with the assistance of the strength testing laboratory. It is important to note that this laboratory operates within the quality control department of Birjand Niloufar Tile Company in collaboration with the factory. The quantities provided in Table 2 of the DOE align with all company restrictions and established standards for the ceramic tile industry.

TABLE 2. Effective Parameters range in research

Level	A	B	C	D
	Pressure (N)	Temp.(C)	Time (Min)	Mesh
(- 1) Low	200	1120	45	0.02
(+1) High	220	1150	48	0.04

4. Research Methodology

Quality improvement and industrial manufacturing efficiency are only effective when integrated into every part of the design and production cycle. The precise application of statistical methods like DOE can streamline production processes, enhance safety, and improve system functionality. Moreover, these methods allow for significant portions of product design, development, and related activities to be reusable, thus enhancing overall efficiency and innovation.

The DOE approach was utilized to analyze and model the process, incorporating full factorial designs, fractional designs, and central composite designs. Factorial designs investigate the impact of two or more variables on a response variable. When these variables in the factorial designs have two levels, the number of trials required is represented as 2k, where k is the number of variables. Full factorial designs establish a linear relationship between the independent variables and the response variables. As the number of independent variables increases, the number of experiments required for full factorial designs also increases.

As mentioned earlier, four effective independent variables for the strength of ceramic floor tile products were identified and used in this article: floor mesh, appropriate pressure during pressing, baking time, and temperature in the oven. To study the effects of the identified parameters, the experiment must be conducted randomly. These experiments were conducted using a four-factorial design with four factors: suitable pressure during pressing (A), baking temperature in the oven (B), baking time in the oven (C), and amount of bottom mesh (D), each at two levels with two iterations. The high level (the highest amount for a factor, considering the constraints available in the company) and the low level (the lowest amount for each factor, considering the constraints available in the company) for each variable are shown in Table 2. After configuring the samples for the strength experiment, a product sample is prepared according to the specified amounts for the variables, and the flexural strength is tested. The results are presented in Table 3.

TABLE 3. Tile strength in exchange for different levels of study

10	pattern	Independent Variables				Response Variable	
		A	B	C	D	R1	R2
1	1	-1	-1	-1	-1	278	287
2	A	1	-1	-1	-1	224	245
3	B	-1	1	-1	-1	343	318
4	AB	1	1	-1	-1	245	253
5	C	-1	-1	1	-1	328	334
6	AC	1	-1	1	-1	290	267
7	BC	-1	1	1	-1	276	243
8	ABC	1	1	1	-1	232	254
9	D	-1	-1	-1	1	340	302
10	AD	1	-1	-1	1	220	290
11	BD	-1	1	-1	1	280	298
12	BAD	1	1	-1	1	330	266
13	CD	-1	-1	1	1	356	300
14	ACD	1	-1	1	1	296	265
15	BCD	-1	1	1	1	178	232
16	ABCD	1	1	1	1	234	289

The overall approach to statistical analysis 2k includes the following:

1. Evaluation of factor effects, resistance and variable index
2. Running the primary model
3. Statistical test
4. Running the final model
5. Analysis of the residuals
6. Analysis of the results

5. Experimental Results

5.1. Evaluation of factor effects, resistance and variable index

Table 4 shows the results of these evaluations. The coded variable indices were used to estimate the indices of the regression model. Table 4 presents the primary number of the model:

$$Resp = 277.90 - 15.41A - 10.97B + 11.34AB - 4.53C + 7.91AC - 20.16BC + 6.16ABC + 1.84D - 7.09AD - 5.41BD + 24.97ABD - 0.34CD + 0.34ACD + 1.03BCD - 2.53ABCD$$

TABLE 4. Table of Resistance and Effect

	Independent Variables														
Patterns	ABCD	BCD	ACD	CD	ABD	BD	AD	D	ABC	BC	AC	C	AB	B	A
1	+	-	-	+	-	+	+	-	-	+	+	-	+	-	-
A	-	-	+	+	+	+	-	-	+	+	-	-	-	-	+
B	-	+	-	+	+	-	+	-	+	-	+	-	-	+	-
AB	+	+	+	+	-	-	-	-	-	-	-	-	+	+	+
C	-	+	+	-	-	+	+	-	+	-	-	+	+	-	-
AC	+	+	-	-	+	+	-	-	-	-	+	+	-	-	+
BC	+	-	+	-	+	-	+	-	-	+	-	+	-	+	-
ABC	-	-	-	-	-	-	-	-	+	+	+	+	+	+	+
D	-	+	+	-	+	-	-	+	-	+	+	-	+	-	-
AD	+	+	-	-	-	-	+	+	+	+	-	-	-	-	+
BD	+	-	+	-	-	+	-	+	+	-	+	-	-	+	-
BAD	-	-	-	-	+	+	+	+	-	-	-	-	+	+	+
CD	+	-	-	+	+	-	-	+	+	-	-	+	+	-	-
ACD	-	-	+	+	-	-	+	+	-	-	+	+	-	-	+
BCD	-	+	-	+	-	+	-	+	-	+	-	+	-	+	-
ABCD	+	+	+	+	+	+	+	+	+	+	+	+	+	+	+
Resistance	-81	33	11	-11	799	-173	-227	59	197	-645	253	-145	363	-351	-493
Effect	-5.06	2.06	0.69	-0.69	49.94	-10.81	-14.19	3.69	12.31	-40.31	15.81	-9.06	22.69	-21.94	-30.81
Variable Index	-2.53	1.03	0.34	-0.34	24.97	-5.41	-7.09	1.84	6.16	-20.16	7.91	-4.53	11.34	-10.97	-15.41

5.2. Statistical test

The analysis of variance can be found in Table 4. In this table, the magnitude of the F-value and the p-value can be used to comment on the effectiveness of the factors on the response variables. Since the experiments were conducted with an error level of 0.05, all factors with a p-value less than 0.05 are considered effective in our model. Moreover, according to the table. Moreover, according to the table, $F_{0.05,1.16} = 4.49$, the factors with f-values above 4.49 have an effect.

TABLE 5. Variance analysis related to a case study in tile industry

Source	DF	Adj SS	Adj MS	F-Value	P-Value
Model	15	41785.2	2785.7	3.69	0.007
Linear	4	12211.1	3052.8	4.04	0.019
press	1	7595.3	7595.3	10.06	0.006
temp	1	3850.0	3850.0	5.10	0.038
time	1	657.0	657.0	0.87	0.365
mesh	1	108.8	108.8	0.14	0.709
2-Way Interactions	6	24224.4	4037.4	5.35	0.003
press*temp	1	4117.8	4117.8	5.46	0.033
press*time	1	2000.3	2000.3	2.65	0.123
press*mesh	1	2831.3	2831.3	3.75	0.071
temp*time	1	13000.8	13000.8	17.23	0.001
temp*mesh	1	935.3	935.3	1.24	0.282
time*mesh	1	1339.0	1339.0	1.77	0.202
3-Way Interactions	4	5144.6	1286.2	1.70	0.198
press*temp*time	1	1212.8	1212.8	1.61	0.223
press*temp*mesh	1	3894.0	3894.0	5.16	0.037
press*time*mesh	1	3.8	3.8	0.01	0.944
temp*time*mesh	1	34.0	34.0	0.05	0.835
4-Way Interactions	1	205.0	205.0	0.27	0.609
press*temp*time*mesh	1	205.0	205.0	0.27	0.609
Error	16	12075.5	754.7		
Total	31	53860.7			

To identify effective factors in the response variables, factorial effects and reciprocal effects diagrams can also be used (Figures 2 and 3, respectively). In Figure 2, the slope of each factor indicates the intensity of its effect on the response variable. Thus, we conclude that the effects of factors A and B (pressure and temperature) are stronger than those of factors C and D (time and mesh size). Moreover, a positive slope indicates a direct effect on the response variable, while a negative slope indicates an inverse effect.

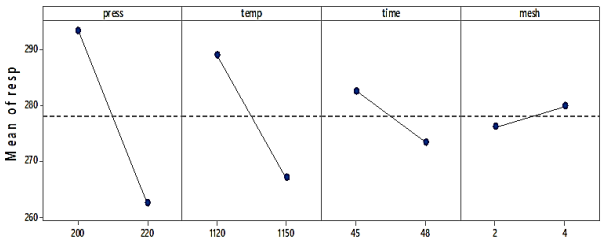

Figure 2. Factorial Effects

Figure 3 shows the reciprocal effects of the factors. In this figure, changes in the factors lead to the intersection of their responses. We can assert that the simultaneous change in the factors is effective; however, to determine the level at which the two factors influence the response variables, we need to utilize contour plots, as illustrated in Figures 4 and 5.

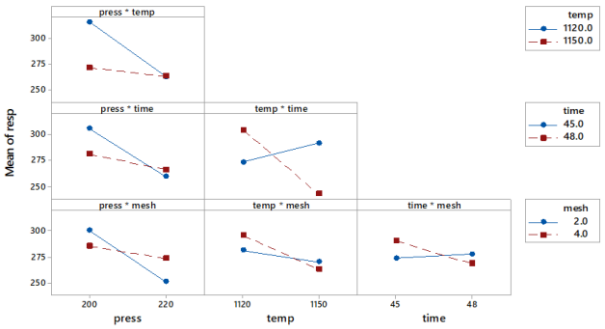

Figure 3. Interaction effects

Figure 4 illustrates the dual effects considering the low level of the independent variables, while Figure 5 depicts the dual effects at the high level of the other variables. The bold areas in each graph indicate the largest effect of these variables on the response variable analyzed below.

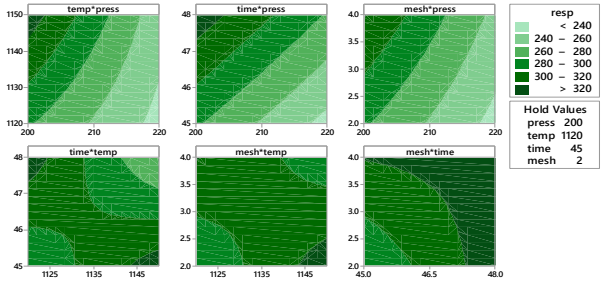

Figure 4. Counter diagram at low level of the variable

TABLE 6. Most response domains in dual effects exchange considering a low level of other independent variables

	Press (N)	Temp (C)	Time (Min)	Mesh
Up- Left side	200	1150	45	2
Up- Center	200	1120	48	2
Up-Right	200	1120	45	2
Down-left (two levels)	200	1120	48	2
	200	1150	45	2
Down-Center	200	1150	48	2
Down- Right	200	1120	48	4,2

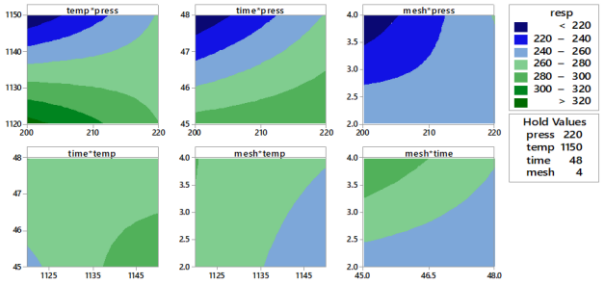

Figure 5. Counter diagram in high levels of variables

TABLE 7. Maximum response surface in dual effects exchange considering a high level of other independent variables

	Press (N)	Temp (C)	Time (Min)	Mesh
Up-Left	200	1120	48	4
Up-Center	In other diagrams there are not bold green (Maximum response area)			
Up-Right				
Down-Left				
Down-Center				
Down- Right				

In Figure 5, only the upper left diagram contains the largest range for the response variables (bold green area), while the other diagrams do not. From these graphs, we can observe the effects of the various factors on the response surface, but we cannot infer the most effective factors. For this purpose, we will use Pareto and normal diagrams, as shown in Figures 6 and 7.

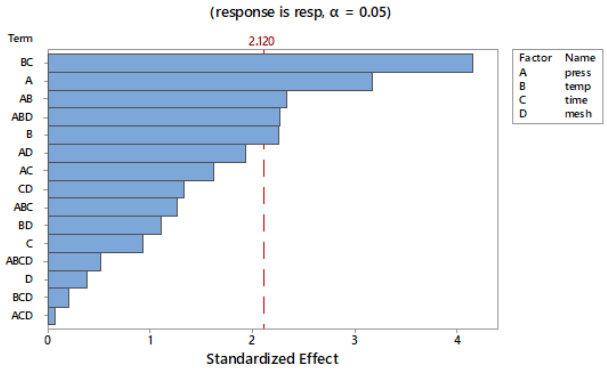

Figure 6. Pareto diagram

According to the Pareto diagram and the influence limit of the response variables (2.120), the effective factors are determined. This is also evident from the normalized diagram in Figure 9. It is important to note that the greater the distance between the 16 individual effects and the reciprocal elements in Table 2 and the normalized line, the greater the effect of the respective factor on the response variable.

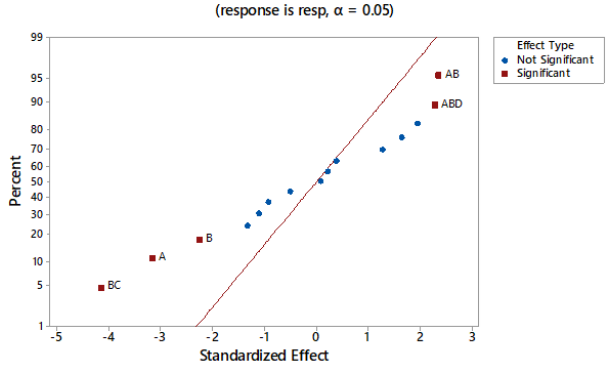

Figure 7. Normalized diagram

The Pareto charts and the normalized charts show the results of the variance table. Therefore, we can refer to the table at the beginning and observe which parameters affect the analysis of variance.

5.3. Model correction (Final model)

The primary model was redesigned according to the previous conclusions as follows:

$$RESP = 277.90 - 15.41(PRESS) - 10.97(TEMP) - 20.16(TEMP)(TIME) + 11.34(PRESS)(TEMP) + 24.97(PRESS)(TEMP)(MESH)$$

5.4. Residual analysis

After defining the regression model, estimate the different quantities from the experiments using this model and calculate the difference between the actual quantities and the predicted quantities. Before accepting the results of the analysis of variance and finalizing the model, check the residuals of this experiment (the difference between actual and predicted quantities) to determine if they are normal and random, ensuring valid results. Figures 8 and 9 show the normal plot of residuals (clustered around the line) and the plot validating random observations, respectively.

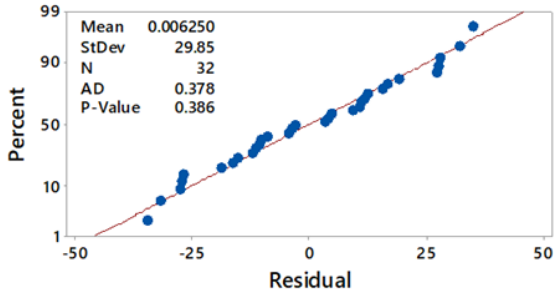

Figure 8. Randomness validation of the amount of residuals

Based on Figure 8, the p-value is validated to be normal (greater than 0.05).

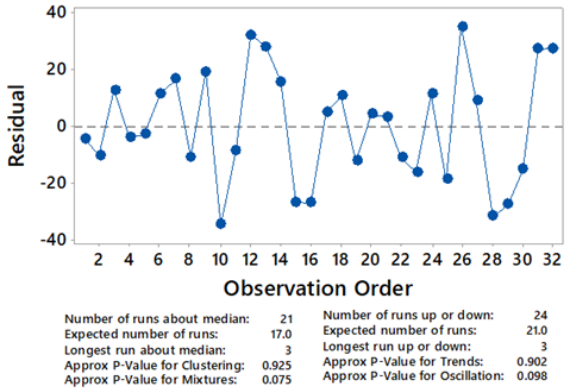

Figure 9. Normal **validation** test of residuals

Based on Figure 9, the p-values confirm randomness (each of the four elements is greater than 0.05). The competency evaluation of the model shows that the residual analysis of this model is satisfactory.

5.5. Analysis of results

To obtain the optimal answer, the Gams and Minitab software are used with the results compared.

5.5.1. Analysis with GAMS software

To obtain the optimized answer, the following model is used:

$$\text{Max resp: } 277.90 - 15.41 * x_1 - 10.97 * x_2 - 20.16 * x_2 * x_3 + 11.34 * x_1 * x_2 + 24.97 * x_1 * x_2 * x_4$$
$$-1 \le x_1 \le +1$$
$$-1 \le x_2 \le +1$$
$$-1 \le x_3 \le +1$$
$$-1 \le x_4 \le +1$$

The optimized answer in the software GAMS can be found below:

TABLE 8. The optimized answer of the proposed model

resp	A	B	C	D
338.81	-1	1	1	-1

The coded variables are converted to decoded variables at the end, given below:

TABLE 9. The converted variables

resp	A	B	C	D
338.81	200	1150	48	0.02

The following figure shows the subtitle of the final answer in the GAMS software.

TABLE 10. Optimized answer in Gams Software

34 Variable Z.L				338.810			
34 Variable X.L							
1	-1.000	2	1.000	3	1.000	4	-1.000

5.5.2. Analysis with Minitab software

According to the results from Minitab software, the optimized set of response variables is also 331, which aligns with the sets of Mesh = 2, Time = 48, Temperature = 1120, and Pressure = 200.

TABLE 11. Results from Minitab software

Solution	Goal	press	temp	time	mesh	Resp Fit	Composite Desirability
1	Maximum	200	1120	48	2	331	0.839744

6. Conclusion

One of the competitive advantages in the ceramic tile industry is the emphasis on the final quality of ceramic floor tiles, particularly their compressive strength. To enhance this attribute, numerous controllable variables can be manipulated. The DOE approach is particularly well-suited for studying these specific variables. This study aimed to investigate the quality of ceramic floor tile products by identifying several critical and influential factors: the amount of floor mesh, the appropriate pressure during pressing, firing time, and kiln temperature. These variables were tested using experimental designs and factorial patterns at two levels—high and low. The optimized conditions for the independent variables were determined using the created model, with results analyzed through Minitab software and compared to those obtained from the model. Notably, the 8-unit difference between the optimized values from Minitab and those from GAMS is attributed to rounding when configuring the model for use in GAMS. The final results reveal that the optimal compressive strength achieved through the experimental design, as calculated in Minitab, is 331 megapascals. This result was obtained under the following conditions: a pressure of 200 newtons, a temperature of 1120 degrees Celsius, a duration of 48 minutes, and a mesh size of 0.02. Conversely, the mathematical model solved in GAMS suggests an optimal compressive strength of 338 megapascals, achieved with identical parameters except for a higher temperature of 1150 degrees Celsius. The discrepancy of 8 units between the results from GAMS and Minitab is due to the rounding of numbers in the GAMS model, whereas Minitab offers more specialized capabilities in analyzing and retrieving optimal solutions in experimental design.

Declaration of Conflicting Interests

The authors declared no potential conflicts of interest with respect to the research, authorship, and/or publication of this article.

Acknowledgements

The authors wish to express their appreciation for several excellent suggestions for improvements in this paper made by the anonymous referees.

REFERENCES

1. ASTM Committee D-18 on Soil and Rock. (2009). Standard test methods for particle-size distribution (gradation) of soils using sieve analysis. ASTM international. https://www.astm.org/d6913_d6913m-17.html
2. Baccour, H., Medhioub, M., Jamoussi, F., & Mhiri, T. (2009). Influence of firing temperature on the ceramic properties of Triassic clays from Tunisia. Journal of materials processing technology, 209(6), 2812-2817, https://doi.org/10.1016/j.jmatprotec.2008.06.055.
3. Balak, Z., & Zakeri, M. (2016). Application of Taguchi L32 orthogonal design to optimize flexural strength of ZrB2-based composites prepared by spark plasma sintering. International Journal of Refractory Metals and Hard Materials, 55, 58-67, https://doi.org/10.1016/j.ijrmhm.2015.11.009.
4. Barrett, P. (2000). Systems and relationships for construction quality. International Journal of Quality & Reliability Management, 17(4/5), 377-392, https://doi.org/10.1108/02656710010298409.

5. Castillo, H., Collado, H., Droguett, T., Sánchez, S., Vesely, M., Garrido, P., & Palma, S. (2021). Factors affecting the compressive strength of geopolymers: A review. Minerals, 11(12), 1317, https://doi.org/10.3390/min11121317.
6. Croseck, H. H., & Jung, R. (1982). U.S. Patent No. 4,350,486. Washington, DC: U.S. Patent and Trademark Office. https://www.uspto.gov
7. da Silva, A. L., Bernardin, A. M., & Hotza, D. (2014). Forming of thin porcelain tiles: a comparison between tape casting and dry pressing. Ceramics International, 40(2), 3761-3767, https://doi.org/10.1016/j.ceramint.2013.09.044.
8. Durgun, R., & Abalı, S. (2022). Effect of calcination and sintering temperature on porosity and microstructure of porcelain tiles. Materials Testing, 64(3), 391-400, https://doi.org/10.1515/mt-2021-2069.
9. Edelson, L. H., & Glaeser, A. M. (1986). Method for removing surface porosity on glassy carbon tiles. Carbon, 24(5), 635-637, https://doi.org/10.1016/0008-6223(86)90153-3.
10. Ercioglu Akdogan, N., Arioz, E., & Kockar, O. M. (2023). Investigation of Physico-Mechanical Properties and Multi-Objective Optimization of Industrial Ceramic Tiles Using Response Surface Method: Sintering Temperature and Time. Transactions of the Indian Ceramic Society, 82(3), 177-186, https://doi.org/10.1080/0371750X.2023.2216763
11. Eren Gültekin, E. E. (2018). The effects of heating rate and sintering temperature on the strength, firing shrinkage, and bulk density of porcelain tiles. Journal of the Australian Ceramic Society, 54, 39-46, https://doi.org/10.1007/s41779-017-0124-9.
12. Hamisi, H., Park, S. E., Choi, B. H., An, Y. T., & Lee, J. (2014). Influence of firing temperature on physical properties of same clay and pugu kaolin for ceramic tiles application. International Journal of Materials Science and Applications, 3(5), 143-146, https://doi.org/10.11648/j.ijmsa.20140305.12.
13. Hatush, Z., & Skitmore, M. (1997). Evaluating contractor prequalification data: selection criteria and project success factors. Construction Management and Economics, 15(2), 129-147, https://doi.org/10.1080/01446199700000002.
14. Hınıslıoğlu, S., & Bayrak, O. Ü. (2004). Optimization of early flexural strength of pavement concrete with silica fume and fly ash by the Taguchi method. Civil Engineering and Environmental Systems, 21(2), 79-90, https://doi.org/10.1080/10286600410001684562.
15. Jordán, M. M., Martín-Martín, J. D., Sanfeliu, T., Gómez-Gras, D., & De la Fuente, C. (2009). Mineralogy and firing transformations of Permo–Triassic clays used in the manufacturing of ceramic tile bodies. Applied Clay Science, 44(1-2), 173-177, https://doi.org/10.1016/j.clay.2009.01.018.
16. Manfredini, T., & Romagnoli, M. (1999). Iron-and calcite-rich ceramic bodies for porous tiles manufacturing by fast double-firing. Interceram, 48, 159-167. https://iris.unimore.it/handle/11380/310227
17. Meena, R., Mallik, M., Yadav, R., Meena, A., & Hashmi, A. W. (2024). Investigation of physical properties of bamboo dust with marble powder filled ceramic composites: Sustainable approach for ceramic tiles manufacturing. Proceedings of the Institution of Mechanical Engineers, Part L: Journal of Materials: Design and Applications, 14644207231225067, https://doi.org/10.1177/14644207231225067.
18. Montgomery, D. C. (2017). Design and analysis of experiments. John wiley & sons. https://www.google.com/books/edition/Design_and_Analysis_of_Experiments/Py7bDgAAQBAJ?hl=en&gbpv=0
19. Ochen, W., D'ujanga, F. M., Oruru, B., & Olupot, P. W. (2021). Physical and mechanical properties of porcelain tiles made from raw materials in Uganda. Results in Materials, 11, 100195, https://doi.org/10.1016/j.rinma.2021.100195.
20. Standard, B., & ISO, B. (2000). Quality management systems-Fundamentals and vocabulary. BSI, GB. https://www.iso.org/standard/29280.html
21. Sanvido, V., Grobler, F., Parfitt, K., Guvenis, M., & Coyle, M. (1992). Critical success factors for construction projects. Journal of construction engineering and management, 118(1), 94-111, https://doi.org//10.1061/(ASCE)0733-9364(1992)118:1(94).
22. Tahwia, A. M., Abd Ellatief, M., Bassioni, G., Heniegal, A. M., & Abd Elrahman, M. (2023). Influence of high temperature exposure on compressive strength and microstructure of ultra-high performance geopolymer concrete with waste glass and ceramic. Journal of Materials Research and Technology, 23, 5681-5697, https://doi.org/10.1016/j.jmrt.2023.02.177
23. Thiers, B., Walmsley-Scott, C., & Van Der Stockt, B. (2018). U.S. Patent No. 9,874,030. Washington, DC: U.S. Patent and Trademark Office. https://www.uspto.gov
24. Vocabulary, Q. (1991). Part 2: Quality Concepts and Related Definitions. British Standard BS, 4778-2. https://www.intertekinform.com/en-us/standards/bs-4778-2-1991-212066_saig_bsi_bsi_501479/
25. Zamani, M., Yapicioglu, H., Kara, A., & Sevik, C. (2023). Statistical analysis of porcelain tiles' technical properties: full factorial design investigation on oxide ratios and temperature. Physica Scripta, 98(12), 125953, https://doi.org/10.1088/1402-4896/ad0ae9.

Advanced Ceramics Progress: Vol. 9, No. 4, (Autumn 2023) 41-49

Materials and Energy Research Center
MERC

Contents lists available at ACERP

Advanced Ceramics Progress

Journal Homepage: www.acerp.ir

Original Research Article

Structural and Phase Stability in the 2TiC-Al-Ti System During Milling and Subsequent Annealing

Khashayar Zamani [a], Majid Tavoosi [b], Ali Ghasemi [c], Gholamreza Gordani [b]

[a] *Ph.D. Candidate, Department of Materials Engineering, Malek- Ashtar University of Technology, Shahin-Shahr, Isfahan, Iran.*
[b] *Associate Professor, Department of Materials Engineering, Malek- Ashtar University of Technology, Shahin-Shahr, Isfahan, Iran.*
[c] *Professor, Department of Materials Engineering, Malek- Ashtar University of Technology, Shahin-Shahr, Isfahan, Iran.*

* Corresponding Author Email: m.tavoosi@gmail.com (Majid Tavoosi)

URL: https://www.acerp.ir/article_206533.html

ARTICLE INFO

Article History:

Received: 20 December 2023
Revised: 08 April 2024
Accepted: 07 September 2024

Keywords:

Ti-Al-C Intermetallic Compound,
Milling,
Heat Treatment,
Phase Stability

ABSTRACT

The aim of the present research was to examine the structural and phase transformations, as well as the phase stability, in the 2TiC-Al-Ti system. A specific ratio of TiC, Al, and Ti powder mixture, based on the stoichiometric reaction for the formation of the Ti3AlC2 compound, was prepared and subjected to milling and annealing processes. The prepared samples were analyzed using scanning electron microscopy (SEM), X-ray diffraction (XRD), and differential scanning calorimetry (DSC). The results showed that milling the 2TiC-Al-Ti powder mixture did not result in the formation of a single-phase Ti3AlC2. Instead, the final structure consisted of a combination of TiC and Ti3AlC2 phases. The Ti3AlC2 phase formed during the milling process was unstable and transformed into a single-phase TiCx structure upon further milling or annealing. Additionally, the effect of the partial addition of Sn and Si on the structural and phase changes in the 2TiC-Al-Ti system during the milling and annealing processes was investigated. It was found that the addition of these elements had little effect on the formation and stability of the Ti3AlC2 compound.

https://doi.org/10.30501/acp.2024.431563.1142

1. INTRODUCTION

Titanium carbide (TiC) forms very stable bonds and does not degrade at any temperature. This carbide is widely used in high-efficiency electrical systems due to its high melting point (3373 °C), as well as its electrical (61 $cm^{-1}\Omega\mu$) and thermal conductivity (33.2 $Wm^{-1}C^{-1}$) (Baviera, et al., 2001). However, the extensive use of TiC has been limited due to its inherent brittleness and tendency for sudden failure. To address this issue, the MAX phase structure has been developed in the Ti-Al-C system. MAX phases are defined by the general formula $M_{n+1}AX_n$, where M represents a transition metal, A is an element from group A (mostly from groups 3, 4, or 5 of the periodic table), and X denotes nitrogen or carbon. These materials exhibit a layered structure and possess unique ceramic and metallic properties (Zhang, et al., 2021) (Kumar, et al., 2022).

The formation of the MAX phase in the Ti-Al-C system has been studied by various researchers, who have used a range of raw materials such as Ti, Al, C, TiAl, TiCx, TiH, Al_2O_3, and Al_4C_3. Different synthesis methods have also been employed, including hot pressing (HP) (Li, et al., 2020) (Yoshida, et al., 2019), hot isostatic pressing (HIP) (Yu, et al., 2020), spark plasma sintering (SPS) (Eryomina, et al., 2021) (Gao, et al., 2020) and self-propagating high-temperature synthesis (SHS)

Please cite this article as: Zamani, Kh., Tavoosi, M., Ghasemi, A., Gordani, Gh. R., "Structural and Phase Stability in the 2TiC-Al-Ti system during Milling and Subsequent Annealing", ***Advanced Ceramics Progress***, Vol. 9, No. 4, (2023), 41-49. https://doi.org/10.30501/acp.2024.431563.1142

(Averichev, et al., 2019) (Pazniak, et al., 2019). For example, Tzenov et al. (Tzenov, et al., 2000) investigated the phase transformation of a Ti, Al_4C_3, and C powder mixture using hot isostatic pressing, applying a pressure of 70 MPa and a temperature of 1400 °C to form the MAX phase. Wang et al. (Wang, et al., 2003) successfully synthesized the Ti_3AlC_2 intermetallic compound via hot pressing (25 MPa at 1500 °C), followed by annealing at 1200 °C. Hongxiang et al. (Hongxiang, et al., 2005) synthesized the Ti_2AlC compound using the SPS method at 1100 °C. They observed that increasing the sintering temperature to 1100 °C caused the Ti_2AlC phase to transform into Ti_3AlC_2, indicating the weaker thermal stability of Ti_2AlC. The work of Łopaciński (Łopaciński, et al., 2001) and Ge et al. (Ge, et al., 2003) on the formation of MAX phases using TiC and Al_4C_3 precursors and the SHS process, and the effect of TiC addition on the formation of the Ti_3AlC_2 compound in Ti/Al/C powder mixtures, represent other significant research efforts in this field. Furthermore, several studies have explored the effect of adding Si and Sn elements on the likelihood of reactions and the prevention of unwanted intermetallic compounds such as TiC and Ti_xAl_y (Cai, et al., 2018) (Cai, et al., 2021) (Guo, et al., 2021).

Despite extensive research on the formation of the Ti_3AlC_2 phase, the formation mechanisms and structural changes of this phase during annealing have not been thoroughly studied. In this regard, the present research aims to explore the structural and phase transformations in the 2TiC-Al-Ti system during milling and annealing processes. In addition, the effect of Si and Sn elements on the formation and thermal stability of Ti_3AlC_2 is investigated.

2. MATERIALS AND METHODS

In this research, raw materials with 99.8% purity and particle sizes of about 30 µm, including Ti, Al, TiC, Sn, and Si, were used to synthesize 2TiC-Al-Ti, 2TiC-Al-Ti-xSn, and 2TiC-Al-Ti-xSi (x = 0.1, 0.2, and 0.3) compounds. The powder samples were prepared by milling using an XQM-2A (Tencan company) at a rotation speed of 400 rpm with a ball-to-powder ratio of 10:1. The milling process was carried out in a tungsten carbide chamber using zirconia balls. The annealing process was performed within a temperature range of 350–1400 °C under an argon atmosphere, with a heating rate of 20 °C/min, using a Nabertherm furnace model HTCT 03/16.

The structural changes in the specimens were monitored using XRD (X-ray diffraction) analysis with a diffractometer (Philips PW3710) equipped with Cu Kα radiation (λ = 0.15406 nm, 40 kV). The measurements were taken with a step size of 0.05° and a time per step of 1 s. Morphological analyses of the powder samples were performed using scanning electron microscopy (SEM) with a VEGA-TESCAN-XMU. ImageJ software was used to determine the average particle sizes of the samples. Additionally, differential scanning calorimetry (DSC) was conducted to evaluate the thermal stability of the produced samples, using a Netzsch STA 409 PC/PG differential thermal analyzer. The samples were placed in Al2O3 pans and heated under a dynamic argon atmosphere (99% purity) up to 1000 °C, with a heating rate of 20 °C/min.

3. RESULTS AND DISCUSSION

The XRD patterns of the 2TiC-Al-Ti powder mixture after various milling times, up to 50 hours, are presented in Fig. 1. As shown, significant changes occur in the diffraction patterns as milling time increases. The XRD patterns of the powder samples at the initial stages of milling contain only the peaks corresponding to the raw materials, with no indication of a reaction. As milling progresses to 25 hours, the peaks related to Ti and Al completely disappear, and new peaks corresponding to the Ti_3AlC_2 phase appear in the XRD pattern.

Temperature measurements within the milling chamber, using a wireless thermocouple monitoring system, indicate that the self-propagating reaction responsible for the formation of the Ti_3AlC_2 phase occurs after approximately 20 hours of milling. The temperature increase during this reaction is estimated to be around 35 $^{\circ}$ C. Fig. 2 shows the DSC heating trace of the 2TiC-Al-Ti powder mixture after 25 hours of milling. Notably, there are no signs of endothermic or exothermic reactions in this trace. The absence of an Al melting peak near 660°C confirms the reaction between the initial materials and the formation of the intended phase during milling. This can be explained by the negative Gibbs free energy change for the formation of the Ti_3AlC_2 phase (ΔG^o = -540 kJ/mol (Shahin, et al., 2016)), as well as the adiabatic reaction temperature of 3643 K, which exceeds the threshold value of T_{ad} > 1800 K. In line with this, Yu et al. (Ye, et al., 1997) reported that exothermic reactions in the Ti-Al-C system result in local temperatures exceeding 1900°C.

It is important to note that the reduction in crystalline size and the increase in crystalline defect density (such as dislocations, voids, and grain boundaries) during the milling process are the primary factors contributing to the instability of the milled samples and the formation of the Ti_3AlC_2 phase (Mossino, et al., 2004). Fig. 3 shows SEM images of the powder particles after 25 hours of milling. As seen, the particles exhibit a pseudo-spherical and uniform morphology, with a mean particle size of approximately 400 nm. There is no evidence of sharp or crushed particles in this image, further supporting that the reaction occurs as a self-propagating process during milling (El-Eskandarany., 2015) (Whang., 2011).

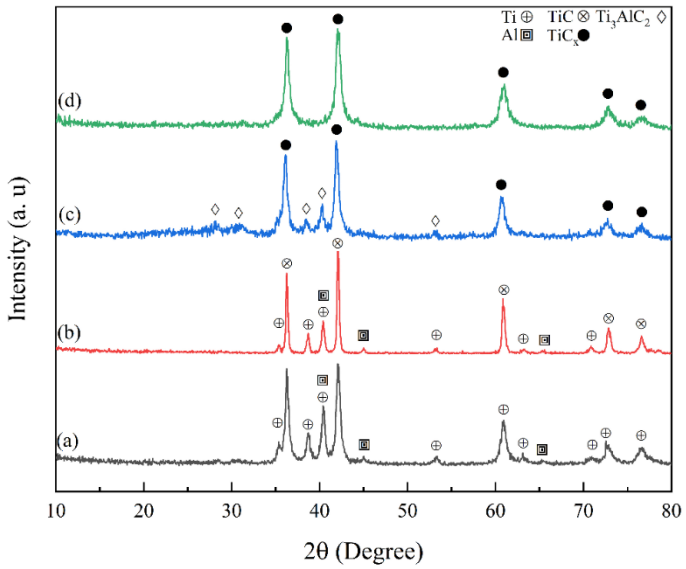

Figure 1. The XRD patterns of 2TiC-Al-Ti powder mixture after different milling periods: a) 0, b) 5, c) 25, and d) 50 h.

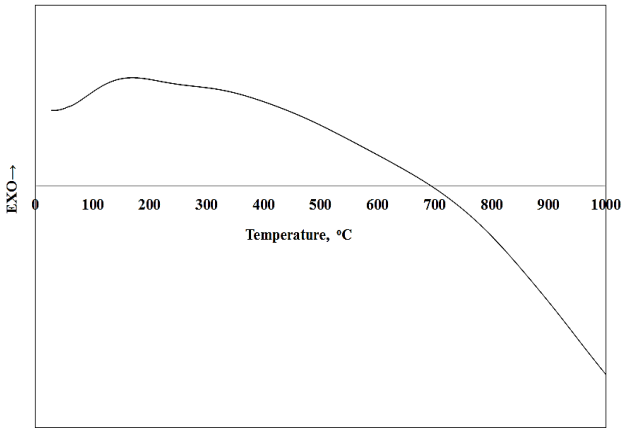

Figure 2. The DSC heating trace of 2TiC-Al-Ti powder mixture after 25 h of milling.

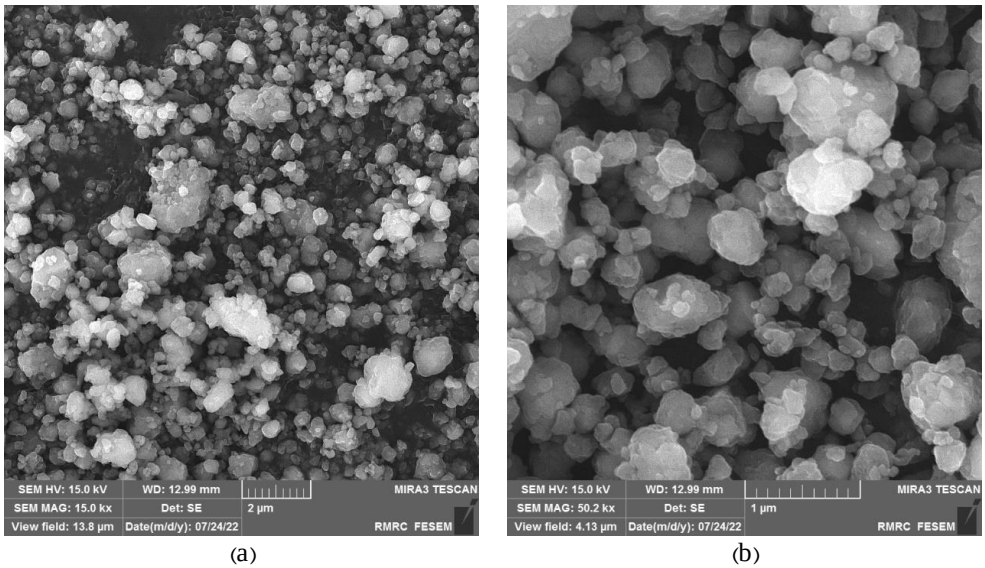

(a) (b)

Figure 3. The SEM micrographs of 2TiC-Al-Ti powder mixture after 25 h of milling (at two different magnifications).

Moreover, as shown in Fig. 1(d), the formed Ti_3AlC_2 compound is unstable and transforms into the TiC_x phase as the milling process continues up to 50 hours. According to the Ti-C equilibrium diagram, the TiC compound is a non-stoichiometric ceramic and remains stable across a wide compositional range ($32 \leq C > 50$ at. %). The formation of a single-phase TiC_x compound in the Ti-Al-C system during milling has also been confirmed by other researchers, such as Li et al. (Li, et al., 2006). However, the sequence of phase transformations in the 2TiC-Al-Ti system during the milling process can be described as follows:

$$2TiC\text{-}Al\text{-}Ti \rightarrow TiC + Ti_3AlC_2 \rightarrow TiC_x \quad (1)$$

To explore the thermal stability of the Ti_3AlC_2 phase produced during the milling process, as well as the potential phase changes during annealing, the 25-hour milled sample underwent heat treatment at temperatures ranging from 350°C to 1400°C. The XRD patterns of the annealed samples are shown in Fig. 4. As observed, with increasing annealing temperature, the intensity of the peaks corresponding to the Ti_3AlC_2 phase gradually decreases and is completely eliminated from the diffraction patterns upon reaching 1000°C. At this point, several peaks corresponding to the TiAl3 phase appear in the diffraction patterns. According to the literature and the Ti-Al-C equilibrium diagram, the stability region of the Ti_3AlC_2 compound is narrow (Bandyopadhyay, et al., 2000), with this phase forming only within the 1350-1450°C range. At other temperatures, this phase gradually decomposes into TiC_x, Ti_2AlC, and Ti_xAl_y intermetallic compounds (Pang, et al., 2010) (Yao, et al., 2015), which is consistent with the results obtained in this study.

As the annealing temperature increases up to 1200°C, the intensity of the peaks corresponding to the $TiAl_3$ phase also increases. These results are in line with the findings of Yoshida et al. (Yoshida., 2012), who reported the formation of $TiAl_3$ and TiAl intermetallic compounds within the 1100-1200°C range in the Ti-Al-C system. Based on Fig. 4, the $TiAl_3$ phase is unstable and gradually disappears from the XRD patterns during annealing up to 1400°C. At this temperature, the XRD pattern of the annealed sample includes only peaks related to the TiC_x compound. The formation of a TiC_x single-phase structure during annealing is similar to the structure produced in the 50-hour milled sample (Fig. 1(d)). This confirms that the stable phase in the 2TiC-Al-Ti system is the TiC_x phase. In other words, the excess Al and Ti dissolve into the carbide network without forming a new phase.

However, this result contrasts with Yoshida's research (Yoshida., 2012), which reported the stability of ternary Ti_3AlC_2 and Ti_2AlC phases between 1200°C and 1400°C. The difference in raw materials and production methods likely explains this discrepancy. The SEM morphological images of the annealed samples at 1400°C are shown in Fig. 5. As seen in this figure, the primary morphological characteristics of the resulting powder particles include a relatively uniform distribution of pseudo-spherical particles with a mean particle size of 300 nm.

The sequence of phase changes in this system during the annealing process can be described as follows:

$$TiC + Ti_3AlC_2 \rightarrow TiC + TiAl_3 \rightarrow TiC_x \quad (2)$$

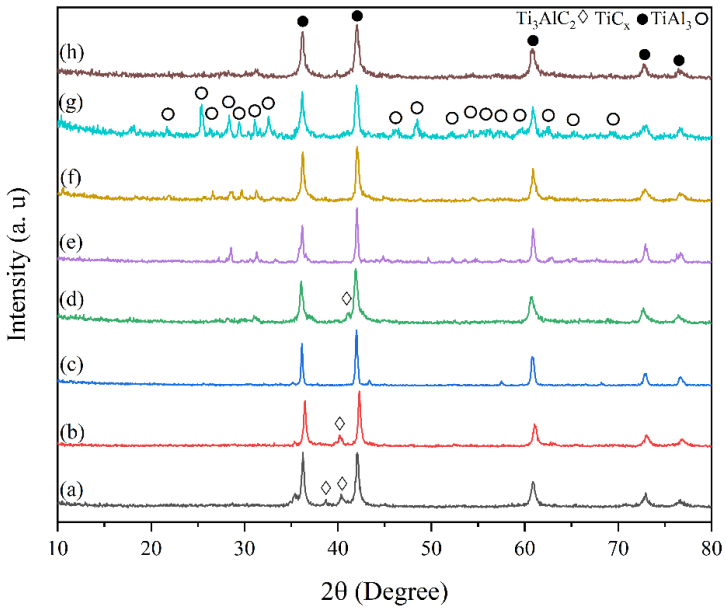

Figure 4. The XRD patterns of 2TiC-Al-Ti milled powder mixture for 25 h after annealing for 1 h: a) 350, b) 700, c) 900, d) 1000, e) 1100, f) 1200, g) 1300 and h) 1400 °C.

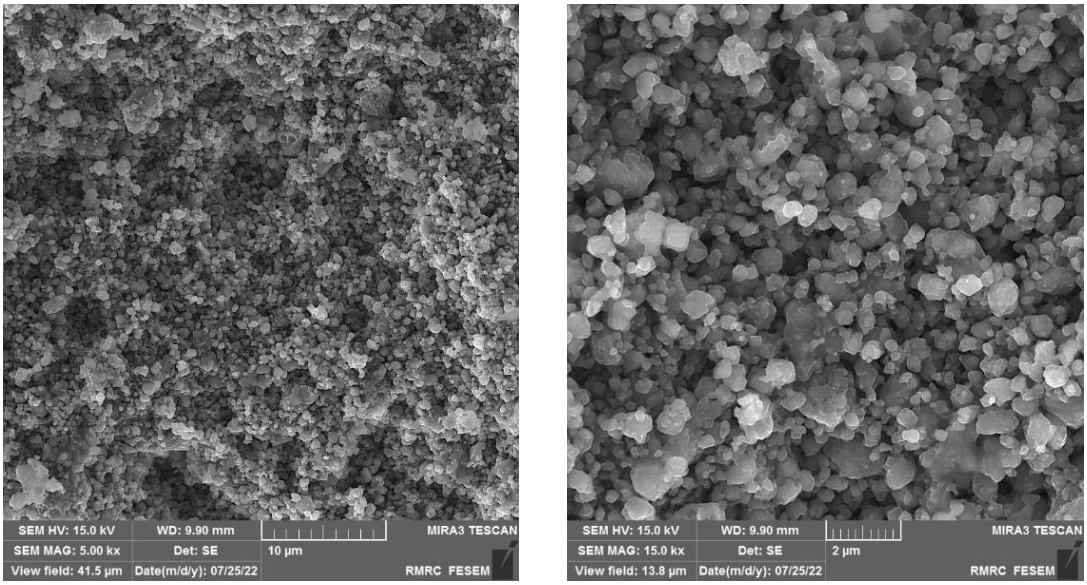

(a) (b)

Figure 5. The SEM micrographs of 2TiC-Al-Ti milled powder mixture for 25 h after annealing at 1400 ºC for 1 h.

According to the literature (Cai, et al., 2018) (Guo, et al., 2021), adding small amounts of Sn and Si elements to the Ti-Al-C system prevents the formation of binary intermetallic compounds such as TiC, Ti_xAl_y, and Al_2O_3, and also prevents thermal explosions. These two elements are incorporated into the intermetallic compound Ti_3AlC_2 as replacement elements for layer A (Al), increasing the density of dislocations. Since Sn and Si are more electronegative than Al, they strengthen the bond between the M-A and A-X layers. In this regard, increasing bond strength may contribute to the stability of the MAX phase. To investigate the effect of Sn and Si on the formation and stability of the Ti_3AlC_2 compound in the Ti-Al-C system, the XRD patterns of the 2TiC-Al-Ti-xSn and 2TiC-Al-Ti-xSi powder mixtures (x = 0.1, 0.2, 0.3) after 25 hours of milling are presented in Figs. 6 and 7, respectively. As observed, the XRD patterns of the examined samples containing these additives consist only of peaks corresponding to TiC_x and Ti_3AlC_2 phases. There is no evidence of Sn and Si in the XRD patterns. This is expected, as the percentage of these two elements is less than 5 vol.%, making them undetectable by XRD.

The absence of the Al melt peak in the DSC curves (Fig. 8) confirms the occurrence of reactions between the components during the milling process. The XRD patterns indicate that the addition of Sn and Si has a detrimental effect on the formation of the mentioned phases in the 2TiC-Al-Ti system. As shown in Figs. 6 and 7, the intensity of the Ti_3AlC_2 peaks decreases as the percentage of Sn and Si in the composition increases. These results contradict the findings of Li et al. (Li, et al., 2008), Mingxing et al. (Mingxing, et al., 2006), and Zhu et al. (Zhu, et al., 2004), who reported that these elements stabilize the Ti_3AlC_2 phase. However, the formation of the Ti_3AlC_2 compound in the 2TiC-Al-Ti system occurs through the SHS reaction during milling. The addition of Sn and Si reduces the local temperature and significantly diminishes the intensity of SHS reactions due to heat absorption, thereby affecting the formation of the resulting phases. In fact, Sn has a more pronounced effect in reducing the intensity of the Ti_3AlC_2 peaks than Si. This is likely due to the lower melting and evaporation temperatures of Sn compared to Si, enabling Sn to absorb more reaction heat and hinder the formation of the Ti_3AlC_2 compound.

The SEM morphological characteristics of the powder mixtures containing 0.1 atomic percent of Si and Sn are compared in Fig. 9. As observed, the morphology of the resulting powders in the presence of these additives is similar to the SEM images presented in Fig. 2, consisting of pseudo-spherical particles with an average size of about 400 nm.

The XRD patterns and SEM micrographs of the samples containing 0.1% Sn and Si after annealing at 1400°C are presented in Figs. 10 and 11. As seen, the phase and morphological structures of the examined samples with additives are very similar to those of the sample without additives, showing no significant differences. In this case, the phase structure consists solely of the TiC_x compound, the particles are spherical, and the average particle size is estimated to be around 300 nm. These results indicate that Sn and Si additives do not significantly influence the formation or stability of the Ti_3AlC_2 phase.

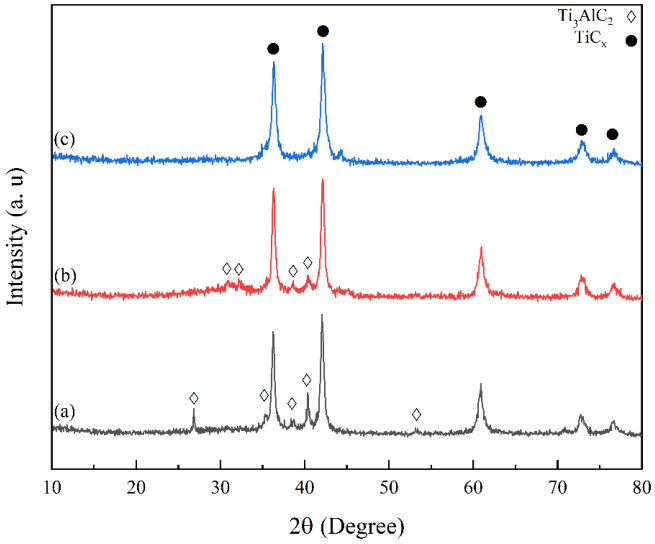

Figure 6. The XRD patterns of 2TiC-Al-Ti-xSn powder mixture after 25 h of milling: a) x=0.1, b) x=0.2 and c) x=0.3.

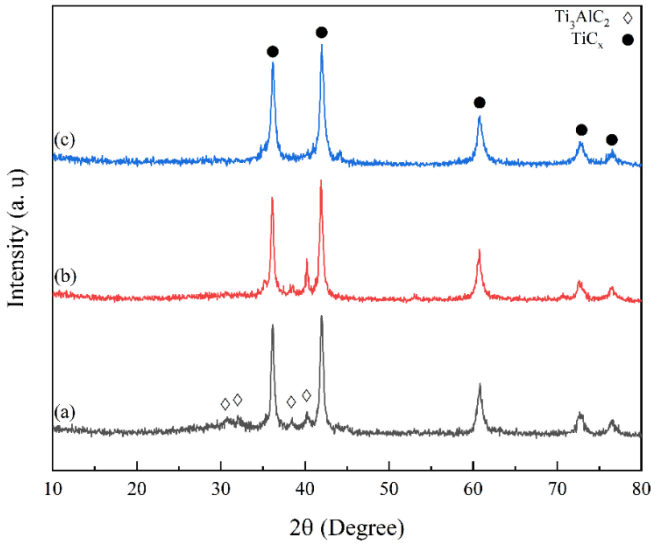

Figure 7. The XRD patterns of 2TiC-Al-Ti-xSi powder mixture after 25 h of milling: a) x=0.1, b) x=0.2 and c) x=0.3.

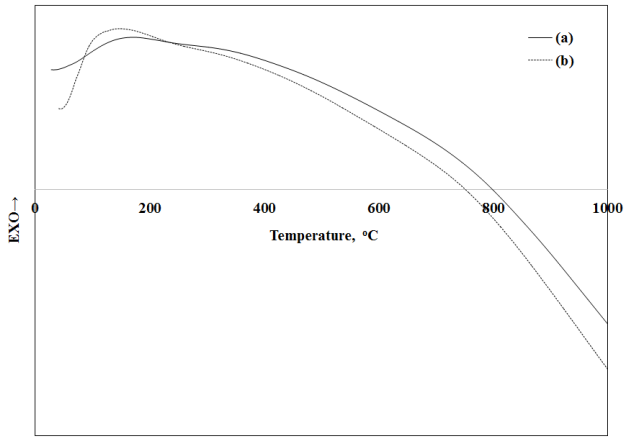

Figure 8. The DSC heating traces of a) 2TiC-Al-Ti-0.1Sn and b) 2TiC-Al-Ti-0.1Si powder mixtures after 25 h of milling.

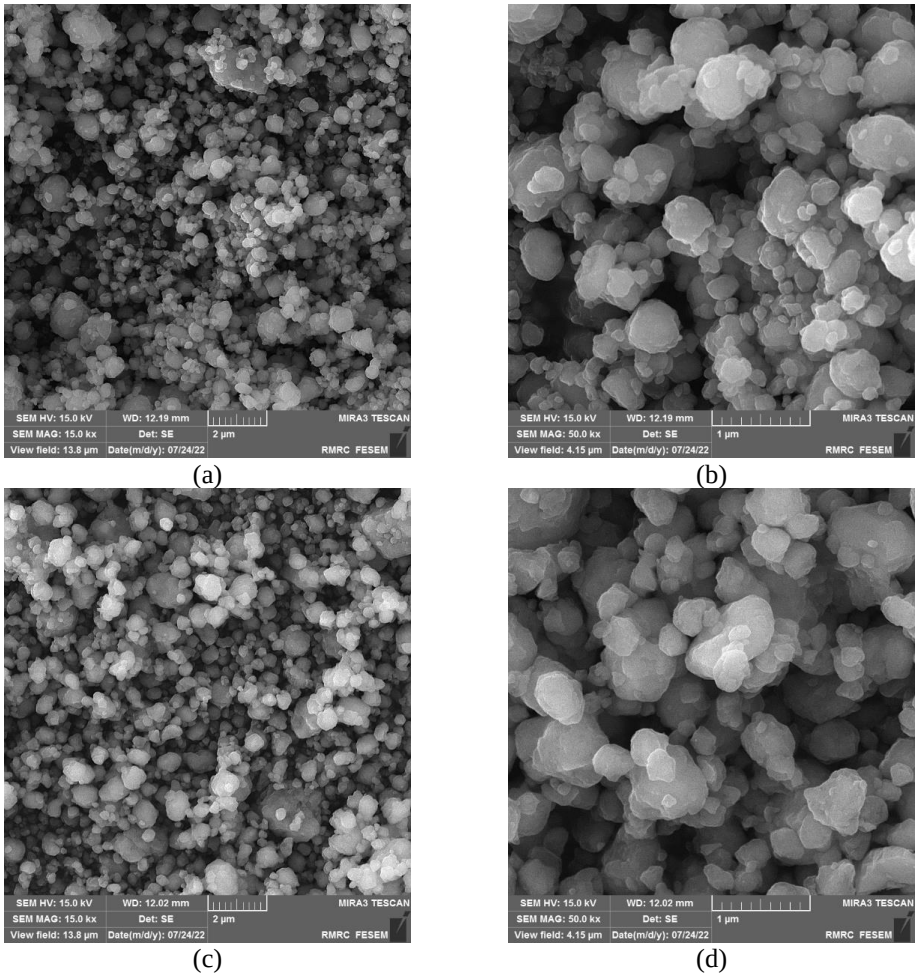

Figure 9. The SEM micrographs of a & b) 2TiC-Al-Ti-0.1Sn and c & d) 2TiC-Al-Ti-0.1Si powder mixtures after 25 h of milling.

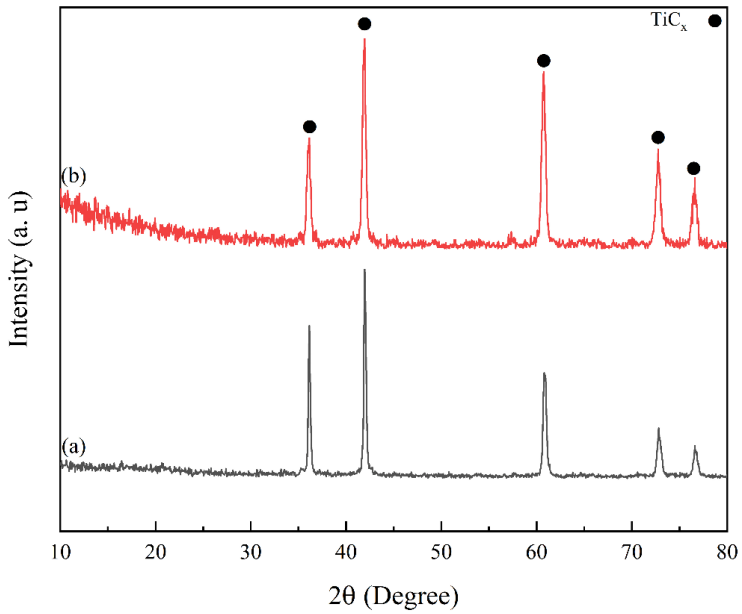

Figure 10. The XRD patterns of milled a) 2TiC-Al-Ti-0.1Sn and b) 2TiC-Al-Ti-0.1Si powder mixtures after heat treated at 1400 ºC for 1 h.

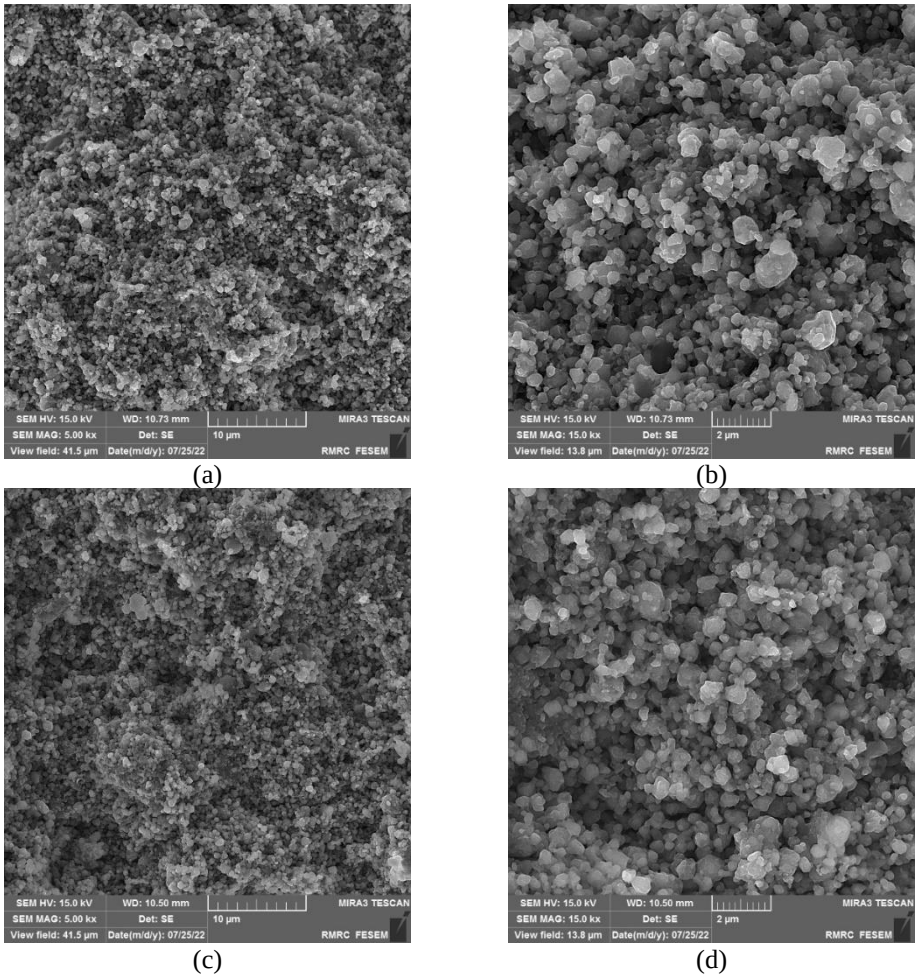

Figure 11. The SEM micrographs of milled a & b) 2TiC-Al-Ti-0.1Sn and c & d) 2TiC-Al-Ti-0.1Si powder mixtures after annealing at 1400 ºC for 1 h.

4. CONCLUSION

This research focused on the structural and phase transformations in the 2TiC-Al-Ti system during the milling and annealing processes, as well as the effect of Sn and Si additions on the formation and stability of the Ti_3AlC_2 phase. The investigation revealed the following key findings:

- It was not possible to create a single-phase Ti_3AlC_2 structure through the milling process in the 2TiC-Al-Ti system. The structure obtained during milling was a combination of TiC_x and Ti_3AlC_2 phases.
- The Ti_3AlC_2 phase formed during milling in the 2TiC-Al-Ti system was unstable and transformed into a single-phase TiCx solid solution as milling continued.
- The TiC/Ti_3AlC_2 composite structure in the 2TiC-Al-Ti system transformed into TiC/Al_3Ti, and eventually into TiC_x, during annealing up to 1400 °C. Ultimately, the stable phase in the TiC-Al-Ti system was the single-phase TiC_x solid solution.
- The addition of Sn and Si had a negative effect on the formation and stability of the Ti_3AlC_2 compound.

ACKNOWLEDGEMENTS

The authors would like to acknowledge Malek-Ashtar University of Technology for supporting this research.

REFERENCES

1. Averichev, O., Prokopets, A., Stolin, P., (2019) "*Structure formation in Ti/Ti-Al-C layered ceramic materials obtained by the method of unconfined SHS compaction*", Refractories and Industrial Ceramics, 60, 219-222. https://doi.org/10.1007/s11148-019-00339-5
2. Bandyopadhyay, D., Sharma, R., Chakraborti, N., (2000) "*The Ti-Al-C system",* Journal of Phase Equilibria, 21, 195-198. https://www.researchgate.net/profile/Debashis-Bandyopadhyay/publication/238894797_The_Ti_Al_C_system_titanium_-_aluminum_-_carbon/links/560d7dea08ae2aa0be4a3b7c/The-Ti-Al-C-system-titanium-aluminum-carbon.pdf
3. Barsoum, M.W., "*MAX phases: properties of machinable ternary carbides and nitrides*", John Wiley & Sons, 2013. https://www.wiley.com/en-us/MAX+Phases%3A+Properties+of+Machinable+Ternary+Carbides+and+Nitrides-p-9783527654604

4. Baviera, P., Harel, S., Garem, H., Grosbras, M., (2001) "*Elaboration and structure of nanostructured TiC, a XRD and HRTEM study*", Scripta Materialia, 44, 2721-2727. https://doi.org/10.1016/S1359-6462(01)00963-0
5. Cai, L., Huang, Z., Hu, W., Lei, C., Wo, S., Li, X., Zhai, H., Zhou, Y., (2018) "*Fabrication and microstructure of a new ternary solid solution of $Ti_3Al_{0.8}Si_{0.2}Sn_{0.2}C_2$ with high solid solution strengthening effect*", Ceramics International, 44, 9593-9600. https://doi.org/10.1016/j.ceramint.2018.02.183
6. Cai, L., Huang, Z., Hu, W., Chen, Y., Tan, Z., Radovic, M., (2021) "*Effects of Al substitution with Si and Sn on tribological performance of Ti_3AlC_2*", Ceramics International, 47, 6352-6361. https://doi.org/10.1016/j.ceramint.2020.10.214
7. El-Eskandarany, M. Sherif., (2015) "*Mechanical alloying: nanotechnology, materials science and powder metallurgy*", Elsevier,. https://www.google.com/books/edition/Mechanical_Alloying/kwjGAgAAQBAJ?hl=en&gbpv=0
8. Eryomina, M., Lomayeva, S., Demakov, S., (2021) "*Synthesis of composite based on Ti_2AlC with added nanographite via wet ball milling followed by spark plasma sintering*", Materials Chemistry and Physics, 273, , 125114-125122. https://doi.org/10.1016/j.matchemphys.2021.125114
9. Gao, L., Han, T., Guo, Z., Zhang, X., Pan, D., Zhou, S., Chen, W., Li, S., (2020) "*Preparation and performance of MAX phase Ti_3AlC_2 by in-situ reaction of Ti-Al-C system*", Advanced Powder Technology, 31, 3533-3539. https://doi.org/10.1016/j.apt.2020.06.042
10. Ge, Z., Chen, K., Guo, J., Zhou, H., Ferreira, J.M., (2003) "*Combustion synthesis of ternary carbide Ti_3AlC_2 in Ti-Al-C system*", Journal of the European Ceramic Society, 23, 567-574. https://doi.org/10.1016/S0955-2219(02)00098-5
11. Guo, C., Wang, E., Wang, S., Hou, X., He, Z., Liang, T., Chou, K.C., (2021) "*Oxidation mechanism of MAX phases (Ti_3AlC_2 powders) with and without Sn doping*", Corrosion Science, 180, 109197-109206. https://doi.org/10.1016/j.corsci.2020.109197
12. Hongxiang, Z., Zhenying, H., Mingxing, A., Yang, Z., Zhili, Z., Shibo, L., (2005) "*Tribophysical properties of polycrystalline bulk Ti_3AlC_2*", Journal of the American Ceramic Society, 88, 3270-3274. https://doi.org/10.1111/j.1551-2916.2005.00588.x
13. Kumar, J.A., Prakash, P., Krithiga, T., Amarnath, D.J., Premkumar, J., Rajamohan, N., Vasseghian, Y., Saravanan, P., Rajasimman, M., (2022) "*Methods of synthesis, characteristics, and environmental applications of Mxene: A comprehensive review*", Chemosphere, 286, 131607-131619. https://doi.org/10.1016/j.chemosphere.2021.131607
14. Li, S., Xiang, W., Zhai, H., Zhou, Y., Li, C., Zhang, Z., (2008) "*Formation of a single-phase Ti_3AlC_2 from a mixture of Ti, Al and TiC powders with Sn as an additive*", Materials Research Bulletin, 43, 2092-2099. https://doi.org/10.1016/j.materresbull.2007.09.016
15. Li, X., Xie, X., Gonzalez-Julian, J., Malzbender, J., Yang, R., (2020) "*Mechanical and oxidation behavior of textured Ti_2AlC and Ti_3AlC_2 MAX phase materials*", Journal of the European Ceramic Society, 40, 5258-5271. https://doi.org/10.1016/j.jeurceramsoc.2020.07.043
16. Li, S.B., Zhai, H.X., Bei, G., Zhou, Y., Zhang, Z., (2006) "*Formation of Ti_3AlC_2 by mechanically induced self-propagating reaction in Ti-Al-C system at room temperature*", Materials Science and Technology, 22, 667-672. https://doi.org/10.1179/174328406X91050
17. Łopaciński, M., Puszynski, J., Lis, J., (2001) "*Synthesis of ternary titanium aluminum carbides using self-propagating high-temperature synthesis technique*", Journal of the American Ceramic Society, 84, 3051-3053. https://doi.org/10.1111/j.1151-2916.2001.tb01138.x
18. Mingxing, A., Hongxiang, Z., Yang, Z., Zhaoyun, T., Zhenying, H., Zhili, Z., Shibo, L., (2006) "*Synthesis of Ti_3AlC_2 powders using Sn as an additive*", Journal of the American Ceramic Society, 89, 1114-1117. https://doi.org/10.1111/j.1551-2916.2005.00818.x
19. Mossino, P., (2004) "*Some aspects in self-propagating high-temperature synthesis*", Ceramics International, 30, 311-332. https://doi.org/10.1016/S0272-8842(03)00119-6
20. Pang, W.K., Low, I.M., O'connor, B., Studer, A.J., Peterson, V., Sun, Z.M., Palmquist, J.P., (2010) "*Comparison of thermal stability in MAX211 and 312 phases*", Journal of Physics: Conference Series, IOP Publishing, 41, 12025-12029. https://doi.org/10.1088/1742-6596/251/1/012025
21. Pazniak, A., Bazhin, P., Shchetinin, I., Kolesnikov, E., Prokopets, A., Shplis, N., Stolin, A., Kuznetsov, D., (2019) "*Dense Ti_3AlC_2 based materials obtained by SHS-extrusion and compression methods*", Ceramics International, 45, 2020-2027. https://doi.org/10.1016/j.ceramint.2018.10.101
22. Shahin, N., Kazemi, S., Heidarpour, A., (2016) "*Mechanochemical synthesis mechanism of Ti_3AlC_2 MAX phase from elemental powders of Ti, Al and C"*, Advanced Powder Technology, 27, 1775-1780. https://doi.org/10.1016/j.apt.2016.06.008
23. Tzenov, N.V., Barsoum, M.W., (2000) "*Synthesis and characterization of Ti_3AlC_2*", Journal of the American Ceramic Society, 83, 825-832. https://doi.org/10.1111/j.1151-2916.2000.tb01281.x
24. Wang, X., Zhou, Y., (2003) "*Oxidation behavior of Ti_3AlC_2 at 1000-1400 ^oC in air*", Corrosion Science, 45, 891-907. https://doi.org/10.1016/S0010-938X(02)00177-4
25. Whang, Sung-Hyun, ed, (2011) "*Nanostructured metals and alloys: processing, microstructure, mechanical properties and applications*", Elsevier. https://www.sciencedirect.com/book/9781845696702/nanostructured-metals-and-alloys
26. Yao, L., Zhu, C.C., Jiang, J.X., Zhou, B.B., (2015) "*Mechanical properties of Ti_3AlC_2 ceramics before and after heat treatment*", Rare Metals, 41, 1-6. https://doi.org/10.1007/s12598-015-0609-z
27. Ye, L., Liu, Z., Li, S., Quan, M., Hu, Z., (1997) "*Thermochemistry of combustion reaction in Al-Ti-C system during mechanical alloying*", Journal of Materials Research, 12, 616-618. https://doi.org/10.1557/JMR.1997.0093
28. Yoshida, M., Sakurada, O., Akatsu, T., (2019) "*Indentation size effect and hardness anisotropy in Ti_3AlC_2 with tailored microstructures*", Materials Today: Proceedings, 16, 109-118. https://doi.org/10.1016/j.matpr.2019.05.307
29. Yoshida, M., (2012) "*Microstructural examination during the formation of Ti_3AlC_2 from mixtures of Ti/Al/C and Ti/Al/TiC*", Advances in Science and Technology, 1, 81-101. https://doi.org/10.1533/9780857096012.81
30. Yu, W., Vallet, M., Levraut, B., Gauthier-Brunet, V., Dubois, S., (2020) "*Oxidation mechanisms in bulk Ti_2AlC: influence of the grain size*", Journal of the European Ceramic Society, 40, 1820-1828. https://doi.org/10.1016/j.jeurceramsoc.2020.01.042
31. Zhu, J., Mei, B., Xu, X., Liu, J., (2004) "*Synthesis of single-phase polycrystalline Ti_3SiC_2 and Ti_3AlC_2 by hot pressing with the assistance of metallic Al or Si*", Materials Letters, 58, , 588-592. https://doi.org/10.1016/S0167-577X(03)00567-6

Advanced Ceramics Progress

Volume 9, Number 4, Autumn 2023

CONTENTS

Journal Home Page: www.acerp.ir